Summer 1987

Laminar Viscous Effects on Longitudinal Dispersion in Tidal Froude Models

Larry H. White
Old Dominion University

Recommended Citation
White, Larry H.. "Laminar Viscous Effects on Longitudinal Dispersion in Tidal Froude Models" (1987). Master of Science (MS), Thesis, Ocean & Earth Sciences, Old Dominion University, DOI: 10.25777/a69b-5893
https://digitalcommons.odu.edu/oeas_etds/311

LAMINAR VISCOUS EFFECTS
ON LONGITUDINAL DISPERSION IN TIDAL FROUDE MODELS

by

Larry H. White
B.S., March 1981, Humboldt State University
B.S., March 1984, Humboldt State University

A Thesis Submitted to the Faculty of
Old Dominion University in Partial Fulfillment of the
Requirements for the Degree of

MASTER OF SCIENCE

OCEANOGRAPHY

OLD DOMINION UNIVERSITY
August 1987

Approved by:

Dr. Carvel H. Blair (Director)

Dr. Chester E. Grosch

Dr. Ronald E. Johnson

ABSTRACT

LAMINAR VISCOUS EFFECTS ON LONGITUDINAL DISPERSION IN TIDAL FROUDE MODELS

Larry H. White
Old Dominion University, 1987
Director: Dr. Carvel H. Blair

A laboratory investigation was designed to test the ability of a tidal Froude model operated according to the minimum Reynolds number criterion of 1400 to simulate the longitudinal dispersion of its turbulent, laboratory prototype in the absence of depth distortion and density stratification. To examine the model's performance, comparative tracer-dye dispersion tests were conducted in the model and in the prototype to determine spatial and temporal longitudinal dye distributions. Froude similitude of cross-sectional mean tide heights and current velocities was achieved. The minimum Reynolds number criterion did not guarantee turbulent flow throughout all tidal stages, prolonged periods of laminar flow existed near times of slack current in the model. Similitude of longitudinal dispersion was not achieved, longitudinal dispersion was exaggerated in the model. The results of this investigation indicate that tidal Froude models operated according to the minimum Reynolds number criterion and validated for similitude of mean tidal motion can be expected to produce laminar viscous effects

which are not present in the prototype and to magnify longitudinal dispersion as a result of laminar viscous scale effects.

This thesis is dedicated to my Mother and Dad
Helen Hain White and Donald Ray White

ACKNOWLEDGEMENTS

This investigation was supported by grants and funds acquired by the director of my thesis committee, Dr. Carvel H. Blair: (1) Old Dominion University Research Foundation Grant No. 80-085, (2) Old Dominion University Research Foundation Grant under Sea Grant Consortium Grant No. 81-672, and (3) the author's research assistanceship funded by the Department of Oceanography, Old Dominion University. Technical assistance was provided by Robert Powell, David Timpy, and Michael Jugan during the development of the capacitance wave height measuring system. Technical assistance was provided by Thurmond Gardner and Robert Kizar during the design and construction of the tide generator. The flume was designed by Dr. Blair and constructed by Dr. George Hecker. Assistance was provided by John Keating during many phases of the project. Portions of the water sampling system were donated by the U.S. Army Corps of Engineers. Various materials and equipment were supplied by the Department of Oceanography, Old Dominion University and the Old Dominion University Science Shop. Numerical calculations and word processing were performed on the Old Dominion University DEC-system 10 and Vector System 2600 computing facilities. The author gratefully acknowledges this support and assistance.

I wish to thank all members of my advisory committee, Dr. Blair, Dr. Chester E. Grosch, and Dr. Ronald E. Johnson, for their assistance in the completion of this project.

Above all, I am grateful to my wife, Ellen and my son, Grant. Ellen's love, patience, understanding, and encouragement made the completion of this project possible.

TABLE OF CONTENTS

Page

Chapter

LIST OF TABLES

LIST OF FIGURES

Figure Page

Figure Page

Chapter 1

INTRODUCTION

Purpose

Previously, several physical hydraulic model investigations were undertaken in the upper reaches of estuary models to predict the spread of pollutants. Frequently the flow in the upper reaches was characterized by low Reynolds numbers due to shallow model depths and low advective velocities, in contrast to the turbulent flow regime of the prototype. Lack of similitude of longitudinal dispersion in these investigations stimulated an inquiry into a model's ability to simulate longitudinal dispersion under these conditions. It was hypothesized that the minimum Reynolds number criterion for tidal models is not adequate to produce turbulent flow throughout all tidal stages in the upper reaches and that the resulting, laminar viscous scale effects cause distortion of longitudinal dispersion. The primary objective of this study was to test the ability of a tidal Froude model operated according to the minimum Reynolds number criterion to simulate the longitudinal dispersion of its laboratory prototype. Preliminary objectives required that an existing laboratory flume, designed especially for this investigation be equipped with a tide generating mechanism and wave height measuring system.

Background

The capacity of estuaries to assimilate pollutants is a matter of increasing interest among oceanographers and others concerned with environmental water quality. Among the several methods of studying mass transfer of pollutants in estuaries has been the use of physical hydraulic models. A specific objective of using physical models has been to empirically determine the longitudinal dispersion coefficient for a given reach of an estuary. The longitudinal dispersion coefficient is a measure of the rate of spreading of a distribution of marked fluid particles in the streamwise direction. The coefficient is determined by comparing solutions of the mass transfer equation with measured model concentration distributions of a tracer dye. The same dispersion coefficient is then used to predict the concentration distribution of a pollutant in the prototype estuary (Harleman 1971).

Conventionally these models are distorted Froude models constructed with an exaggerated depth scale and operated according to Froude-law scaling relationships. The Froude model law of similarity establishes that the ratio of inertial forces F_i to gravitational forces F_g in the model should equal the corresponding ratio in the prototype. In estuarine tidal flows, gravitational forces are the dominant forces contributing to fluid motion. Since inertial reaction is always present in flow phenomenon, it follows that inertial forces must be considered in any particular flow situation. The inertial force characterizes the natural resistance of a fluid to any change in its state of motion and is equal to the sum of all external forces applied to that fluid. To express these forces in usable terms their physical equivalents in terms of density ρ, gravitational acceleration g, characteristic length L, and characteristic velocity V may be used. Thus,

$$F_i = \text{mass x acceleration} = (\rho L^3)(V^2/L) = \rho L^2 V^2$$

$$F_g = \text{mass x gravitational acceleration} = \rho L^3 g$$

and, with subscripts m and p indicating model and prototype quantities, respectively

$$\frac{(F_i)_m}{(F_g)_m} = \frac{(F_i)_p}{(F_g)_p}, \qquad \text{or} \qquad \frac{(\rho L^2 V^2)_m}{(\rho L^3 g)_m} = \frac{(\rho L^2 V^2)_p}{(\rho L^3 g)_p}$$

Taking $\rho_m = \rho_p$ and $g_m = g_p$, the ratios reduce to

$$\frac{V_m}{(g_m L_m)^{1/2}} = \frac{V_p}{(g_p L_p)^{1/2}}$$

and, with subscript r indicating the model-to-prototype ratios, the Froude model law is

$$\frac{V_r}{(g_r L_r)^{1/2}} = 1 \quad , \qquad \text{or} \quad \frac{(F_n)_m}{(F_n)_p} = (F_n)_r = 1$$

where, taking L as a characteristic depth, $(gL)^{1/2}$ is the celerity of a frictionless, small amplitude, shallow water wave. The dimensionless ratio $V/(gL)^{1/2}$ is called the Froude number F_n. Froude's law supposes that gravity is the dominant force contributing to the motion in both the model and the prototype, and that all forces other than gravity forces have no appreciable influence on the phenomena under investigation. To satisfy the Froude law, the effects of the non-dominant forces, i.e. viscous and capillary forces, which are negligible in the prototype, must be kept negligible in the model. Distortions in model flow patterns, a result of scale reduction, are caused by the presence of laminar flow associated with viscous forces and surface tension caused by capillary forces, and are termed scale effects.

Surface tension manifests itself at a boundary surface by the formation of a kind of membrane due to attractive forces between liquid molecules. At some point in a liquid medium, at an appreciable distance from a boundary, such molecular forces are necessarily in equilibrium. But at a boundary surface the forces are no longer the same on every side, so that a resultant force acts upon all surface molecules in a direction normal to the surface. Since the magnitude of this force is proportional to the surface area, the liquid surface therefore tends to contract until it has the minimum area possible (Rouse 1961). Therefore, surface tension becomes appreciable in physical models when the radius of curvature of the liquid surface and the distance between solid boundaries become small (Henderson 1966). Various authorities (Novak 1981, Fischer et al. 1979, LeMehaute 1976, Maxwell and Weggel 1969, Von Arx 1967, and Henderson 1966) suggest various minimum depths at which surface tension is negligible in physical models, ranging from one to three centimeters. However, the widely accepted rule-of-thumb is that model depths and channel widths should be no less than 3 cm (Webel and Schatzmann 1984).

Viscosity is a fluid property and is defined as the degree to which a fluid resists flow under an applied force, i.e. when an ordinary fluid is being distorted, a stress field is produced in it that resists the distortion (Plapp 1968). The use of the term viscosity in this study will refer to the kinematic viscosity ν, the ratio of absolute viscosity μ to the mass density.

Frictional effects in laminar flow arise because of fluid viscosity and are greatly enhanced in turbulent flow. In general, a flow's being laminar or turbulent can be viewed as resulting from viscous damping of any disturbance fluctuations that occur within it. The basic property of steady laminar flow is that at each point in space the velocity shows absolutely no variation with time other than that due to the random motion of molecules of which the fluid is composed. In nonsteady laminar flow, time variations of the velocity can be directly related to variations in the boundary conditions. In contrast, steady and nonsteady turbulent flows are characterized by random fluctuations in the velocity (roughly analogous to molecular motion but much greater) in all directions superposed on a temporal mean velocity in the downstream direction. As the fluctuations in instantaneous velocity at adjacent positions are on the average not perfectly correlated, elemental volumes of fluid that were previously close together become statistically farther apart as the population of fluid particles is advected downstream. Advection refers to the transport by an imposed current system. In nonsteady turbulent flow, the characteristic small velocity fluctuations are not directly correlated with changes in boundary conditions. The random scattering of particles due to molecular motion and turbulent motion, as described above, may be referred to as molecular diffusion and turbulent diffusion, respectively. Random scattering of particles due to molecular diffusion in laminar flow or due predominantly to turbulent diffusion in turbulent flow will be much faster in turbulent flow (Plapp 1968).

In bounded laminar or turbulent flow a velocity gradient or shear will exist due to friction at the boundary surface. This shear effect is defined as the advection of fluid at different velocities at different positions in the flow; this may be the normal velocity profile for a laminar or turbulent flow where the fluid flows faster with increasing elevation from the bed; or the shear effect may be the changes in both magnitude and direction of the velocity with depth in complex flows such as in estuaries. In turbulent shear flows the inertial forces give rise to forces called Reynolds stresses (turbulent shear stresses) which have the physical character of friction, but which are much greater than viscous friction (Pond 1978). In laminar flow, only viscous shear stresses are present. In fully turbulent flow, characteristic of estuaries, both viscous and Reynolds stresses are present, however Reynolds stresses are the dominant forces opposing the motion, compared to viscous shear stresses which are considered to be negligible (Dyer 1977). The only practical way of eliminating the effects of fluid viscosity in physical models is to satisfy another condition for Froude similitude, that of equal flow regime on the model as in the prototype (Novak 1981). It is known from hydraulics that head loss due to friction in laminar and turbulent flow differs. In laminar flow the head loss is proportional to the first power of the velocity, but in fully turbulent flow to the square of the velocity. Therefore, because the flow in the prototype estuary is considered to be turbulent, the model must not be so small that the flow regime changes to laminar flow (Novak 1981, Dyer 1977, and Pritchard 1965). This is a necessary though not sufficient requirement for the attainment of exact Froude similitude.

Where the problem to be solved is extended to that of water quality and the modeling of longitudinal dispersion, the dispersive effects are a function of the flow regime, being primarily related to the details of the velocity distribution in the channel cross section. Longitudinal dispersion is defined by Fischer (1973) as the spreading of marked fluid particles in the streamwise direction by the combined action of a velocity distribution and cross-sectional mixing. In laminar flow, cross-sectional mixing is due to molecular diffusion. In turbulent flow, molecular diffusion is neglected and cross-sectional mixing is due to turbulent diffusion. The dominant cause of longitudinal dispersion is the shearing effect of the cross-sectional velocity distribution. The shear effect refers to the dispersive action of the velocity profile; a tracer mixed throughout the cross section by molecular or turbulent diffusion will be dispersed longitudinally as it is advected downstream at the mean velocity because it is carried faster by currents at the surface and in the center of the channel than at the bottom and near the sides (Fischer 1976). It follows, that in fully turbulent flow the velocity profile will be somewhat different than in a laminar flow in the same channel and the cross-sectional turbulent mixing (diffusion) coefficient will play the role of molecular diffusion in laminar flow (Fischer et al. 1979). This is why, when attempting to replicate the process of longitudinal dispersion in physical models, the same flow regime must be preserved on the model as in the prototype, i.e. turbulent and not laminar. Because of practical considerations of scale this exact requirement is not generally met, and it is customary to operate estuary models in the smooth turbulent or transitional regions with periods of laminar flow near times of slack current (Crickmore 1972 and Harleman 1971).

The criterion for turbulent or laminar flow in open channels is the Reynolds number $R_n = uh/v$, where u and h are average hydraulic parameters of velocity and depth, respectively. Various authorities (Webel and Schatzmann 1984 Herrmann 1979, Sager and Hales 1979, Henderson 1966, Hickox 1952, Allen 1947, Stevens et al. 1942, and Allen 1934) suggest various minimum Reynolds numbers for fully turbulent flow in open channels, ranging from 750 to 4,000. For tidal flows in physical models, Allen (1947) states that for similarity of the law of fluid resistance and to minimize scale effects due to viscosity in tidal models, it may be taken as a safe rule that the Reynolds number in the model, based on the maximum current velocity at the mouth and the mean depth of the approach channels, must not be less than 1400. This critical Reynolds number was experimentally determined by Allen (1934) in a straight open channel, independent of the roughness of the rigid channel boundaries. However, this criterion does not indicate fully turbulent flow but only the transition from approximate laminar flow to turbulence.

Even so, various modeling authorities (Herrmann 1979, Sager and Hales 1979, and Henderson 1966) recommend Allen's minimum Reynolds number of 1400 as the critical Reynolds number above which tidal flow in physical models will be fully turbulent and thus sufficient for the achievement of Froude similitude. In this instance, one might expect that estuary models would not be capable of correctly modeling longitudinal dispersion.

Physical models of many of our major estuaries are already in existence, as motivation for these models has usually been problems associated with navigation improvements. These models were built primarily to study bulk tidal motion, i.e. tide heights, current velocities, and salinity intrusion. In some cases, models were verified by only comparing model and prototype mean tide heights and current velocities of the various cross sections, measured along channel centerlines. More detailed data in the cross section is usually difficult to obtain in the prototype. Generally, reproduction of prototype tide heights, current velocities and salinity is imperfect, with varying degrees of similarity. However, these verifications are typically deemed adequate for solving the navigation problems of interest. The success of these models in providing solutions to navigation problems in complex estuaries has generated a high but possibly unjustified degree of confidence in these models for use in studying water quality problems. In recent years it has been convenient to use these models to simulate the longitudinal dispersion of pollutants by studying the motion of traceable dye, however, there is no total agreement on how well these models reproduce the dispersion phenomena of the prototype (Fischer 1976).

A review of the literature dealing with the application of physical models to dispersion processes indicates that the ability of distorted models to simulate dispersion in tidal flows is unclear. Blair and Kuo (1979) reviewed published research concerning the mass transfer verifications of tidal Froude models in regions of substantially constant density and in regions of longitudinal salinity gradients. Their report indicated that in the majority of model verifications summarized, various degrees of similarity of dispersion were achieved.

However, the limitations of distorted physical models for determining longitudinal dispersion in tidal flows are well known. Fischer and Holley (1971) showed that the vertical and transverse velocity distribution and the rate of turbulent cross-sectional mixing in a distorted model are altered from that of the prototype as a result of vertical exaggeration and exaggerated types of roughness.

Several investigators give reasons why unstratified estuary models may distort dispersion phenomena. In this case longitudinal dispersion is caused by the velocity gradient, and the longitudinal dispersion coefficient does not follow Froude-law scaling. Holley et al. (1970) have shown that for velocity gradient-induced dispersion in estuaries, dispersion can be caused by velocity gradients in both the vertical and transverse directions, and that either direction may dominate. Harleman (1966) has shown that if only vertical velocity gradients are important, distorted models will greatly over emphasize longitudinal dispersion. Fischer and Holley (1971) concluded that the dispersive effects of transverse gradients may be magnified in the model, diminished, or correctly modeled, depending on the value of the prototype (dispersion) dimensionless time scale. In wide estuaries the dispersive effects of both transverse and vertical gradients are magnified in the model, and in narrow estuaries dispersion due to transverse gradients may be properly modeled, but dispersion in the model is usually caused by vertical gradients which are magnified in the model, and thus, the overall result is magnification of longitudinal dispersion. Fischer and Hanamura (1975) studied transverse mixing in a rectangular flume with vertical strip roughness and found that it may be possible to choose the width of the strips to obtain Froude scaling of longitudinal dispersion due to transverse velocity gradients but not of longitudinal dispersion due to vertical velocity gradients.

In a stratified model, Fischer et al. (1979) states that model verification of the local salinity gradient implies verification of the rate of vertical mixing. However, it implies nothing about transverse mixing. Fischer et al. (1979) reports that it is thus generally assumed that since similitude of salinity distribution exists that the model will also correctly simulate flushing of any dissolved tracer. This reasoning is only exactly correct if the pollutant to be flushed is introduced into the estuary in exactly the same way as the fresh water, otherwise initial dispersion from a local source may not be modeled correctly because of incorrect modeling of local turbulent mixing or near-source advection. Far from the source, however, it is reasonable to expect that pollutant dispersion will be modeled to the same degree of accuracy as salinity intrusion. Harleman (1971) reports that similitude of the salinity intrusion regions, a mass transfer-related-process, has been replicated fairly well in distorted models; but that this process is strongly dependent on density effects, and therefore the ability to duplicate salinity intrusion is undoubtedly related to the fact that similitude with respect to the gravitational effects is being achieved, basically in tidal motion. Since salinity intrusion is also a gravitational-type circulation process, it is possible to duplicate this.

The number of studies in the literature pertaining to the effects of flow regime on longitudinal dispersion in physical models is small. Ward (1972) conducted dispersion experiments in a laboratory tidal flume of constant-density flow, operated with a Reynolds number criterion of 1000 at the channel entrance, and found that laminar flow existed during portions of the tidal cycle; longitudinal dispersion was magnified when compared to what would be expected from calculations in fully turbulent flow. Crickmore (1972), studied dispersion in a coastal flow near Heysham, England, in a constant-density model (horizontal scale 1:250, vertical scale 1:60), and reported that turbulent flow was not fully developed at all tidal stages in the model, and that the marker plume was highly irregular until Reynolds numbers reached 7000 during the tidal cycle, at which time the plume became similar to that of the prototype. Nece et al. (1979) conducted dispersion experiments in the field and in an idealized (planform geometry) marina basin model of constant density (horizontal scale 1:500, vertical scale 1:50). He reports that Reynolds numbers in the model were low, with a peak of about 3000 at the basin entrance, and observed differences between model and prototype flow patterns.

Blair (1981, 1980, 1979) set out to determine a scientific basis for establishing shellfish buffer zones in the vicinity of marinas and small boat harbors, typically located in the upper reaches of tidal rivers entering the Chesapeake Bay, by investigating the feasibility of using the model to study longitudinal dispersion of a conservative tracer-dye from tidal marina locations. The bulk of his experimental work was conducted in the Lafayette River portion of the U.S. Army Engineer Waterways Experiment Station's (WES) Chesapeake Bay Hydraulic Model, Matapeake, Maryland (horizontal scale 1:1000, vertical scale 1:100). The Lafayette River, located in Norfolk, Virginia, is situated in the lower Chesapeake Bay and characterized by Blair (1976) through prototype studies, as a well-mixed estuary (longitudinal density gradient). Comparisons of model and prototype spatial and temporal dye distributions indicated that similitude of longitudinal dispersion was not achieved for the Lafayette River portion of the model or for any of the other tidal rivers investigated in the model (Daily Press 1983, Coates 1982, and Cook 1982). Jugan (1982) conducted similar dispersion experiments in the Lafayette River portion of the WES model related to the effects of varying river discharge on longitudinal dispersion, dispersion similitude was also not achieved. Both investigators attributed the lack of similitude in the Lafayette River portion of the model to the effects of surface tension in the two upper branches of the Lafayette River model. The mean depth in the Lafayette River portion of the model was 3.1 cm in the main channel and 1.1 cm in the two upper branches. However, the calculated model Reynolds number at the mouth of the Lafayette River was about 850. Blair (1976) also conducted dispersion studies in a highly distorted model of the Lafayette River (horizontal scale 1:540, vertical scale 1:12), Old Dominion University (ODU), Norfolk, Virginia, and reported that dye concentration profiles showed good agreement in the main channel, but that dye concentrations in the two upper branches of the model were consistently higher than those of the prototype. The lack of similitude was attributed to scale effects in tide heights and current velocities resulting from high geometric distortion. The mean depth in the two upper branches of the model was 9.2 cm. The calculated model Reynolds number at the mouths of the two upper branches was about 3,000. Kuo et al. (1978) conducted similar dispersion experiments in the ODU Lafayette River model and reported similar results. As the experiments progressed with increasing numbers of tidal cycles, model dye concentrations became progressively higher than those of the prototype. The distortion of longitudinal dispersion was attributed to (1) difficulty of reproducing accurate salinity gradients and velocity fields in the model, (2) low advective velocities, (3) low freshwater discharge, and (4) dye "trapping" not observed in the prototype.

In the present study, a plunger-type tide generator was constructed for use in a laboratory flume which produced a repeatable, sinusoidal, oscillating wave of adjustable height and period. A wave height measuring system was developed which used variable-capacitance, wave height measuring probes, capable of measuring wave heights in the tidal flume to within 1 mm. A constant-density, undistorted, tidal Froude model (horizontal and vertical scales 1:1.45) operated according to the minimum Reynolds number criterion of 1400 and a laboratory prototype operated in the predominantly turbulent regime were set up in the tidal flume of rectangular cross section. The influence of density stratification on longitudinal dispersion and any limitations to the achievement of similitude of longitudinal dispersion due to vertical exaggeration in the model were eliminated. Model and prototype tide heights and current velocities, measured along the channel centerlines, were validated for Froude similitude. If it were feasible to use physical models for dispersion studies, which are operated according to the minimum Reynolds number criterion of 1400 and validated for Froude similitude of cross-sectional mean tide heights and current velocities, then the laboratory model should simulate the longitudinal dispersion of the laboratory prototype. To examine the model's performance, comparative tracer-dye tests were conducted to determine in the model and in the prototype the spatial and temporal longitudinal dye distributions experienced by the intrusion of marked water from the headbay of the tidal flume. The match between model and prototype of the longitudinal extent over time of the resulting plumes was taken as a measure of the model's ability to reproduce the dispersive mechanisms existing in the prototype.

Generally, results obtained from the present investigation indicated that tidal Froude models operated according to the minimum Reynolds number criterion of 1400 and validated for similitude of mean tidal motion can be expected to produce laminar viscous effects which are not present in the prototype and to magnify longitudinal dispersion as a result of laminar viscous scale effects. These results provide further confirmation that physical models, such as those used by government, academia, and industry to study the longitudinal dispersion of pollutants in estuaries, may give misleading results.

Chapter 2

PROTOTYPE AND MODEL TIDAL FLUME EXPERIMENTS

Design of Prototype and Model

The criteria for setting up an undistorted, constant-density, tidal Froude model (small scale) and its laboratory prototype (large scale) in a rectangular flume to investigate longitudinal dispersion were:

1) The channels should be much wider than they are deep.
2) The generated oscillatory waves should be small amplitude shallow water waves (or long waves).
3) The times required for vertical mixing should be about equal to the tidal periods.
4) The Reynolds number at the mouth of the model channel should be greater than 1400.
5) Water depths should be no less than 3 cm.

Criterion 1 must be satisfied to prevent the sidewalls of the flume from significantly influencing the transverse velocity profiles, so that the only significant velocity variations are with depth. As a result, the effect of the sidewalls on turbulent flow in a wide rectangular channel will be confined to layers of thickness on the order of the depth (Chatwin and Sullivan 1982, Novak 1981, and Knight and Macdonald 1979). A wide channel is particularly necessary since the width of the flume b will be the same for both the model and prototype, thus the width of the model will be distorted.

If criterion 2 is satisfied, the tidal range H will be small and the tidal period T will be so long that the frictionless wavelength L_0 will be much greater than the length of the channel L considered. Associated with a long wave will be small water surface slopes and small vertical velocity components. Thus the relative change in water depth over the tidal cycle will be small and the flow will be essentially horizontal, aligned with the longitudinal axis of the channel, and uniform over depth (Henderson 1966 and Ippen 1966).

If criterion 3 is satisfied, the tidal period will be similar to the time required for vertical mixing T_z between the bed of the channel and the water surface, and shear flow dispersion will have its maximum effect (Fischer 1976). In constant-density, oscillatory shear flows in wide rectangular channels, dispersion is associated primarily with the vertical velocity distribution. Vertical mixing is caused predominantly by turbulence generated by bottom shear stress, and the vertical turbulent diffusion (mixing) coefficient, averaged over the depth, is expected to be $\varepsilon_z = 0.067hu^*$, where z is the vertical cartesian coordinate in an open channel, h is the mean depth, and u^* is the depth-averaged shear velocity (Holley et al. 1970). Fischer et al. (1979) summarized a number of laboratory studies in rectangular flumes of varying channel roughness and found that $u^* \simeq 0.1u$, where u is the mean velocity in the channel cross section. Application of this equation to oscillatory flow gives $u^* \simeq 0.1u_t$, where $u_t = (2/\pi)u_{max}$ is the rms tidal velocity and u_{max} is the average of the maximum flood and ebb velocities. The time required for vertical mixing is $T_z = h^2/\varepsilon_z = (h/0.0067)u_t$. Holley et al. (1970) have found that in most estuaries $T/T_z > 1$. The maximum contribution of the shear effect in oscillatory flow is found when $T/T_z = 0.7$, resulting in a maximum dispersion coefficient (Fischer 1976).

According to various modeling authorities (Herrmann 1979, Sager and Hales 1979, Henderson 1966, and Allen 1947), criterion 4 is recommended to attain fully turbulent flow in tidal Froude models, and consequently, laminar viscous scale effects will be avoided.

Criterion 5 is the widely accepted minimum model depth required to avoid scale effects due to surface tension (Webel and Schatzmann 1984). It is believed that this rule originated as the result of an analytical examination of the limitations imposed by surface tension on the lowest scale in Froude models of regions of nearly uniform flow (Maxwell and Weggel 1969). The analysis demonstrated that the shallowest depth at which surface tension effects can be judged to have negligible influence on the Froude modeling law can be obtained from the knowledge of the accuracy of the instrumentation used in the model test and the Froude number at which the model is operated. The example given, using $F_n = 1$ and an accuracy of 1% in the measurement of model discharges, yielded a minimum depth of 2.7 cm.

The specific conditions imposed by the above criteria for oscillating flow are:

Condition No.	Condition
1)	$h/b < 0.10$
2)	$H/h < 0.10$
3)	$L/L_0 < 0.10$
4)	$T/T_z \simeq 1$
5)	$R_n > 1400$
6)	$h > 3$ cm

Both the prototype and model were to be set up in a flume channel, 24 meters long and 27.6 cm wide, designed and constructed especially for this investigation (Fig. 1).

To satisfy condition 1, the maximum mean water depth in the flume channel should be 2.76 cm. However this depth is below the limit imposed by condition 6 which is required to prevent scale effects due to surface tension. Previous experiments in laboratory flumes have used the following relaxed conditions with satisfactory result (Webel and Schatzmann 1984, Fischer et al. 1979, and Ippen 1966):

Condition No.	Relaxed Condition
1a)	$h/b < 0.20$
2a)	$H/h < 0.25$

Therefore, to satisfy condition 1a, the maximum mean water depth in the flume channel should be 5.52 cm which also satisfies condition 6.

The channel bend in the flume was another problem which warranted consideration when conducting longitudinal dispersion tests. Fischer (1969) demonstrated that channel bends increase the rate of transverse mixing due to the creation of a transverse velocity gradient, and thereby to some extent reduce longitudinal dispersion. The channel bend was avoided in the model by choosing a horizontal model length L_m of 1175 cm, i.e. the length of the model was about half the total length of the flume channel. To minimize the effect of the channel bend for the longitudinal dispersion test conducted in the prototype, it was decided that the durations of the prototype and model tests should be limited by the number of tidal cycles it took for the dye plume to reach the bend in the prototype.

The values of the hydraulic parameters for the model were established following the prescribed criteria by testing various combinations of tidal periods, tidal ranges, and mean water depths while monitoring tide heights and current velocities at the mouth of the channel. The parameters used for the model setup were those which produced a Reynolds number of about 1500 at the channel mouth; Allen (1947) defines this Reynolds number as $R_n = u_{max(flood)}h/v$. Having determined a mean water depth for the model $h_m = 3.80$ cm and choosing $h_p = 5.52$ cm for the prototype, adhering to criterion 1a, the required model-to-prototype horizontal length ratio was $L_r = 0.69$. Experimentally determined values for the model parameters and the required values for the prototype parameters, based on geometric relations and the Froude criterion of scaling for an undistorted model, along with the required scale ratios, are given in Table 1.

Table 1. Summary of prototype and model data and scale ratios.

Parameter[1]	Units	Ratio[2]	Prototype	Model
Channel Length L	cm	L_r	1705	1175
Channel width b	cm	(3)	27.6	27.6
Depth at low water h_{LW}	cm	L_r	4.88	3.37
Depth at high water h_{HW}	cm	L_r	6.10	4.21
Mean depth h	cm	L_r	5.52	3.80
Tidal range H	cm	L_r	1.22	0.84
Tidal period T	s	$(L_r)^{1/2}$	233	193
Tidal wavelength L_o	cm	L_r	17,070	11,778
$L_o = T(gh)^{1/2}$				
Maximum flood velocity $u_{max(f)}$	cm/s	$(L_r)^{1/2}$	4.80	3.98
Maximum ebb velocity $u_{max(e)}$	cm/s	$(L_r)^{1/2}$	6.70	5.56
Mean maximum velocity u_{max}	cm/s	$(L_r)^{1/2}$	5.75	4.77
$u_{max} = [u_{max(f)} + u_{max(e)}]/2$				
RMS tidal velocity u_t	cm/s	$(L_r)^{1/2}$	3.65	3.03
$u_t = (2/\pi)u_{max}$				
Reynolds number R_n	--	$(L_r)^{3/2}$	2653	1512
$R_n = u_{max(f)}h/\nu$				
Time for vertical mixing T_z	s	$(L_r)^{1/2}$	225	187
$T_z = h/(0.0067u_t)$				
<u>Parameter Ratio:</u>				
h/b	--	--	0.20	0.14
H/h	--	--	0.22	0.22
L/L_o	--	--	0.10	0.10
T/T_z	--	--	1.03	1.03

---

[1] Parameter values apply to the channel entrance ($x = 0$).

[2] $L_r = 0.69$, $(L_r)^{1/2} = 0.83$, and $(L_r)^{3/2} = 0.57$.

[3] The model is laterally (width) distorted.

Equipment

Flume

A flume was designed and constructed particularly for this study by Dr. Carvel Blair and Dr. George Hecker. The flume shown in Figure 1, is housed in the Department of Oceanography building at Old Dominion University and consists of a channel and a headbay designed to accommodate a plunger-type tide generator.

The entire channel is composed of two 12-m long channels laid parallel to each other and connected at one end by a bend. At the opposite end, one channel section is closed and the other channel section is connect to the headbay. The entire channel is 24.0 m long, 27.6 cm wide, and 30.5 cm deep. The bottom of the channel stands 75.6 cm above a concrete floor and is supported by masonry blocks, stacked two blocks high on both sides of the channel and spaced at 2.4 m intervals along the length of the channel. The headbay is 240.0 cm long, 57.2 cm wide, and 61.0 cm deep. The bottom of the headbay stands 45.1 cm above the concrete floor and is supported by masonry blocks, stacked one and a half blocks high on both sides of the headbay and spaced at 1.2 m intervals along the length of the headbay.

The bottom and sides of the headbay are each composed of a solid section of 1.9 cm thick, marine grade plywood.

Fig. 1. The 24 meter flume and headbay.

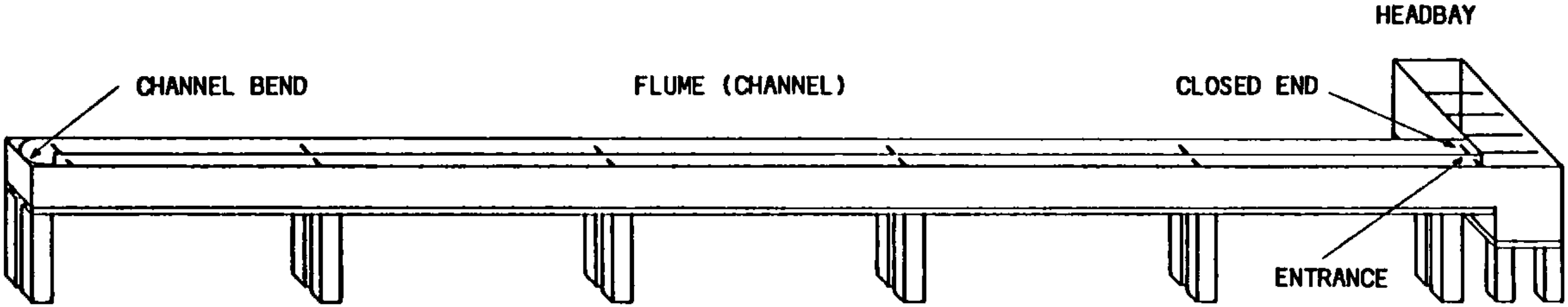
HEADBAY
CHANNEL BEND
FLUME (CHANNEL)
CLOSED END
ENTRANCE

The channel is constructed of five 2.4-m long sections to allow easy disassembly since the flume was intended to be a temporary installation. The bottom and sides of each channel section are composed of a solid piece of 1.9 cm thick, marine grade plywood. The sides of the channel and headbay are connected to plywood bottoms with wood screws. Each channel section is fitted with grooves at both ends. The channel sections are joined end-to-end in the grooves and fastened with wood screws. The headbay is also attached to the channel with wood screws. The inside corners and joints of the headbay and channel are lined with 10 cm wide strips of fiber glass cloth coated with marine fiber glass. To provide additional support to the sides of the channel, 1.3 cm diameter, threaded steel rods are fitted laterally across the channel through holes at the top of the sidewalls at each channel section joint and bolted in place. Threaded rods are also bolted to the top of the headbay and spaced 48 cm apart along its length. The parallel channels are joined at one end by a sheet metal bend, bent to a 27.6 cm radius. The metal bend is attached to the channel bottom and sidewalls with fiber glass cloth coated with marine fiber glass. The inside of the flume is coated with three coats of pigmented, aqua-blue, marine fiber glass. The outside of the flume is coated with white latex paint.

The flume rests on steel I-beams which are 2 m long by 5.1 cm wide and are bolted together end-to-end along the length of the flume and connected laterally with 1.3 cm diameter threaded rods. The bed of the channel was leveled with a carpenter's level by placing wooden shims between the I-beams and masonry block supports.

The flume is filled with tap water from a garden hose and fitted with two 7.6-cm diameter bottom drains and cover plugs located midway along the centerline of each 12 m long channel section. The headbay is also fitted at one end with a 7.6 cm diameter bottom drain and cover plug. The channel can be adjusted to a desired length by placement of a temporary, acrylic plastic barrier, sealed with "MORTITE" caulking cord, in the channel cross section.

Tide Generator

Tidal flow is produced in the flume by a plunger-type tide generator shown in Figure 2. In this method, a plunger is suspended in the headbay of the flume from a lever which is driven by a constant speed electric motor through reduction gears and a reciprocating mechanism, the function of which is to provide a sinusoidally varying water level in the flume (Allen 1947). The plunger is connected to a balancing system consisting of a cam from which is suspended a balance weight. The cam provides a variable moment arm about its axis of rotation, while the plunger exerts a variable downward force at a constant moment arm. The system thus maintains approximate equilibrium. When the plunger is set in motion, the effective (varying) downward force (weightless buoyant force) of the oscillating (up and down)

Fig. 2. Plunger-type tide generator.

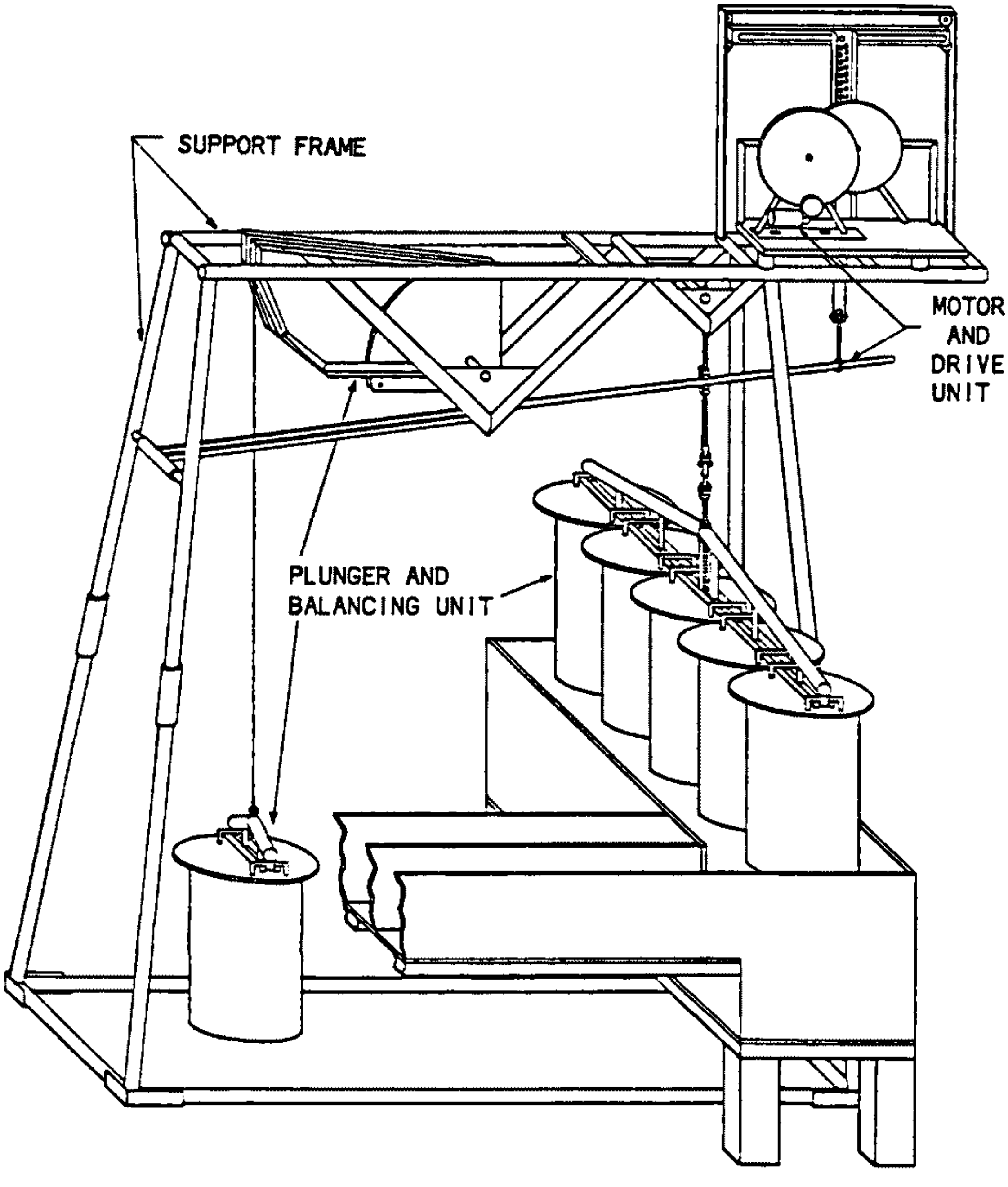
SUPPORT FRAME
MOTOR AND DRIVE UNIT
PLUNGER AND BALANCING UNIT

plunger is continuously balanced through the rocking (back and forth) motion of the cam. At low water the cam has its largest moment arm, providing the greatest balancing moment and corresponding to a minimum plunger buoyancy (Fig. 2). Conversely, at high water when plunger immersion is maximum, the cam is in a position which provides the least leverage to the balance weight and thus corresponds to a maximum plunger buoyancy shown in Figure 4. The tide generator is functional at various channel lengths, water levels, and tidal ranges. For example, when the length of the channel is set at 12 m, the maximum tidal range is about 7 cm with a low water depth of about 23 cm, and for a channel length of 24 meters, the maximum tidal range is about 5 cm with a low water depth of about 25 cm. The tide generator was designed to operate at tidal periods of 2 to 15 minutes.

The tide generator is composed of three major units: the support frame, the plunger and balancing unit, and the motor and drive unit. The support frame shown in Figure 3, provides a structure for mounting and suspending a total mass of about 635 kg (1400 lb). The tide generator straddles the headbay of the flume and stands 3.1 m high on a base that is 2.4 m long and 1.2 m wide. The upper frame is constructed of steel pipes and steel plate mounting brackets and joined by welds. The lower frame is constructed of steel pipe and angle bar and is composed of a set of legs and a base. Angle bar feet are welded to the bottom of each lower leg and bolted to angle bar cross members to form a rec-

Fig. 3. Tide generator support frame assembly.

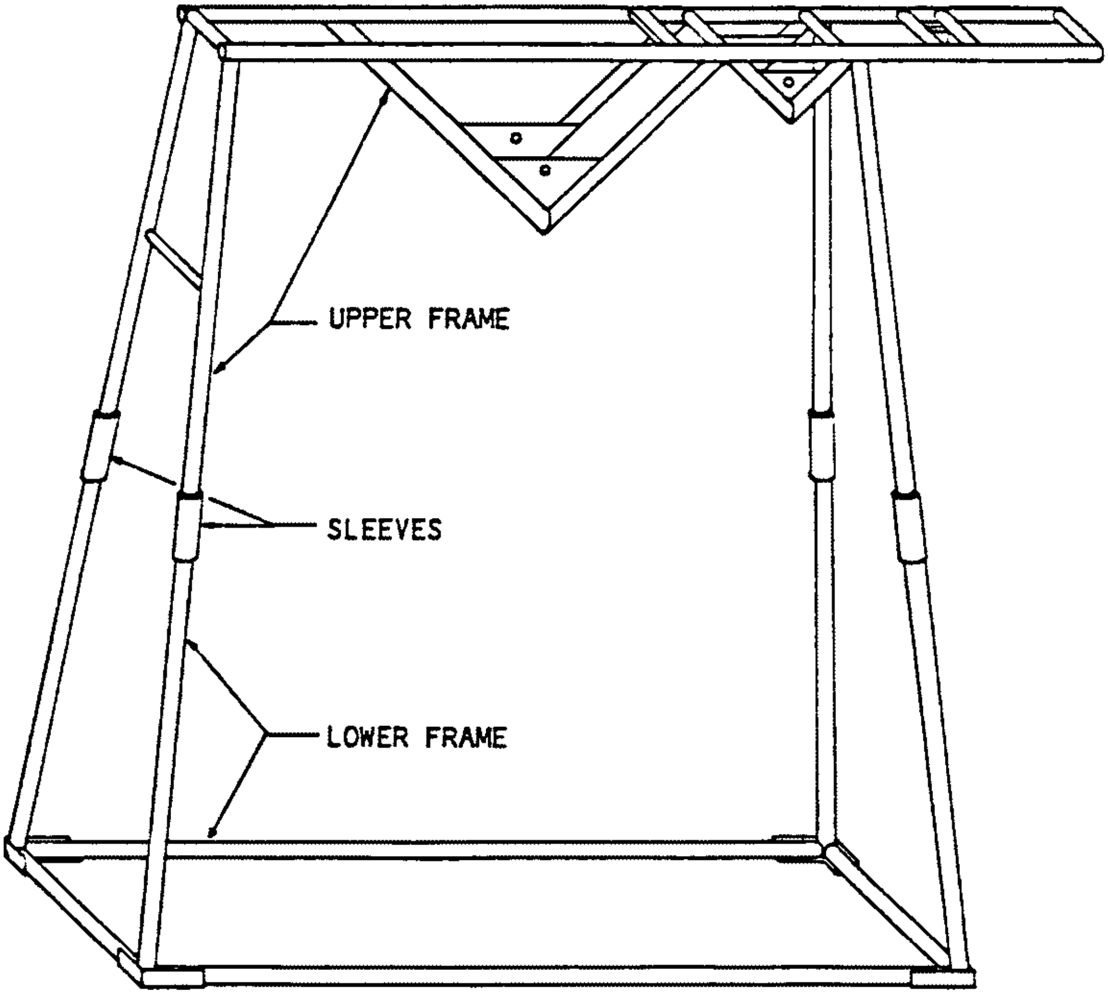
UPPER FRAME
SLEEVES
LOWER FRAME

tangular base. Pipe sleeves are welded to the top of each lower leg and allow the upper frame legs to be fitted into the lower legs and to be bolted in place. The upper frame is bolted to the lower frame to provide convenience in assembling the tide generator.

The plunger and balancing unit consist of a plunger assembly and balancing assembly shown in Figure 4. The plunger assembly consists of a plunger and the plunger coupling components. The plunger is composed of five 75-liter, sand-filled, aluminum alloy cylinders and mounted on a support bar. The support bar is constructed of steel pipe and joined by welds. The support bar passes through the handles of the cylinder covers and is fastened to the handles with U-bolts. A hole through the center of the support bar and through the cover of the center cylinder provides clearance for a 1.3 cm diameter lower threaded rod. The lower threaded rod is attached to the support bar by a nut which is welded to the top of the support bar. Vertical adjustment of the lower threaded rod allows the plunger to be positioned at any depth in the headbay. The plunger coupling assembly is attached to an eye nut which is fitted on top of the lower threaded rod. The plunger is coupled to the cam-disk of the balancing assembly by a 4.8 mm diameter, steel cable and a 1.3 cm diameter, upper threaded rod fitted with an eye nut at either end. The plunger is connected to the bottom eye nut of the upper threaded rod by a jaw-and-eye-swivel and shackle arrangement attached to the lower threaded rod. The

Fig. 4. Tide generator plunger and balancing assembly.

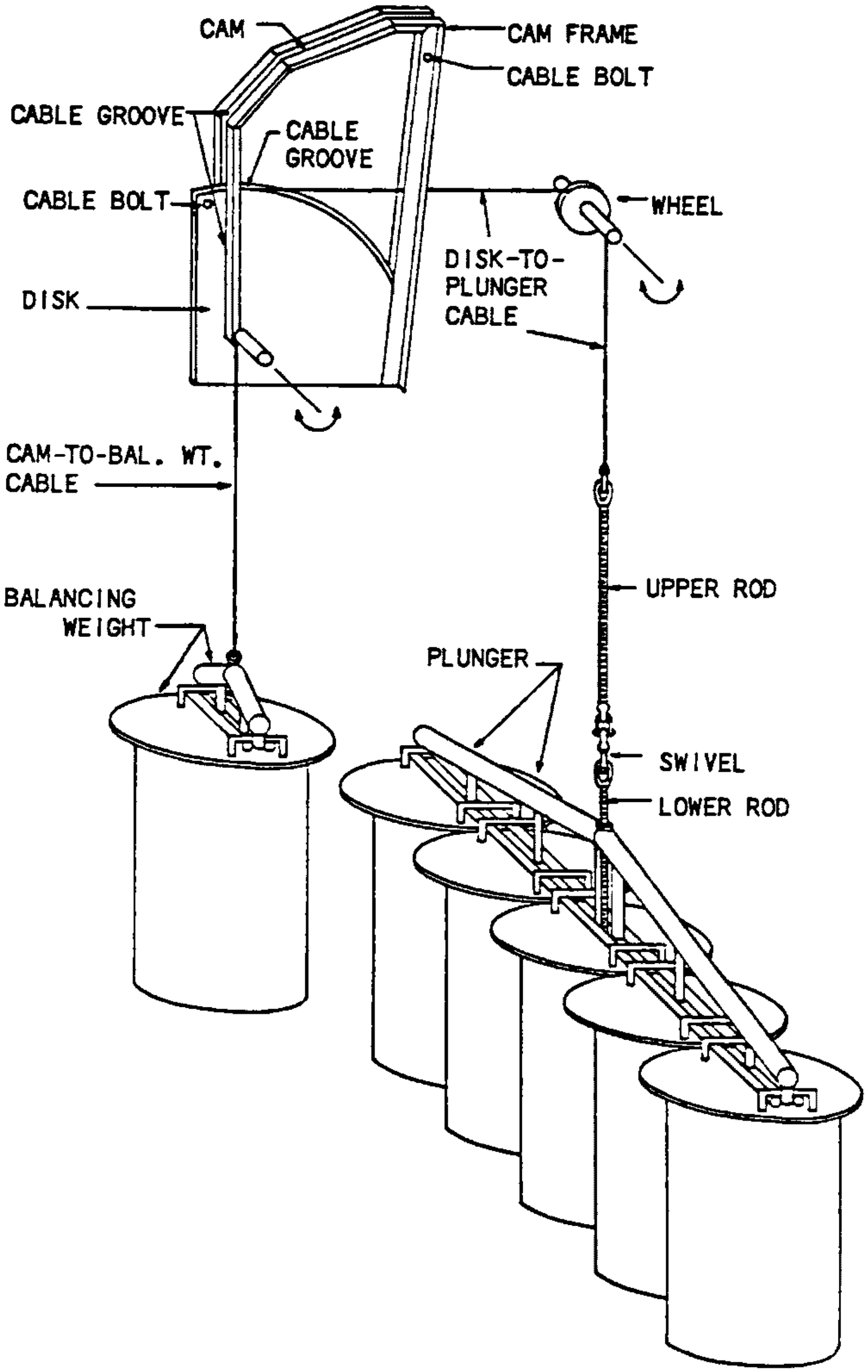
CAM
CAM FRAME
CABLE BOLT
CABLE GROOVE
CABLE GROOVE
CABLE BOLT
WHEEL
DISK-TO-PLUNGER CABLE
DISK
CAM-TO-BAL. WT. CABLE
UPPER ROD
BALANCING WEIGHT
PLUNGER
SWIVEL
LOWER ROD

swivel allows the lower threaded rod to be turned without twisting the cable when adjusting the height of the plunger. The cable running from the cam-disk is fitted with a thimble and shackled to the top eye nut of the upper threaded rod. The cable passes over a wheel which is fitted with roller bearings and mounted directly above the plunger on the support frame. The plunger assembly has a mass of 367 kg (813 lb).

The balancing assembly consists of a cam-disk and a balance weight. The cam-disk is one unit and is composed of a cam which is welded to a 35.3 cm radius, steel quarter-disk fitted with a shaft. Each end of the shaft is fitted with a ball bearing pillow block mounted on the support frame. The disk is constructed of a 6.4 mm thick, steel plate sandwiched between two 3.2-mm thick, steel plates. The center plate is inset 6.4 mm to form a groove along the radius of the disk to guide the cable attached to the plunger assembly. One end of the cable is fitted with a thimble and is bolted in the groove at one corner of the disk. The disk rotates back and forth through a maximum angle θ of 90 degrees, providing a maximum plunger stroke of 55.5 cm. The plunger stroke is equal to the entire arc length of the disk. This maximum plunger stroke was designed to be used with a channel length of 24 m. The disk serves to couple the motion and weight of the plunger to the cam and balance weight. The cam provides a maximum moment arm of 76.2 cm and a minimum moment arm of 2.5 cm and is constrained to move through a maximum angle θ of 90 degrees by stop bars welded to the support frame. The cam is constructed of a 6.4 mm thick, steel plate inset and sandwiched between two 3.2-mm thick angle bar support frames to form a groove to guide the cable from which the balance weight is suspended. One end of the cable is bolted to the end of the cam and the other end is shackled to a hoist eye on the balance weight. The balance weight is composed of a 75 liter, sand and lead-filled, aluminum alloy cylinder and mounted on a support bar. The support bar passes through the handles of the cylinder cover and is fastened to the handles with U-bolts. The balance weight has a mass of 163 kg (360 lb) and the cam-disk has a mass of 25 kg (56 lb).

The tide generator is equipped with a plunger securing hook which extends from the shaft of the wheel and attaches to the top eye nut of the upper threaded rod. This arrangement allows the plunger to hang from the support frame when not in use and allows the cam-disk to be held at its maximum low water position when adjusting the tide generator for a particular tidal range and water level.

The design of the plunger and balancing unit was simplified by imposing the following conditions:

1) Since the system would be operated at very slow speeds, the angular acceleration of the cam-disk could be considered negligible. Thus, the system could be considered to be in mechanical equilibrium at all times and in

all cam-disk positions.

2) The system would be designed to function in mechanical equilibrium for a flume length of 24 meters.

3) The effective weight of the plunger in water would be considered to be a linear function of the angular position θ of the cam-disk.

4) All motion associated with the system would be considered to be frictionless.

In practice, any deviation from these conditions which might strain the system was compensated for by the motor and drive unit and by adjustment of the actual weights of the plunger and balance weight or by adjustment of the cam angle in relation to the vertical position of the plunger.

For the system consisting of the plunger and balancing unit, the vector components of the forces contributing to the torque about the axis of rotation of the cam-disk are shown in Figure 5. For rotational equilibrium, the sum of the resultant torques τ_o about point O is zero.

$$\sum \tau_o = W_2 d_2 - W_1 d_1 - W_3 d_3 = 0 \tag{1}$$

W_1 is the actual weight of the cam-disk. W_2 is the effective weight of the plunger in water, i.e. the fixed weight of the plunger W_p multiplied by the angular position of the cam-disk $[1-(\theta/90°)]$. W_3 is the actual weight of the balance weight. The tension in the wire cable T is equal to the ef-

Fig. 5. Free-body diagrams showing all forces acting on the tide generator plunger, cam-disk, and balancing weight.

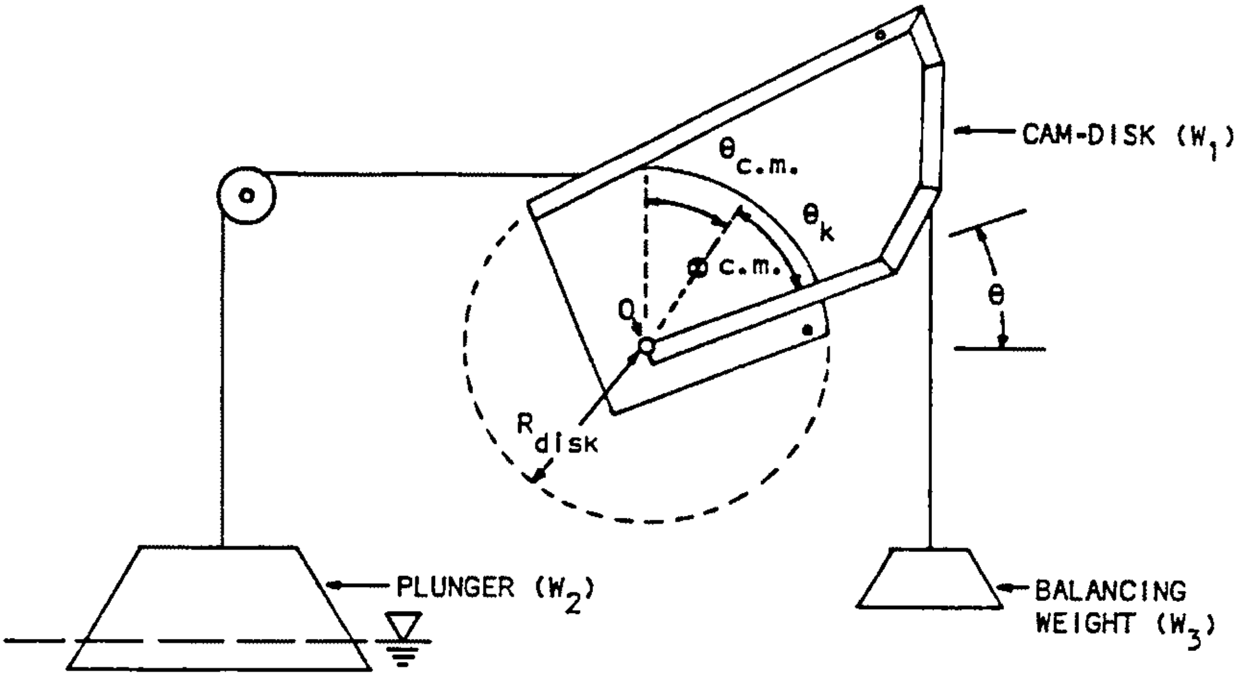
$\theta_{c.m.}$
CAM-DISK (W_1)
θ_k
c.m.
O
θ
R_{disk}
PLUNGER (W_2)
BALANCING WEIGHT (W_3)

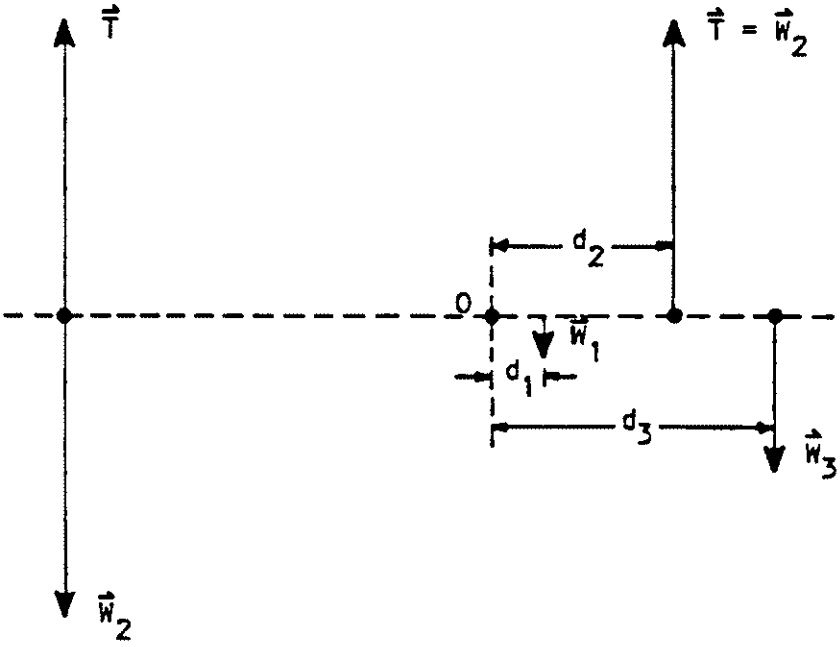
$\vec{T}$
$\vec{T} = \vec{W}_2$
d_2
O
$\vec{W}_1$
d_1
d_3
$\vec{W}_3$
$\vec{W}_2$

fective weight of the plunger in water W_2 at equilibrium. The center of mass c.m. of the cam-disk is located at a fixed angle θ_k and at a distance $d_{c.m.}$ from the axis of rotation of the cam-disk at point O. The line of action of W_1 is a distance d_1, the effective length of the moment arm associated with the center of mass of the cam-disk and is equal to a length $[(d_{c.m.})\sin(\theta_{c.m.})]$ from the axis of rotation of the cam disk at point O, where $\theta_{c.m.} = 90°-(\theta_k+\theta)$. The line of action of W_2 is the distance d_2 from point O, equal to the radius of the disk R_{disk}. The line of action of W_3 is the distance d_3, the effective length of the moment arm of the cam from point O.

Rewriting equation (1) gives

$$W_p[1-(\theta/90°)]R_{disk} - W_1 d_{c.m.}\sin[90°-(\theta_k+\theta)] - W_3 d_3 = 0 \qquad (2)$$

Solving equation (2) for the effective length of the moment arm of the cam d_3 yields the following formula for the design of the cam

$$d_3 = \frac{W_p[1-(\theta/90°)]R_{disk} - W_1 d_{c.m.}\sin[\,90°-(\theta_k+\theta)]}{W_3} \qquad (3)$$

The shape of the cam, i.e. the lengths of the moment arms associated with various angles of θ, 0 to 90 degrees, was determined by substituting the actual values used in the design of the tide generator given in Table 2 and the angles of θ from 0 to 90 degrees into equation (3).

Table 2. Summary of data for the tide generator design.

$W_1 = 2.5 \times 10^7$ dyne

$W_p = 3.6 \times 10^8$ dyne

$W_3 = 1.6 \times 10^8$ dyne

$d_{c.m.} = 28.7$ cm

$d_2 = 35.3$ cm

$\theta_k = 35.04°$

The calculated deviations from mechanical equilibrium or unbalance in the resulting system for maximum tidal ranges in flume channels of lengths 24 m and 12 m are as follows: (1) for a 24 meter flume the maximum deviation is 5 kg (11 lb) and the average deviation is 1 kg (2 lb), and (2) for a 12 meter flume the maximum deviation is 15 kg (33 lb) and the average deviation is 6 kg (13 lb).

The major components of the motor and drive unit are an electric motor, a reduction gear assembly, and a reciprocating mechanism and lever shown in Figure 6. The motor and drive unit is mounted on a steel platform, 30 cm by 66 cm. The platform is welded to the top of the tide generator support frame. The reduction gear assembly consists of four steel gears labeled in Figure 6 as gears A,B,C, and D. The gears are driven by a 12 volt dc motor. The speed of the motor is controlled by a variable dc power supply. The reduc-

Fig. 6. Tide generator motor and drive assembly.

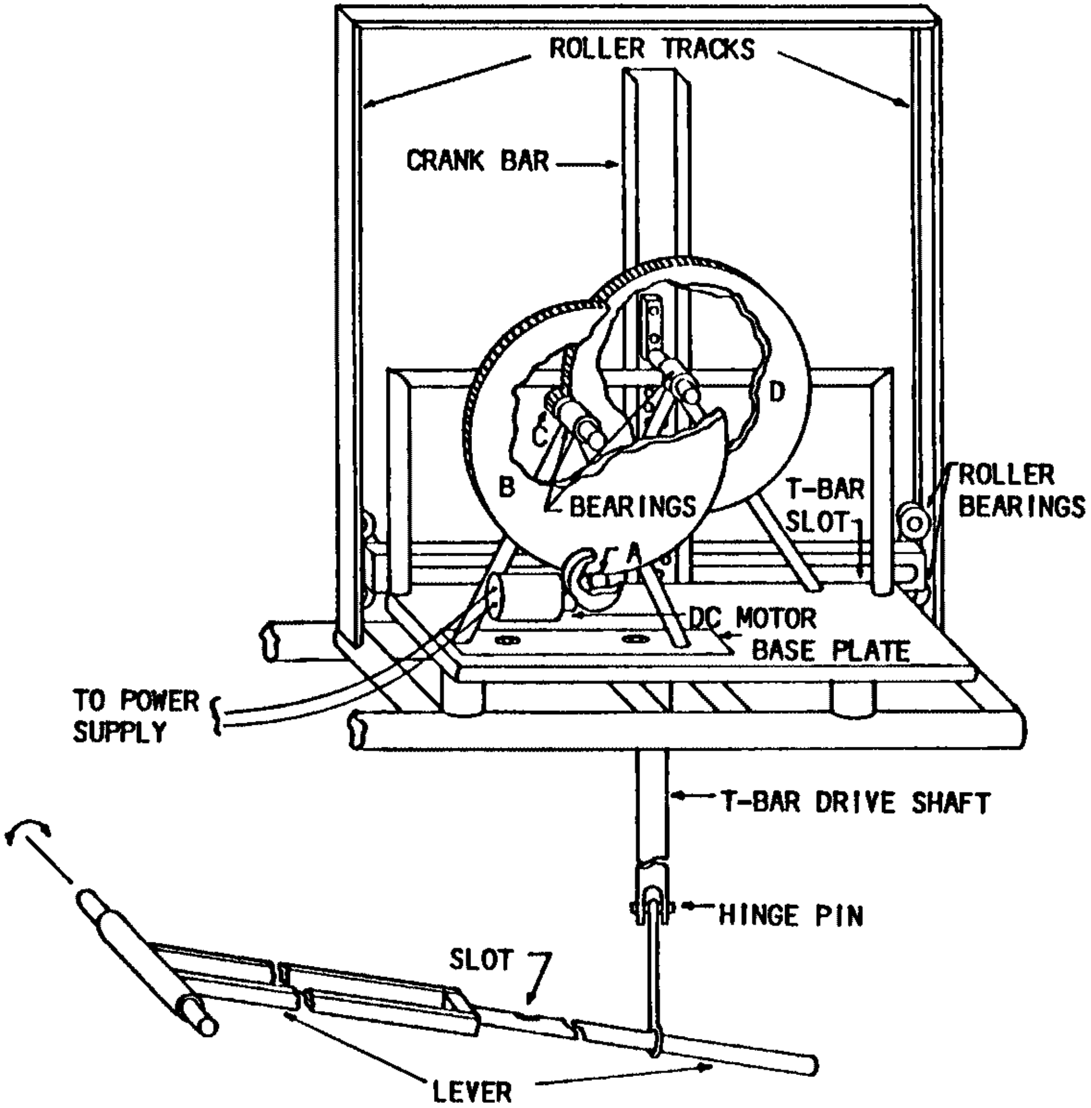
ROLLER TRACKS
CRANK BAR
D
C
B
BEARINGS
A
T-BAR SLOT
ROLLER BEARINGS
DC MOTOR
BASE PLATE
TO POWER SUPPLY
T-BAR DRIVE SHAFT
HINGE PIN
SLOT
LEVER

tion gears provide an approximate 100:1 reduction at the output to the reciprocating mechanism. The electric motor and gear A are attached to a steel mounting bracket on an A-frame gear support containing gears B and C. The A-frame gear support is composed of a bearing housing welded to two steel legs. The legs of the A-frame are welded to a base plate which is bolted to the mounting platform. Gear D and the crank bar of the reciprocating mechanism are mounted on a second A-frame gear support which is welded to the mounting platform. This A-frame is also supported by a rectangular, steel pipe, support frame which is welded to the mounting platform and to the bearing housing. Slotted bolt holes located in the base plate of the A-frame gear support containing gears B and C provide clearance for adjustment of proper meshing of gears C and D.

The reciprocating mechanism consists mainly of a crank bar, T-bar drive shaft, and lever. The reciprocating mechanism is driven by the electric motor through the reduction gears and crank bar. The aluminum crank bar is bolted to the shaft of output gear D. A T-bar drive shaft is connected to the crank bar with a crank pin. The crank pin consists of a bolt fitted with a roller bearing. The roller bearing is mounted in a slot on the horizontal cross member of the drive shaft. The drive shaft is composed of a steel pipe and welded at one end to a slotted, angle bar, cross member. The other end of the drive shaft is fitted with a hinge pin which passes through a hinged eye bolt attached to the lever. The drive shaft is constrained to move vertically by a bearing guide through which the vertical drive shaft passes and by a pair of roller bearings bolted to each end of the horizontal cross member. The rollers run on vertical tracks on either side of the horizontal cross member. The drive shaft guide is composed of a pipe fitted with ball bearing assemblies at either end and is welded to brackets on the support frame. The roller tracks are constructed of U-shaped steel bars and are welded to the support frame. The tracks are also supported by a crossbar which is welded to the tops of the tracks and by angle bar braces which are welded to the support frame and crossbar.

The motor and drive unit is coupled to the plunger and balancing unit by a lever. The lever is hinged to the support frame at one end and hinged to the drive shaft at the other end. The upper threaded rod of the plunger coupling assembly passes through a slot in the lever and is attached to the lever by a set of adjusting nuts. The adjusting nuts are attached to the upper threaded rod on either side of the lever slot. The lever is composed of two halves. The half nearest the support frame hinge point is constructed of two parallel angle bars. Each bar is welded to cross pipes at both ends. This half is welded at one end to a pipe-within-a-pipe hinge on the support frame. A space exists between the two parallel angle bars of this half of the lever to allow the cable extending from the balance weight and the cam to pass through the lever so that the cable has enough clearance to move from side to side as the balance weight moves up and down. To the other end of this lever half is welded a steel pipe which is fitted with the slot through which the upper threaded rod passes. The entire lever extends from its hinged position on the support frame to the bottom of the drive shaft. The lever is hinged to the drive shaft through the eye of the drive shaft eye bolt. This arrangement permits the lever to slide in the eye of the drive shaft eye bolt during operation. The slot in the lever provides clearance for slight horizontal movement of the upper threaded rod during operation. The slotted hole in the lever also permits vertical adjustment of the plunger and allows the cam to be set at any position, thereby eliminating the need to adjust the length of the drive shaft.

When the reciprocating mechanism is set in motion, the crank bar rotates as the crank pin roller bearing slides horizontally in the drive shaft slot. This motion forces the drive shaft to oscillate up and down, thus driving the lever and plunger up and down. The lengths of the strokes of the drive shaft and plunger are adjusted by changing the radius of rotation of the crank bar, thereby adjusting the tidal range in the flume. The crank bar contains numerous holes which allow the crank pin to be positioned at various lengths along the crank bar, providing various radii for the adjustment of the stroke length of the drive shaft. The tidal period is a function of the speed at which the crank bar rotates and is controlled by adjustment of the dc power supply voltage applied to the electric drive motor. Power to the electric motor may be turned on or off by switches on both the power supply and the motor mount bracket. The power supply is located on an equipment rack alongside the flume.

The tide generator is equipped with two bubble-type levels. One level is mounted on the side of the disk to indicate the maximum low water position of the cam-disk. The other level is mounted on the crank bar to indicate the high or low water positions of the crank bar. The levels are used when adjusting the tide generator for a particular tidal range and water level in the flume.

The tide generator is also equipped with two spring-loaded contact switches which are connected to the output terminals of a strip chart recorder. The recorder receives input signals from an electromagnetic current meter and a capacitance wave height measuring system, recording tide heights and current velocities during tidal flume operation. The contact switches are attached to one of the vertical roller tracks of the motor and drive unit. The switches can be placed at any location along the length of the track. In use, one contact switch is positioned at the top of the stroke of the drive shaft and the other is positioned at the bottom of the stroke of the drive shaft. The event marker on the strip chart recorder is triggered when the horizontal cross bar of the drive shaft depresses the spring-loaded lever on either switch, marking the times of high and low water at the entrance to the channel. This arrangement provides reference times for correlating tidal heights and current velocities.

Prior to performing any adjustments to the tide generator, the plunger and plunger coupling assembly should be raised above the headbay and attached to the plunger securing hook on the support frame. In this position the cam-disk is in its maximum low water position ($\theta = 90$ degrees) as indicated by the bubble-type level mounted on the side of the disk. This is also the proper position of the plunger when the tide generator is not in use. The procedure to adjust the tide generator for a particular water level and tidal range in the flume is carried out as follows:

1) Disconnected the lever from the drive shaft.
2) Adjust the sets of nuts on the upper threaded rod so that the lever is positioned at the bottom of the upper threaded rod.
3) Set the tidal range by unbolting the crank pin from the crank bar and re-bolting it to the crank bar through the crank bar hole corresponding to the stroke radius of the desired tidal range.
4) Connect the lever to the bottom of the drive shaft.
5) Position the upper threaded rod nuts on either side of the lever slot so that about 0.5 cm of play exists between the lever and the nuts.
6) Fill the flume with tap water to the desired low water level.
7) Lower the plunger to the low water level by turning the

lower threaded rod while preventing the upper threaded rod from turning. The plunger is in its proper low water position when the bottom of the plunger is just touching the water surface.

8) Remove the plunger securing hook from the plunger coupling assembly.
9) The tide generator is now ready for operation.

Figures 14 and 18 show profiles of tidal heights measured along the channel centerline with the capacitance wave height measuring system for channel lengths of about 24 m, 17 m, and 12 m.

Capacitance Wave Height Measuring System

Verification of the model in this investigation required that tidal wave height in the model be related to that in the prototype through a scale factor. Therefore, a means of determining the instantaneous free surface tidal wave elevations at a point as a continuous function of time was required. Tidal heights were measured along channel centerlines of the model and prototype using a variable-capacitance wave height measuring system. The measured tidal heights were taken as cross-sectional average heights.

A variable-capacitance wave height measuring system shown in Figure 7, was developed for use in the tidal flume and satisfied the following requirements: (1) capable of operating in tap water and accurately measuring relatively

Fig. 7. Wave height measuring system probe and detector units.

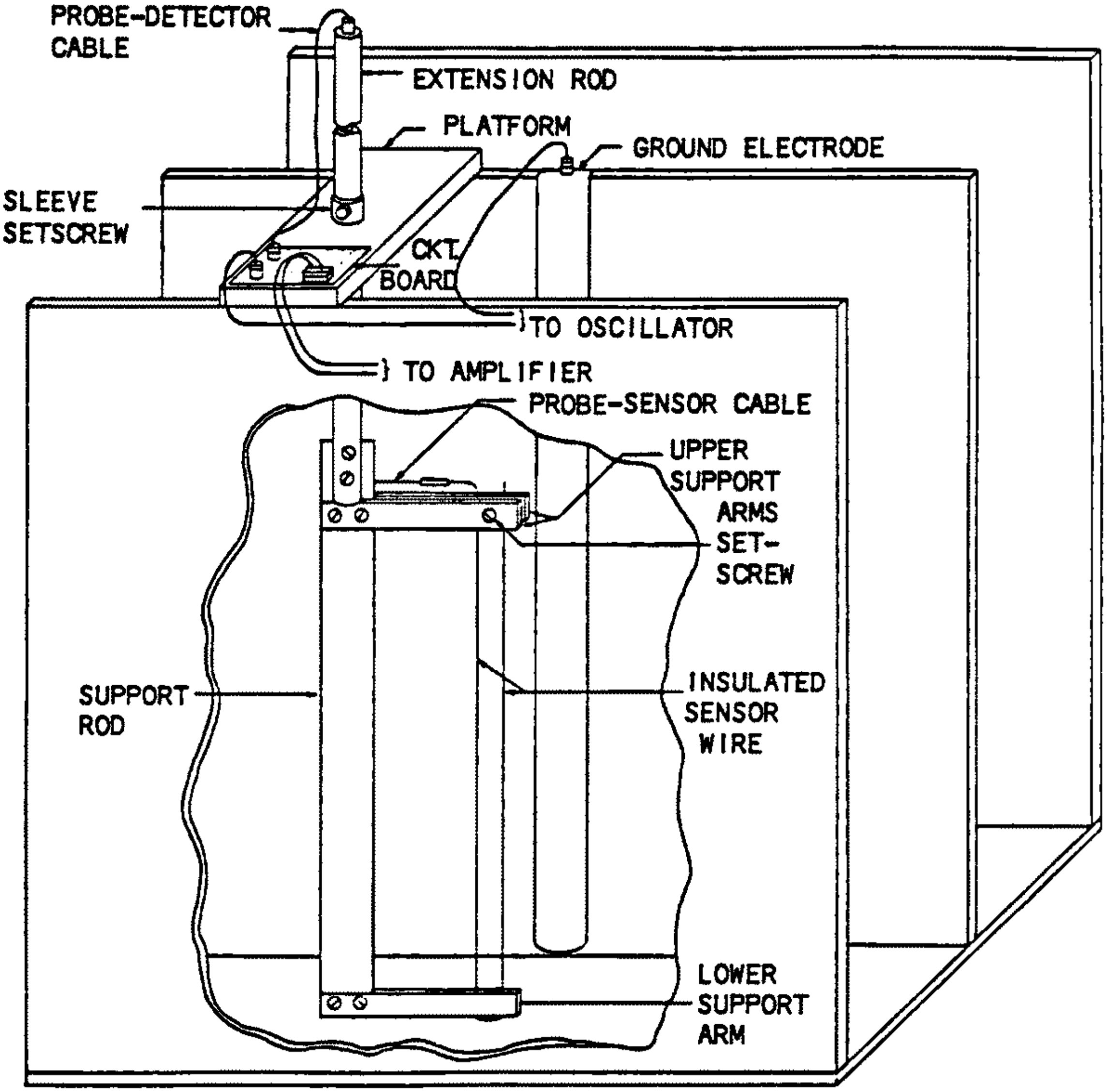
PROBE-DETECTOR CABLE
EXTENSION ROD
PLATFORM
GROUND ELECTRODE
SLEEVE SETSCREW
CKT. BOARD
TO OSCILLATOR
TO AMPLIFIER
PROBE-SENSOR CABLE
UPPER SUPPORT ARMS
SET-SCREW
SUPPORT ROD
INSULATED SENSOR WIRE
LOWER SUPPORT ARM

small amplitude waves having heights of 5 to 20 mm and periods ranging from about 2 to 15 minutes, (2) small sensing element to cause minor interference with the motion of the water, (3) high sensitivity, and a stable voltage output of associated circuitry that is a linear function of wave height and of conventional magnitude for operating standard auxiliary electronic equipment, and (4) simple construction using readily available components, easily used, and inexpensive.

Many methods have been developed to measure the heights of water waves in the laboratory (Grace 1970). These include: (1) sensors which operate above the water surface (e.g. lasers, electrical point gages with servo positioning mechanisms, and photographing waves against a grid, (2) sensors which operate below the water surface (e.g. pressure sensors), (3) sensors which float on the water surface (e.g. mechanical surface following floats), and (4) sensors which penetrate the air-water interface (e.g. resistance, inductance, conductance, and capacitance sensors).

The wave height measuring system developed for use in this investigation uses a capacitance sensor of the type which crosses the air-water interface. The capacitance measuring system consists of three essential components: a sensing element, a detector, and a display (voltmeter, strip chart recorder, or data logger). The system uses a partially immersed insulated wire for its sensing element. The impedance of the insulated wire to an applied, constant voltage, sine wave is almost entirely due to the capacitive reactance between the wire and the surrounding water. The alternating current signal modulated by the tidal wave profile, produces a voltage drop across a fixed capacitor in a capacitance voltage divider of which the sensor is one element. The resultant voltage drop is an amplitude modulated signal and is linearly proportional to the depth of immersion of the sensor wire. This signal passes through a voltage rectifier and is filtered, amplified, and applied to a strip chart recorder to produce a record of the tidal wave profile.

In use, four capacitance probes, each equipped with a separate measuring circuit, may be placed at desired positions along the channel centerline. The probes are connected to an oscillator, an amplifier, and a strip chart recorder through a probe selection switch which permits use of one probe at a time.

The capacitance sensor, in its simplest form, is a conducting wire which passes vertically through the air-water interface and is insulated by its dielectric coating from the water, as shown in Figure 8. The wire is mounted on a rigid frame and fixed in a position with reference to the mean level of the varying water surface. In the water, a bare electrode is installed at any location. Between this bare electrode and the sensor wire is a high frequency alternating current provided by a constant voltage, sine wave oscillator. The partially immersed insulated wire acts as a variable, concentric, cylindrical capacitor; the wire insul-

Fig. 8. Simplified electrical configuration of the wave height sensor.

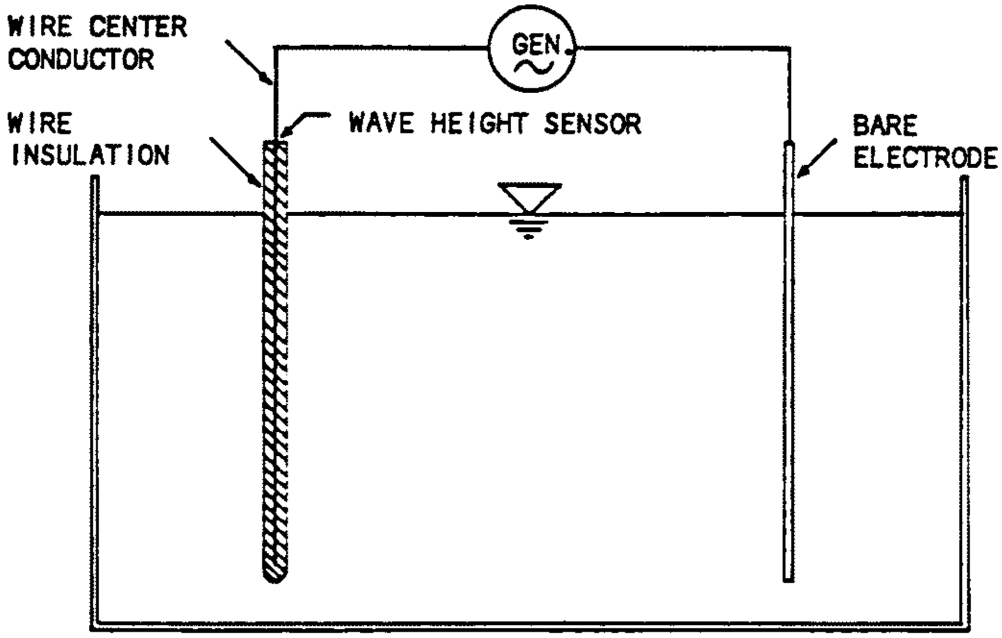
WIRE CENTER CONDUCTOR
GEN.
WIRE INSULATION
WAVE HEIGHT SENSOR
BARE ELECTRODE

ation is the dielectric and its plates correspond to the conductive wire and the surrounding water of reasonable conductivity. The capacitance between the conductive wire and the water, i.e. across the insulating dielectric, varies as the water level varies, i.e. as the wetted area of the conductive wire varies. This capacitance is directly proportional to the current flow between the conductive wire and the surrounding water. The capacitance per unit length of sensor wire C is given by the formula for a cylindrical capacitor

$$C = \frac{2\pi\epsilon_o k l}{\ln(D_2/D_1)} \tag{4}$$

where ϵ_o = the absolute dielectric constant

= 8.85×10^{-14} farad/cm^2

k = the specific dielectric constant of the wire insulating material

l = the length of wire immersed

D_1 = the diameter of the center conductor

D_2 = the diameter of the wire insulation

The capacitance and the current flow are linearly dependent on the depth of immersion of the sensor wire, provided that the wire insulation is uniform and that the wire end-effects are negligible (McGoldrick 1969). End-effects or fringing of the lines of force at the end of the capacitance sensor will have little effect on the linearity, if the length of the immersed sensor wire is much greater than the distance between the conducting wire and the surrounding water.

Ideally then, the variable capacitance sensor is a linear transducer. When connected to a detector that converts this varying capacitance or fluctuating current into a proportional fluctuating voltage, the wave form of any disturbance on the water surface, as it passes the sensor wire, would be duplicated.

In practice, the probe does not act as a pure capacitor as described above (McGoldrick 1969). For a capacitance probe consisting of an insulated wire near a grounded electrode, the simplified electrical configuration, as shown in Figure 9, is two terminal plates (conductive wire and ground electrode) with two intervening layers of dielectric (wire insulation and water), equivalent to the water resistance R_w in series with a parallel combination of the sensor wire capacitance C_p and leakage resistance of the wire insulation R_i. The series resistance is dependent on the conductivity of the surrounding water (e.g., tap water is less conductive than salt water) and on the distance between the sensor wire and the ground electrode. The parallel leakage resistance of the wire insulation is normally so large that it is negligible. However, coated wires will absorb water to some extent, causing a decrease in the leakage resistance of the insulation which may contribute significantly to the impedance of the probe. By a suitable choice of frequency for the electrical measuring current, the capacitance reactance

Fig. 9. Schematic of the simulation of complex resistance between the wave height sensor and the ground electrode.

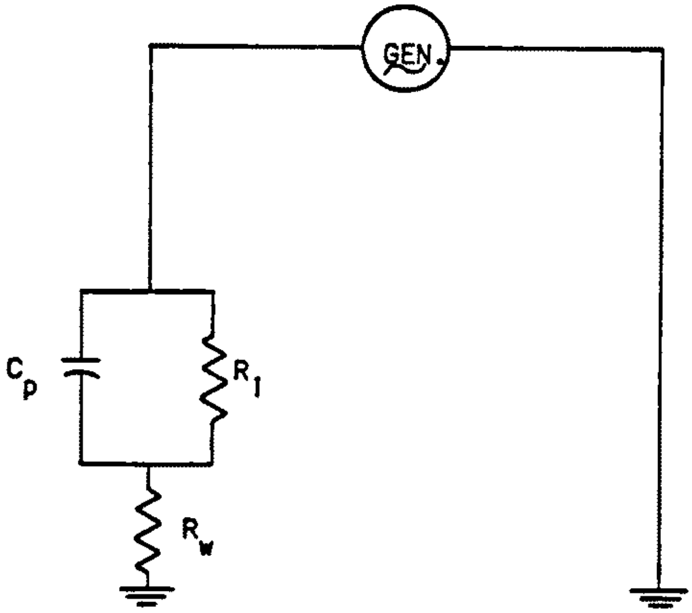
GEN.
C_p
R_1
R_w

of the sensor wire can be made large compared to the series resistance of the water, and thus, the series resistance of the water will be negligible. Furthermore, the leakage resistance is approximately inversely proportional to the depth of immersion; and if the distance between the sensor wire and the ground electrode is kept constant and the conductivity of the water is kept constant, then the series resistance of the water will remain constant. The net result is that the detector senses not just the capacitance of the immersed sensor wire, but the total impedance of the probe. This impedance is still inversely proportional to the depth of immersion, and thus, the response of the system is still linear.

The sensor wire used in this measuring system is a 32 AWG, enamel coated, magnet wire with a copper center conductor. The magnet wire has a center conductor diameter D_1 of 0.020 cm, an insulation diameter D_2 of 0.022 cm, and a specific dielectric constant of the enamel coating k of 4. Substitution of these values into equation (4) yields a sensor wire capacitance per unit length C of 23 pf/cm. This particular wire was chosen because it was readily available, inexpensive, and small in diameter. A sensor wire of small diameter is necessary to inhibit the formation of flowback films on the wire (Wilner 1960). Under dynamic conditions in the tidal flume, the water surface is typically flat as the water rises around the sensor wire, but, as the water recedes, viscosity prevents the water from leaving the wire instantaneously. Consequently, a flowback film is left on the sensor wire which acts as a conducting sheath to the main water body, giving a spurious increase in capacitance which may cause the measuring system to indicate a water level higher than the main level a short distance away from the sensor wire. Capillary pressure is responsible for the removal of the flowback film and increases as the radius of the sensor wire is decreased. Wilner (1960) found experimentally that the influence of flowback films on wave height measurements is negligible if sensor wires of 26 AWG (D_1 = 0.041 cm) and finer are used. A disadvantage of the enamel coated sensor wire is its property of absorbing water and changing the dielectric properties of the insulation, i.e. the leakage resistance decreases and the dielectric constant increases, causing an increase in capacitance of the immersed sensor wire (Tucker and Charnock 1954). A decrease in leakage resistance may prevent the immersed sensor wire from appearing as a pure capacitor to the detector circuitry. Figure 10 shows the long term drift in the voltage output of the measuring system in tap water for the period after immersion of the probe. A considerable increase in output voltage occurs in the beginning, coming to a standstill in about 15 minutes. Thus, in practice, the sensor wire is soaked for at least 15 minutes before use, thereafter, no further difficulty results due to absorption.

The capacitance probe shown in Figure 7, consists of a 42 cm long, looped, 32 AWG magnet wire stretched vertically

Fig. 10. Wave height measuring system output voltage variation with time after submergence of probe in tap water.

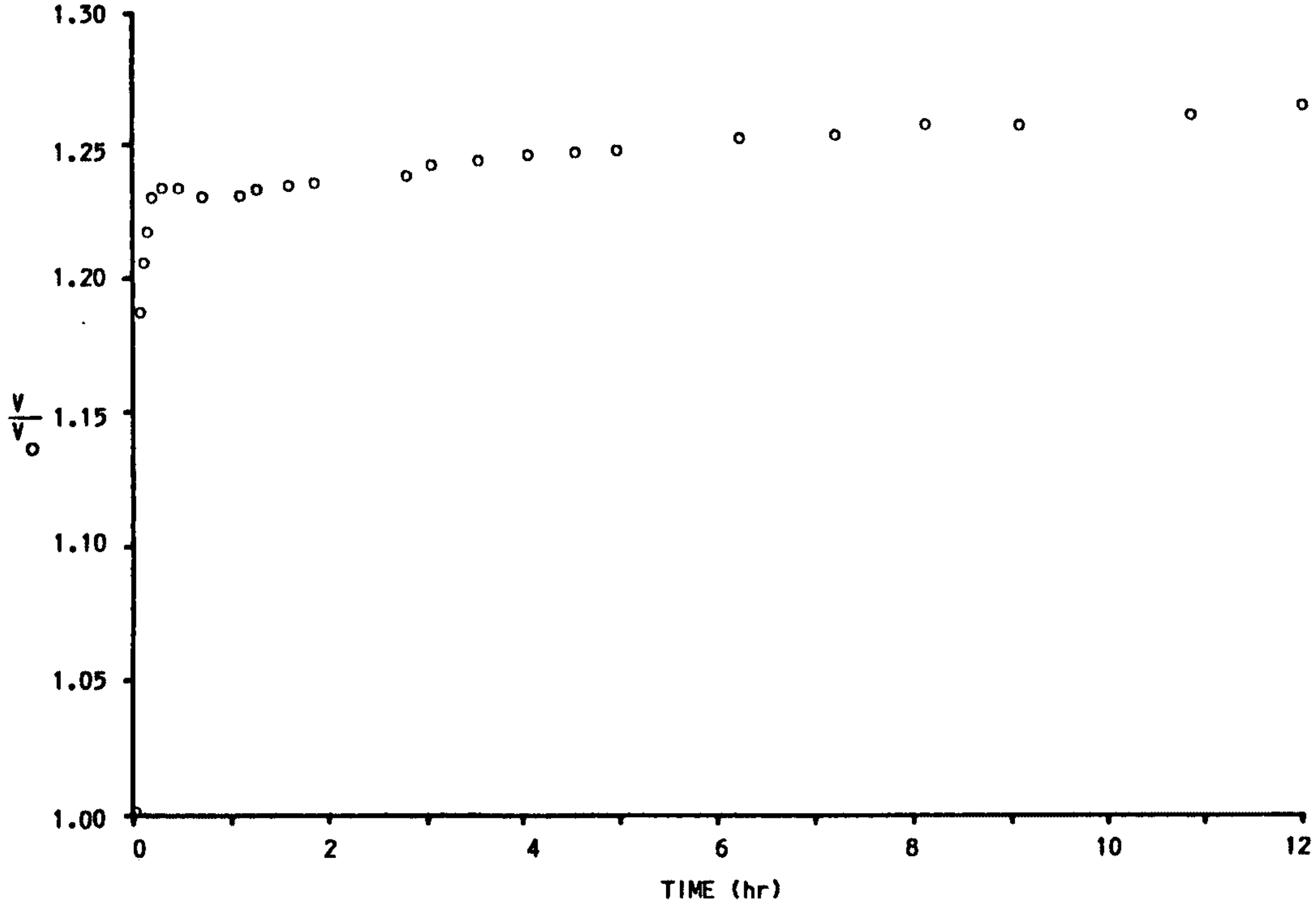
1.30
1.25
1.20
1.15
1.10
1.05
1.00
$\frac{V}{V_o}$
0
2
4
6
8
10
12
TIME (hr)

through the water surface between two acrylic plastic support arms. Each arm is 0.5 cm thick, 1.3 cm wide, and 5 cm long. For very shallow depths (less than approximately 1 cm), the capacitance probe must be fitted with a narrower, lower support arm. The support arms are spaced 16.5 cm apart and are mounted on a thin, anodized aluminum, support bar which is 0.1 cm thick, 2.3 cm wide and 21.7 cm long. The sensor wire is looped and threaded through two holes spaced 0.8 cm apart in the lower support arm to avoid the necessity of insulating the lower end of the sensor wire from the water. The two ends of the sensor wire are sandwiched between two halves of the upper support arm. The ends are clamped firmly in place with a set screw which passes between the sensor wires and through both halves of the upper support arm. A space of 3.5 cm is allowed between the inner sensor wire and the support bar to minimize error in measurements caused by the reflection of capillary waves from the support bar. A hollow, acrylic plastic rod, 1 cm in diameter and 39 cm long, is attached to the upper end of the support bar. The top of this extender rod is fitted with a terminal post to which is solder a length of insulated hook up wire, 41 cm long. The wire passes down through the hollow extender rod to the upper support arm where it is soldered to one end of the sensor wire. This arrangement allows damaged sensor wires to be easily replaced. The sensor wires are quite durable when subject to water action, however, they are easily damaged by contact with solid objects.

The common types of detector circuits used to transform the variable probe capacitance to analog output voltages involve the application of an ac signal to the capacitance sensor and use the sensor wire (1) as one element in a voltage divider (Timpy 1982, Blair 1976, and Anderson et al. 1972), (2) in one leg of a bridge circuit to balance a bridge (Moore 1964), (3) in a tuned LC circuit for comparison to a reference frequency (McGoldrick 1969, Killen 1955, and Tucker and Charnock 1954), or (4) in an RC oscillator to control its repetition rate (Wittenbury et al. 1959). The detector circuit used with the capacitance sensor in this study is a modified version of the detector circuit used by Blair (1976) and uses a capacitive voltage divider as a measuring circuit.

A block diagram and circuit diagram of the capacitance wave height measuring system are shown in Figures 11 and 12. A sine wave of constant 15 volts ac and frequency of 20 khz is generated by a General Radio Model 1310A Wein Bridge oscillator. The oscillator frequency, in combination with the oscillator output, was chosen so that (1) the water resistance of the main body of water surrounding the sensor wire R_w is small compared to the capacitive reactance of the immersed sensor wire Xc_p and (2) a usable output voltage is produced for the display equipment. Thus, the impedance of the probe is almost entirely due to the capacitive reactance between the wire and the surrounding water. The equations for the impedances of a coaxial system are well known

Fig. 11. Block diagram of the wave height measuring system.

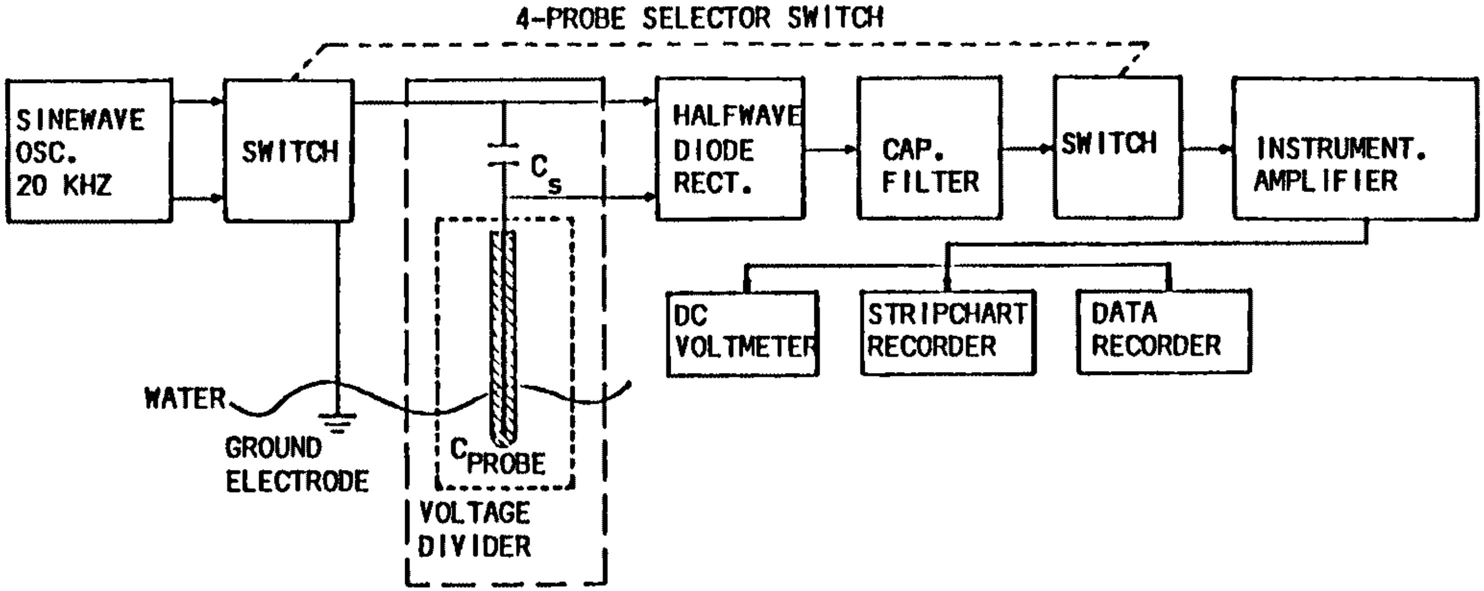
4-PROBE SELECTOR SWITCH
SINEWAVE OSC. 20 KHZ
SWITCH
C_s
HALFWAVE DIODE RECT.
CAP. FILTER
SWITCH
INSTRUMENT. AMPLIFIER
DC VOLTMETER
STRIPCHART RECORDER
DATA RECORDER
WATER
GROUND ELECTRODE
C_{PROBE}
VOLTAGE DIVIDER

Fig. 12. Circuit schematic of the detector unit of the wave height measuring system.

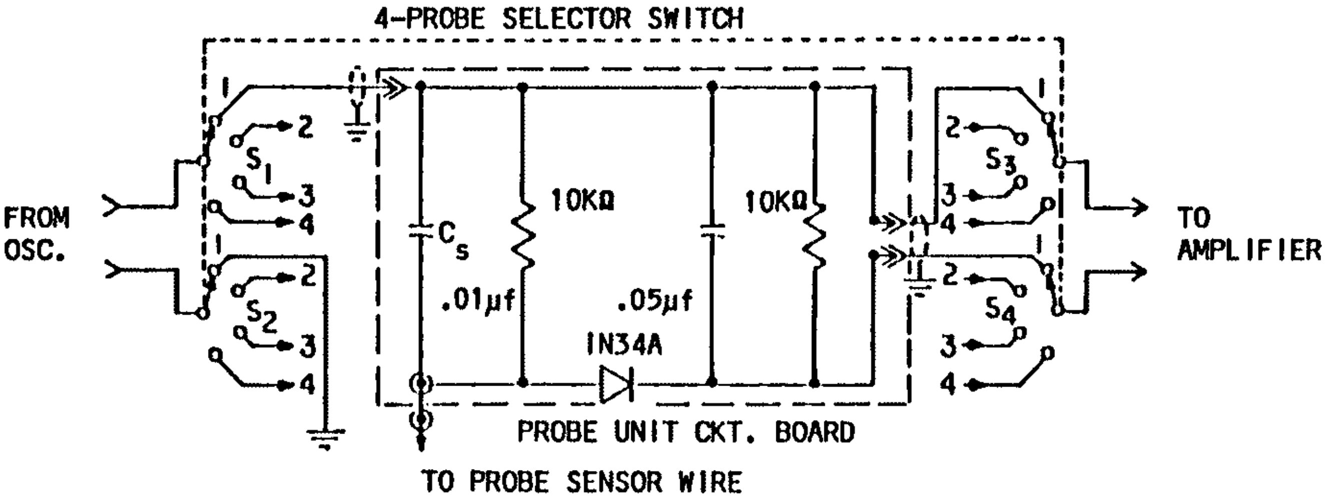
4-PROBE SELECTOR SWITCH
FROM
OSC.
1
2
S_1
3
4
1
2
S_2
3
4
C_s
.01μf
10KΩ
IN34A
.05μf
10KΩ
1
2
S_3
3
4
1
2
S_4
3
4
TO
AMPLIFIER
PROBE UNIT CKT. BOARD
TO PROBE SENSOR WIRE

(Tucker and Charnock 1954, and Wilner 1960).

$$R_w = \frac{\ln(D_3/D_2)}{2\pi\sigma_w l} \tag{5}$$

and

$$Xc_p = \frac{1}{2\pi f C_p} = \frac{\ln(D_2/D_1)}{4\pi^2\epsilon_\circ l k f} \tag{6}$$

where D_3 = the distance between the sensor wire center conductor and the ground electrode

σ_w = specific conductivity of tap water

= 5×10^{-5} ohm^{-1}cm^{-1}

f = the frequency of the oscillator

Substitution of the actual values used in the design of the capacitance probe given in Table 3, into equations (5) and (6) yields a ratio R_w/Xc_p of 0.06, as $Xc_p >> R_w$ for the chosen frequency of 20 khz. Thus, the series resistance of water is negligible and the capacitance of the sensor wire is nearly proportional to the depth of immersion.

Table 3. Summary of data for the capacitance wave probe design.

k = 4

D_1 = 0.020 cm

D_2 = 0.022 cm

f = 20 kHz

The constant voltage sine wave is applied to a capacitive voltage divider measuring circuit consisting of two capacitors in series, one is a 1 x 10^4 pf, fixed capacitor C_s and the other is formed by the looped sensor wire which has a capacitance per unit length C of 46 pf/cm. That is, the capacitance per unit length of the looped (doubled) sensor wire probe is twice the capacitance of a single sensor wire configuration. If C_s is made much larger than the capacitance of the probe C_p, i.e., if the capacitive reactance Xc_p of the immersed sensor wire is made much greater than the capacitive reactance Xc_s of the fixed capacitor, then the voltage drop across C_s is directly proportional to the capacitance C_p which varies with the depth of immersion. For example, let the maximum capacitance obtained by the immersed sensor wire C_p equal 92 pf at high water when the tide generator is operating with a tidal range of 2 cm. This corresponds to a total length of immersed sensor wire of 4 cm. Substituting the values for C_s and C_p given above, into equation (6) yields a ratio $Xc_s/Xc_p = 0.01$, where $Xc_p \gg Xc_s$. Blair (1976) used a resistor in a voltage divider measuring circuit in place of the capacitor C_s. The advantage of using the capacitor C_s in place of a resistor is that, should the oscillator frequency vary, then the impedances of the capacitors C_p and C_s will vary proportionately, preventing the output voltage and the sensitivity from varying.

The voltage across capacitor C_s will be an amplitude modulated sine wave modulated by the tidal wave profile. This signal is rectified by a half wave diode rectifier to eliminate the 20 khz carrier frequency and to detect the amplitude modulated signal. The half wave rectifier is followed by a capacitive filter with a ripple factor of 0.03 to further reduce the alternating component of the rectified wave form so that the output is primarily a dc voltage. This dc voltage is amplified by a linear instrumentation amplifier with a gain of 4. The amplified dc voltage varies linearly with the depth of probe immersion and is applied to a Bausch & Lomb V.O.M. 10, single-trace, linear, strip chart recorder and a Hewitt-Packard, digital dc voltmeter for display. The dc output voltage has also been applied to an InterOcean Model 680, digital, data recorder for computer processing of data from a magnetic tape.

The fixed capacitor in the measuring circuit voltage divider, the half wave diode rectifier and the capacitive filter, and the load resistor are all contained on a 4.5 cm square, component board which is attached to the probe mounting platform shown in Figure 7. This portion of the detector circuit is mounted directly adjacent to the probe to avoid problems with the "dead" capacitance of the cables leading to the sensor (Wilner 1960). The wooden mounting platform, measuring 2 cm by 5 cm by 40 cm, rests on the top of the flume. A plastic sleeve is fitted through the center of the platform through which the probe extender rod passes. The depth of immersion of the sensor wire is adjusted by sliding the extender rod through the plastic sleeve. The extender rod is clamped in place by a a set screw which passes through the side of the plastic sleeve. The sensor wire is connected to the detector circuitry by a 45 cm long, insulated, wire cable containing an alligator clip at both ends. One end of the cable is clipped to the probe terminal post at the top of the extender rod and the other end is clipped to a terminal post on the circuit board.

The oscillator, instrumentation amplifier, and display equipment are contained on a portable equipment rack located alongside the flume. All wire cables connecting the electronic equipment on the portable equipment rack to the probe unit circuitry on the flume are shielded to ground and fed through wire hangers along the outside of the channel. Coaxial cables of the type RG 174/U run from both binder posts of the oscillator; one of the cable is fitted with a single prong connector and is plugged into a jack on the probe unit circuit board, and the other cable is fitted with a thin, galvanized electrode, measuring 1.9 cm by 30.5 cm, which fits over the edge of the channel adjacent to the probe sensor wire and extends to the bottom, inside corner of the channel. The probe is placed along the channel centerline at a distance of 14 cm from the ground electrode. A two conductor audio cable fitted with a two prong connector and plugged into a receptacle on the circuit board runs to the binder posts of the instrumentation amplifier. All display equipment is connected to the output of the instrumentation amplifier.

The measuring system is designed to accommodate four probe units, each with 8 m of cable. A terminal box containing a probe selection switch S (rotary wafer), oscillator and amplifier terminals, and a ground terminal, interfaces all probe units with the rack of associated electronic equipment. The terminal box is hooked to the outside of the flume next to the equipment rack. All cable shielding is connected to the ground terminal on the terminal box. The probe selection switch permits selection and use of one probe at a time.

The overall performance of the variable-capacitance wave height measuring system was determined through static and dynamic response tests which were conducted in tap water in the tidal flume. Sensitivity and linearity of response of the system was determined by a static calibration of each probe. For calibration, a probe was removed from the probe mounting platform and transferred to a rack and pinion on top of the channel. The rack and pinion was graduated in 0.1 mm increments. The probe was immersed to a depth of 6 cm in smooth water and soaked before calibration for at least 15 minutes, until the output voltage on the voltmeter had stabilized. The depth of immersion was then decreased stepwise in 0.5 cm intervals over a 4 cm range while the corresponding voltages were recorded from the voltmeter. To test the repeatability of the response, the probe was immediately returned to its original depth of immersion by increasing the depth of immersion in 0.5 cm intervals while recording the output voltages. Static response tests were also conducted at various oscillator frequencies in water of various salt concentrations using various oscillator frequencies. The overall results for the saltwater tests showed satisfactory linearity but lacked repeatability. The poor response of the probe in saltwater may have been a result of adhesion of salt to the sensor wire, thus changing the electrical properties of the wire insulation. A typical static response calibration curve for tap water is shown in Figure 13. The overall sensitivity of the system was 208 mv/mm and the mean deviation of the static calibration curve from a straight line was 0.08 mm, typical of all probe calibrations.

The dynamic response of the system was determined by comparing tide heights measured with the capacitance probe to those measured with a manual point gage. A Lory Type C point gage graduated in 0.1 mm increments was positioned along the channel centerline at a distance of 10 cm from the sensing wire of the probe. Point gage measurements were taken every 15 seconds and compared to wave height profiles recorded on the strip chart recorder (set for a full scale reading of 1 volt and a chart speed of 1 inch/min). Typical dynamic response curves are shown in Figure 14 for a channel length of 24 m, mean water level of 6 cm, tidal range of 1.2 cm, and tidal period of 5 minutes. The comparisons between wave heights measured with the point gage and those

Fig. 13. Linearity between output voltage and probe displacement in tap water for static calibration of the wave height measuring system.

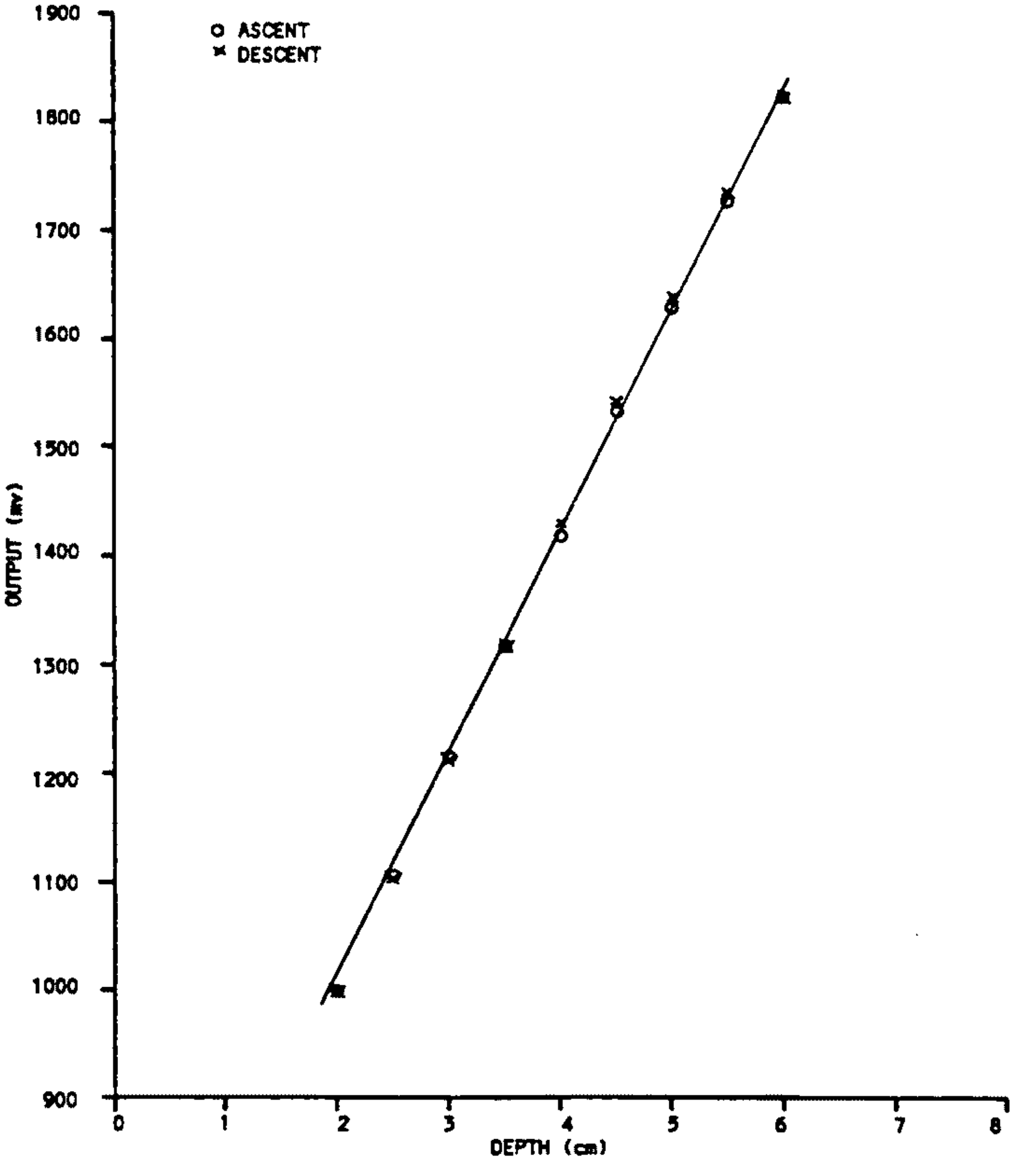
○ ASCENT
× DESCENT
OUTPUT (mv)
1900
1800
1700
1600
1500
1400
1300
1200
1100
1000
900
DEPTH (cm)
0
1
2
3
4
5
6
7
8

Fig. 14. Dynamic response in tap water of the wave height measuring system to a small amplitude wave.

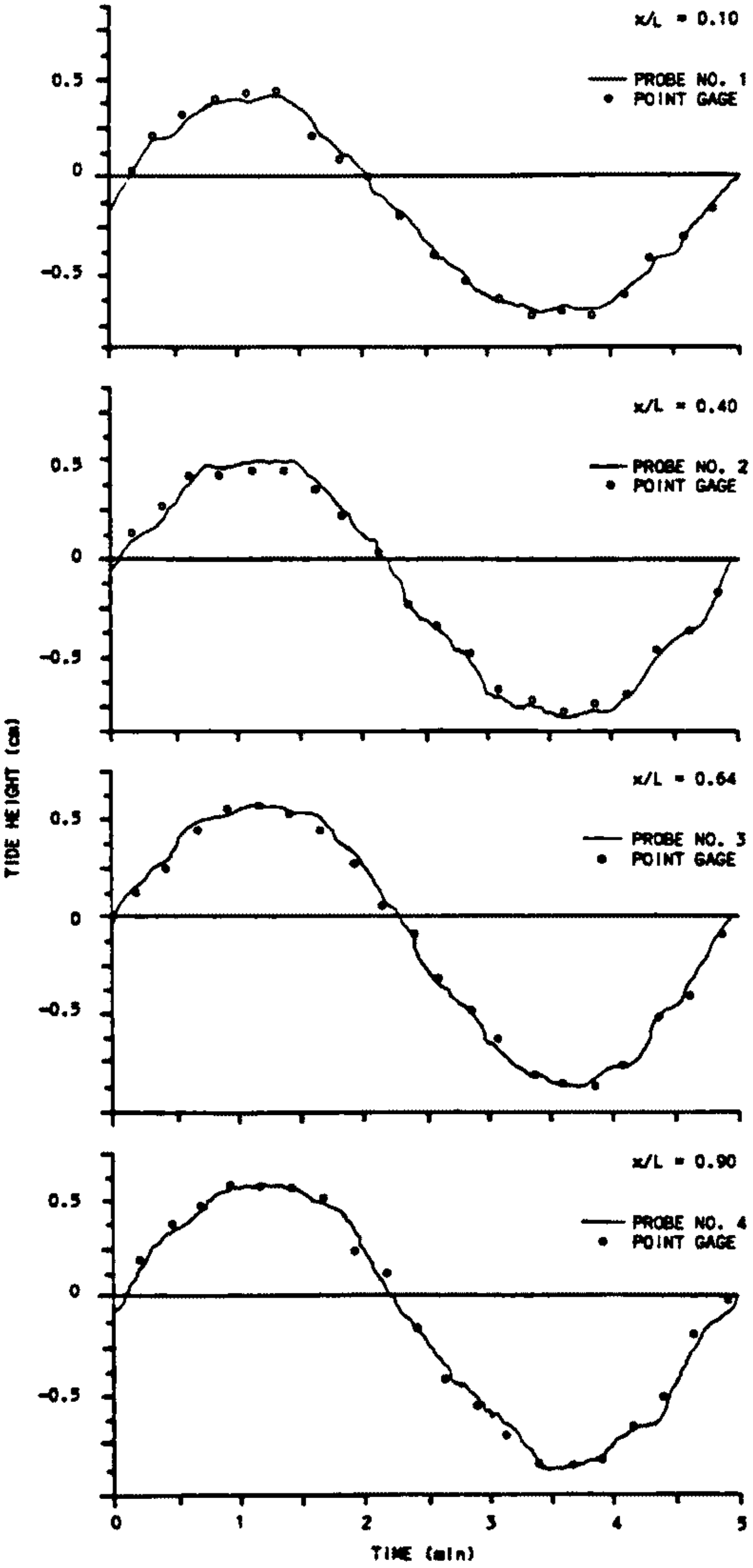
x/L = 0.10
PROBE NO. 1
POINT GAGE
x/L = 0.40
PROBE NO. 2
POINT GAGE
x/L = 0.64
PROBE NO. 3
POINT GAGE
x/L = 0.90
PROBE NO. 4
POINT GAGE
0.5
0
-0.5
TIDE HEIGHT (cm)
0
1
2
3
4
5
TIME (min)

measured with the capacitance probes showed good agreement (Fig. 14).

Current Velocity Measurement

Verification of the model in this investigation required that tidal current velocity in the model be related to that in the prototype through a scale factor. Therefore, a means of determining the instantaneous tidal current velocities at a point as a continuous function of time was required. Tidal current velocities were measured along the channel centerlines of the model and prototype using a Marsh-McBirney Model 523 electromagnetic water current meter. The measured current velocities were taken as cross-sectional average velocities.

The electromagnetic current meter operates on Faraday's principle of electromagnetic induction, which states that "a conductor (the water) moving in a magnetic field (generated within the current meter probe) produces a voltage that is proportional to its velocity" (Cushing 1974). The instrument consists of a current velocity probe and a signal processor. To obtain velocity profiles over a tidal cycle, the signal from the signal processor (0 to 1 volt, corresponding to current velocities of 0 to 3.05 m/s) was fed to a Bausch & Lomb V.O.M. 10, single-trace, linear, strip chart recorder (set for a full scale reading of 100 mv and a chart speed of 1 inch/min).

The current meter probe shown in Figure 15, consists

Fig. 15. Marsh-McBirney Model 523 electromagnetic current meter probe assembly.

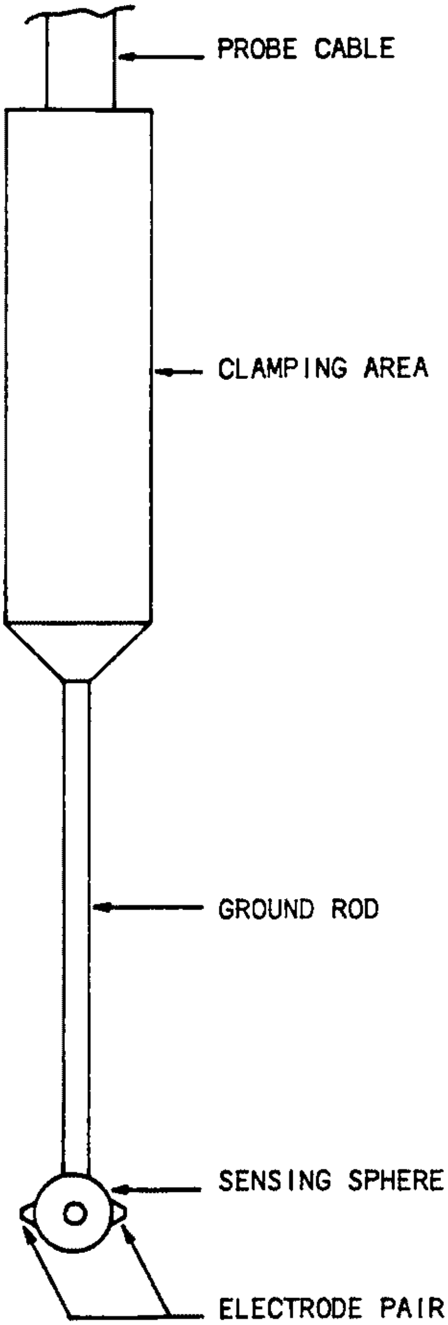
PROBE CABLE
CLAMPING AREA
GROUND ROD
SENSING SPHERE
ELECTRODE PAIR

of a 9.5 mm diameter sphere containing an electromagnet and two pairs of external sensing electrodes, a Y-electrode pair and an X-electrode pair in contact with the water. The sphere is permanently mounted on the end of a 3.2 mm diameter, stainless steel, ground rod . A clamping area is provided at the other end of the ground rod, 7.6 cm from the center of the sphere. In use, the clamping area is fitted with a machined mounting tube which is clamped to a ringstand and positioned on top of the flume.

In general, the principle of operation of the electromagnetic current meter can be described as the interaction of three mutually orthoganal vectors: the magnetic field created by an ac electromagnet within the sensor, the flow velocity around the sensor, and the induced electric field. The magnetic field is produced, so as to be parallel to the longitudinal axis of the probe. The electrode pairs in the wall of the sensing sphere detect voltages caused by water flowing past the sensor in a plane normal to the longitudinal axis of the probe. Two pairs of electrodes are used, so that the velocity $\mathbf{U}$ can be resolved into its two components $(u_x)^2$ and $(u_y)^2$, where $u_x = |\mathbf{U}| \cos \theta$ and $u_y = |\mathbf{U}| \sin \theta$. The current velocity magnitude is $U = [(u_x)^2 + (u_y)^2]^{1/2}$. The flow sensing volume is a sphere with a diameter of 2.86 cm, equal to three probe diameters. The instrument time constant of 5 seconds causes instantaneous velocity measurements to be averaged over a damping period of 5 seconds. Thus, there is a time lag of 5 seconds between the output voltage and the measured current velocity.

For the measurement of current velocities in the tidal flume, the sensing sphere was immersed to mid-depth below static low water and oriented so that the x-axis was perpendicular to the longitudinal axis of the channel and the y-axis was parallel to the longitudinal axis of the channel. The analog voltage output of the signal processor presents the flow as two orthoganal components; the X-electrode pair sensed transverse (lateral) channel velocities, while the Y-electrode pair sensed longitudinal channel velocities. Because the channel depth-to-width ratio was relatively small for both the model and the prototype, the channel sidewalls had a negligible effect on the cross-sectional velocity distribution, and therefore, transverse velocities were nearly zero. Only the output voltages detected by the Y-electrode pair, proportional to model and prototype longitudinal current velocities, were recorded and used for verification.

The instrument was factory calibrated in a recirculating water tunnel. Current velocities are determined to within about ±2 percent and the low velocity resolution is about 0.05 cm/s.

Water Sampling System

The longitudinal distributions of marked fluid in the model and in the prototype were measured by analyses of dye-water samples collected along channel centerlines using water sampling probes. The measured dye concentrations were taken as cross-sectional average concentrations.

Water samples were withdrawn by suction, simultaneously, through the activation of a vacuum pump sampling system (Scheffner 1981). The vacuum sampling system shown in Figure 16, consists mainly of (1) a vacuum pump and reservoir, (2) a vacuum manifold with associated sampling tube probes and test tube sample collectors, and (3) an overflow system. Vacuum manifolds were donated by the U.S. Army Corps of Engineers upon disassembly (1983) of the WES Chesapeake Bay hydraulic model.

For the dispersion tests in this investigation, two vacuum manifolds and two vacuum pumps were used along with a single vacuum reservoir. The vacuum manifolds are mounted on tripod stands and stand 1.5 m high. Both manifolds were positioned alongside the channel at distances of 3 m (manifold No. 1) and 9 m (manifold No. 2) from the headbay. The vacuum pumps and reservoirs were located between the two vacuum manifolds. Each manifold has the capacity to withdraw 24 water samples, simultaneously, however, only eight sample positions on manifold No. 1 and eight positions on manifold No. 2 were used in the tests.

Both vacuum pumps are powered by 110 volts ac through a single electrical switch, allowing both pumps to be tuned on or off, simultaneously. The vacuum lines leading from the pumps are 6.4 mm-ID surgical tubes and are connected to tee fittings at the top of the reservoir. One end of each tee

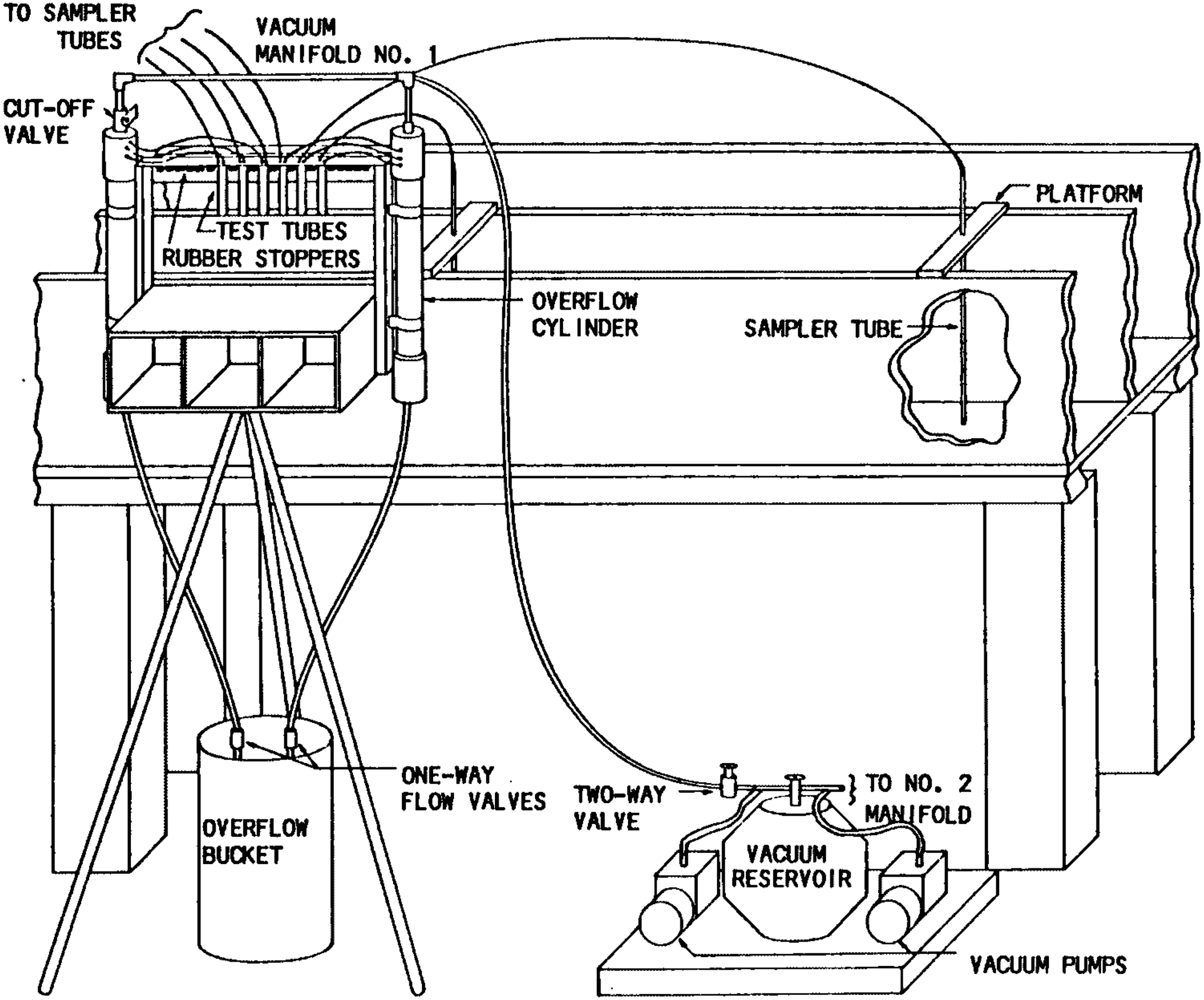
TO SAMPLER TUBES
VACUUM MANIFOLD NO. 1
CUT-OFF VALVE
PLATFORM
TEST TUBES
RUBBER STOPPERS
OVERFLOW CYLINDER
SAMPLER TUBE
ONE-WAY FLOW VALVES
TWO-WAY VALVE
TO NO. 2 MANIFOLD
OVERFLOW BUCKET
VACUUM RESERVOIR
VACUUM PUMPS

fitting is connected to a two-way valve. Position #1 of the two-way valves opens the vacuum lines between the vacuum reservoir and the vacuum manifolds. Position #2 closes the vacuum lines between the vacuum reservoir and the vacuum pumps and simultaneously opens the vacuum lines leading from the vacuum manifold to ambient pressure. Therefore, in position #2, the two-way valves serve as relief valves to eliminate the vacuum remaining in the lines after water samples are withdrawn, thus stopping the withdrawal of water. Position #2 also facilitates the creation of a vacuum in the vacuum reservoir when water samples are not being withdrawn. The vacuum reservoir aids in decreasing sample withdrawal time and acts as a moisture trap to prevent water from entering the vacuum pumps. The vacuum reservoir is composed of a 27 liter, metal, freon container.

The vacuum pumps and reservoir are connected to the vacuum manifolds through 12.7 mm-ID polybutylene tubes which extend from the two-way valves to tee fittings on the top of the vacuum manifold overflow cylinders. The two 1-liter overflow cylinders on each vacuum manifold are joined through 12.7 mm-ID polybutylene tubes. From the top of each overflow cylinder, 1.6 mm-ID polybutylene tubes branch into 10 ml (13mm x 100mm) sample test tubes through size 00 rubber stoppers permanently mounted in holes on a plastic support bar on the manifolds. The test tubes are easily fitted on the rubber stoppers which provide air-tight seals when withdrawing water samples. The test tubes are easily removed after water samples have been collected. Each test tube holds about 8 ml of sample water when fitted on the rubber stoppers. Another length of 1.6 mm-ID polybutylene tube passes from each test tube through the rubber stopper and to a sampling probe mounted in a wooden, portable platform on top of the flume. Each sampling probe is composed of a 39 cm long by 3 mm-ID glass tube fitted with a thin, 5 mm long by 1 mm-ID glass, pipette stem to minimize disturbance of the flow. The thin pipette stem penetrates the water surface and extends to the desired sampling depth. The sampling tube is fitted through a hole in the wooden platform and is easily adjusted to the desired sampling depth.

A 12.7 mm-ID polybutylene tube extends from the bottom of each overflow cylinder, passing through a one-way flow valve (flapper-type), and to an overflow bucket. The overflow system permits water which has overflowed from the sample test tubes to collect in the overflow cylinders and to drain from the vacuum system through the one-way flow valve and into the overflow bucket when the vacuum in the system is released. This prevents water from being sucked into the vacuum reservoir or vacuum pumps. A cutoff valve is provided on one overflow cylinder of each manifold in the event that only half of the manifold is to be used.

The vacuum sampling system is operated and functions as follows. With both two-way valves in position #2 and both vacuum pumps activated, a vacuum is created in the vacuum reservoir in about two minutes. Both two-way valves are then switched to position #1, causing an instantaneous withdrawal of water samples as the flappers close on the one-way flow valves. With 16 sampling probes in place in the flume, water samples are withdrawn at slack currents for a duration of about 7 seconds. During this withdrawal period, the sample test tubes are completely filled within the first 5 seconds. An additional 2 seconds of withdrawal time allows the sample test tubes to overflow (approximately 3 ml) and to be flushed of any water which may have been trapped in the vacuum lines (approximately 2 ml) between the test tubes and the sampling probes from the previous sample withdrawal. The overflow collects in the overflow cylinders. To prevent the vacuum lines from sagging and consequently trapping water, the vacuum lines between the sample test tubes and the sampling probes are elevated by nylon lines which extending from the overhead. In this way, the gravity drain process is accelerated when sample withdrawal is stopped. However, some water still remains in the lines after the withdrawal of a sample as a result of capillarity. The withdrawal of water samples is stopped by switching the two-way valves to position #2, and thereby, eliminating the vacuum in the system. At this time the flappers in the one-way valves open and allow the water in the overflow cylinders to drain into the overflow buckets. The vacuum pumps are then turned off after a vacuum has been created in the vacuum reservoir. After the water samples are collected, the sample test tubes are removed from the manifolds, stoppered, and placed in test tube racks. The tripod stand is equipped with test tube rack holders which hold racks of both empty and full test tubes. Empty test tubes are then fitted on the manifolds in preparation for the next sampling run.

Tracer Dye Concentration Measurement

Because the model and prototype longitudinal dispersion tests in this investigation were to be conducted in a constant-density flow system, Rhodamine WT fluorescent dye was used as a tracer. Concentration gradients without density gradients are readily produced with fluorescent tracer-dye. Rhodamine WT was developed specifically for use in physical models because it has the best solubility of all fluorescent tracer-dyes and does not readily adsorb to the sidewalls and bottom of models (Turner Designs 1982). Rhodamine WT dye is a conservative tracer-dye and is supplied by the manufacturer as a 20% aqueous solution of specific gravity 1.2.

A Turner Model 111 filter fluorometer with a far ultraviolet (uv) lamp source and matched filter arrangement (primary color spec. No. 546 and secondary color specs. No. 3-66 and No. 4-97) was used to detect the fluorescence of tracer-dye in water samples collected in the dispersion experiments of this investigation. Water samples were collected with the water sampling system in 10 ml test tubes, 13 mm x 100 mm, which fit into the sample holder of the fluorometer. In the fluorometer, the sample converts a fraction of the light which reaches it, into light of a new wavelength; this re-emitted light is then measured in fluorometric units (f.u.). The fraction converted, hence the emitted light, is proportional to the concentration. Turner Designs (1975) reported that the meter reading of the fluorometer, i.e. the measured, emitted light from a water sample containing dye, is linearly proportional to the concentration of Rhodamine WT dye from the smallest detectable concentration to about 200 ppb. The fluorometer is accurate to within 0.3 fluorometric units.

The fluorometer was calibrated to determine the dye concentration range for which the meter reading of the fluorometer was linearly proportional to the dye concentration. All ranges of the fluorometer (X30, X10, X3, and X1) were calibrated, from the most sensitive X30 to the least sensitive X1, against standards made by diluting the manufacturer's 20% aqueous stock dye solution with aged tap water. The resulting calibration curves for each range of the fluorometer are given in Figure 17. The curves indicate that the reading of the fluorometer in f.u. is linearly proportional to the concentration of Rhodamine WT dye to at least a concentration of 400 ppb. The highest dye concentration used in the dispersion tests of this investigation was about 300 ppb.

Photodecomposition of dye in low concentrations (less than 0.2%) by laboratory lighting (ultraviolet light) has been reported to be significant (perhaps as much as 20%) in a year. However, it has also been reported that dye samples stored in the dark for six months showed no change (Turner

Fig. 17. Linearity between Rhodamine WT fluorescent dye concentration and the fluorescence dial reading on all scales of the Turner Model 111 fluorometer.

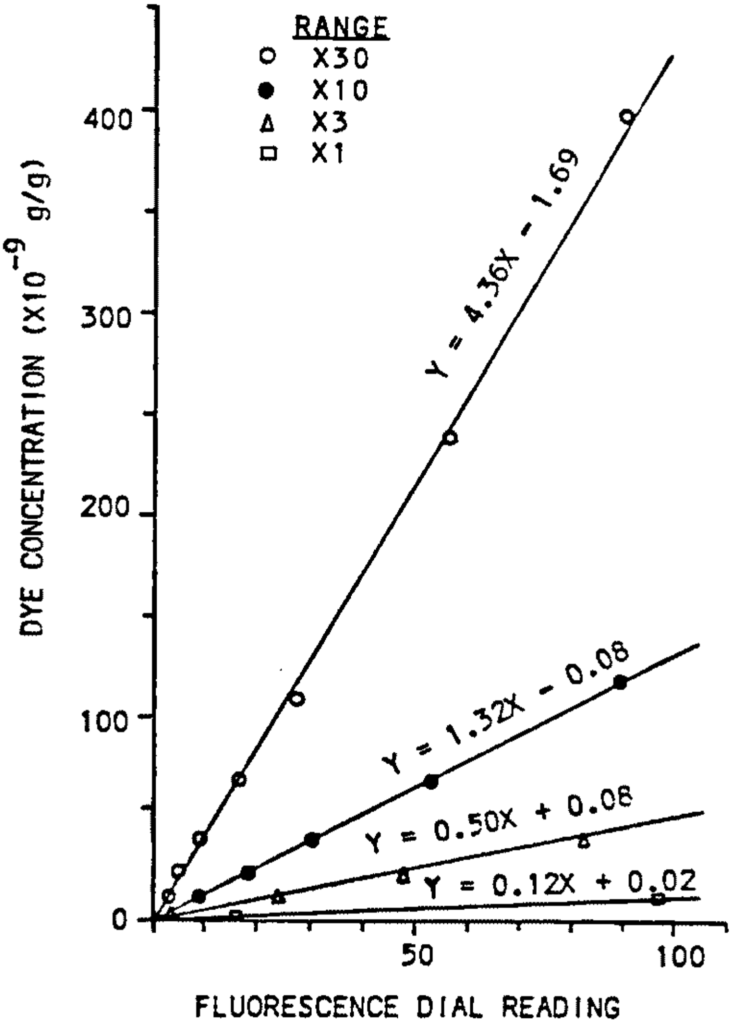
RANGE
○ X30
● X10
Δ X3
□ X1
Y = 4.36X - 1.69
Y = 1.32X - 0.08
Y = 0.50X + 0.08
Y = 0.12X + 0.02
DYE CONCENTRATION (X10^{-9} g/g)
0
100
200
300
400
50
100
FLUORESCENCE DIAL READING

Designs 1982). Undocumented reports indicate that chemical degradation by chlorine in its elemental form results in a rapid destruction of the fluorescence of the dye (Turner Designs 1982). However, elemental chlorine exists only transiently in solution. It rapidly dismutates and the dismutated form is commonly called "residual" chlorine. Deaner (1973) demonstrated that levels of residual chlorine, considerably in excess of those found in tap water, have no effect on the fluorescence of Rhodamine WT dye. The fluorescence of Rhodamine WT dye is also affected by temperature, as the dye concentration is inversely proportional to the temperature (Turner Designs 1982).

To minimize the effects of photodecomposition, chemical degradation, and temperature on Rhodamine WT dye concentrations, all standards and water samples analyzed in this investigation were stored in the dark and analyzed at fairly uniform ambient temperatures, ranging from 22.8 to 24.5° C. The tap water in the flume and that used for diluting the manufacturer's dye solution in making standards was aged (stood for at least 24 hours in the open) to allow dismutation of elemental chlorine. Dye standards were checked before the sample analyses of each dispersion test. The dye concentration standards showed no appreciable change over a 3 month period.

Experimental Procedures

The initial phase of the experimental investigation involved the preliminary set up of a tidal Froude model and its laboratory prototype, and validation of model and prototype tide heights and current velocities through the process of verification and prototype calibration. The preliminary set up of the model or prototype (see Table 1) began by adjusting the model or prototype to the required length by inserting a barrier across the channel. The flume was then filled with tap water in conjunction with the adjustment of the tide generator to attain the required static mean depth (3.80 cm in the model and 5.52 cm in the prototype), and required static tidal range (0.95 cm in the model and 1.38 cm in the prototype). Static high, low, and mean water levels were measured at the channel entrance with a point gage graduated in 0.1 mm increments. The required tidal period was set by adjustment of the output voltage of the tide generator's dc power supply while timing the movement of the tide generator with a stop watch graduated in seconds. To measure the longitudinal distribution of tracer in subsequent dye dispersion tests, thirteen water sampling probes were positioned along the centerline of the flume at the locations given in Table 4. The probes were positioned at mid-depth below static low water (1.67 cm above bottom in the

Table 4. Prototype and model station locations.

	Flume Stations*												
	F0	F1	F2	F3	F4	F5	F6	F7	F8	F9	F10	F11	F12
	Distance (x) from channel entrance - (cm)												
Prototype (x_p)	0	145	290	435	580	725	870	1016	1161	1306	1451	1596	1689
Model (x_m)	0	100	200	300	400	500	600	700	800	900	1000	1100	1164
$x_p/L_p = x_m/L_m$	0	0.085	0.170	0.255	0.340	0.426	0.511	0.596	0.681	0.766	0.851	0.936	0.991

*Dye concentrations were measured at all stations. Tide heights and current velocities were measured at stations F1, F5, and F9.

model and 2.42 cm above bottom in the prototype). Three water sampling probes were positioned at mid-depth along the centerline of the headbay. To eliminate standing wave disturbances created by the change in geometry between the channel and headbay, wave filters composed of synthetic packing fiber were placed at the channel entrance. A submersible pump and hose attachment were placed in the headbay to stir the dye-water mixture in subsequent dye dispersion tests. The pump was also activated during the model and prototype verification and calibration stage.

The model was set up first because the relative roughness of the channel was greater in the model than in the prototype. Roughness would eventually have to be added to the prototype channel in addition to the natural bed roughness already existing in the flume. Model tide heights and current velocities were measured for several tidal cycles using the capacitance wave height measuring system and electromagnetic current meter. The wave height probe and current velocity probe were positioned along the centerline of the channel at the locations given in Table 4. The current velocity probe was positioned at mid-depth below static low water.

Following set up of the model, the next step was to verify and calibrate the prototype against model observations of tide heights and current velocities. This procedure involved the preliminary set up of the prototype and the addition and adjustment of friction in the prototype channel until model tide heights and current velocities were reproduced throughout the length of the prototype channel. The degree of roughness afforded by the vertical placement of wire mesh screens in the channel cross section at various locations in the upper half of the prototype channel led to accurate simulation of prototype tide heights and current velocities (Figs. 18 and 19).

The flow regimes on the model and prototype were determined at various locations along the channel centerline by visual observation of potassium permanganate ($KMnO_4$) dye trails which emanated from $KMnO_4$ crystals suspended in the flow at mid-depth. The vertical placement of wire mesh screens in the channel cross section in the upper half of the prototype channel aided in inducing turbulence.

The final phase of the experimental investigation involved verification of longitudinal dye dispersion in the model and prototype. Longitudinal dispersion was examined by conducting constant-density dye dispersion tests in the model and in the prototype, similar to dye intrusion experiments conducted by Ippen (1966) but without freshwater discharge. Before the model or prototype headbay was dosed with dye, the water in the flume was aged for at least 24 hours to allow time for chlorine dissipation since chlorine is known to degrade Rhodamine WT dye. With the water level in the flume set to static low water, a temporary barrier was placed across the channel entrance to separate the channel and headbay. The headbay was dosed with about 10 drops of stock Rhodamine WT dye. The quantity of dye used was determined by experimenting with dye concentration ranges, based on the sensitivity of the fluorometer. To initially mix the dye and water in the headbay and to maintain a constant dye concentration in the headbay during the dispersion tests, an underwater diffuser consisting of a submersible pump (Little Giant Model 5-MSP) and garden hose attachment was set up and activated in the headbay. The hose was 1.8 m long and plugged at one end and contained numerous 64 mm diameter holes along its length. The pump was placed near the water surface at the far end of the headbay with the hose extending lengthwise along the bottom of the headbay. Initial mixing in the headbay was monitored by taking water samples at various locations in the headbay and reading the dye concentrations on the fluorometer. The dimensions of the headbay were such, that the dye-water mixture could be regarded as an infinite volume for both the model and the prototype. After mixing was complete, i.e. after the dye concentration in the headbay was constant throughout, the water sampling system was activated to take background samples in the channel.

With the channel waters quiescent at low water (LW 0), the barrier separating the channel and headbay was removed and the tide generator was started, simultaneously. Dye concentrations were simultaneously monitored in the headbay and along the length of the channel by collecting water samples at both high and low water slack every five tidal cycles for 30 tidal cycles. The selection of 30 tidal cycles was based on observations of the longitudinal extent of the plume in relation to the channel bend in the prototype, the dye plume rounded the channel bend after about 30 tidal cycles. Slack currents were determined by observing polystyrene surface floats near the mid-lengths of the model and prototype channels. The floats reversed their direction of travel near times of slack current. Upon completion of the model or prototype dispersion test, the dye-water samples were taken to the laboratory and stored overnight to allow time for temperature equilibration of the sample with room temperature. Dye concentrations were read on the fluorometer the following day.

Experimental Results

The laboratory investigation involved the set up of a Froude model and its prototype in a laboratory tidal flume of rectangular cross section. The model was operated according to the minimum Reynolds number criterion of 1400 at the entrance to the channel in the absence of depth distortion and density differences. The intrusion of tracer-dye from the model and prototype headbays was monitored at high and low water slack every five tidal cycles for 30 tidal cycles. The match between model and prototype spatial and temporal longitudinal dye distributions was taken as a measure of the model's ability to reproduce the dispersive mechanisms existing in the prototype under the imposed conditions. The values of the parameters used in setting up the laboratory prototype and its tidal Froude model are given in Table 1.

Graphical comparisons of model and prototype tide height profiles at stations F1, F5, and F9 are shown in Figure 18. (In Figure 18, model values have been converted to corresponding prototype values.) Tide height profiles show consistent agreement between model and prototype tidal ranges, durations of flood, and durations of ebb. Tide heights in the model appear to be approximately in phase with those of the prototype. As expected for a cooscillating tide (standing wave), the maximum amplitude of the tide oc-

Fig. 18. Prototype and model tide height comparisons at stations F1, F5 and F9.

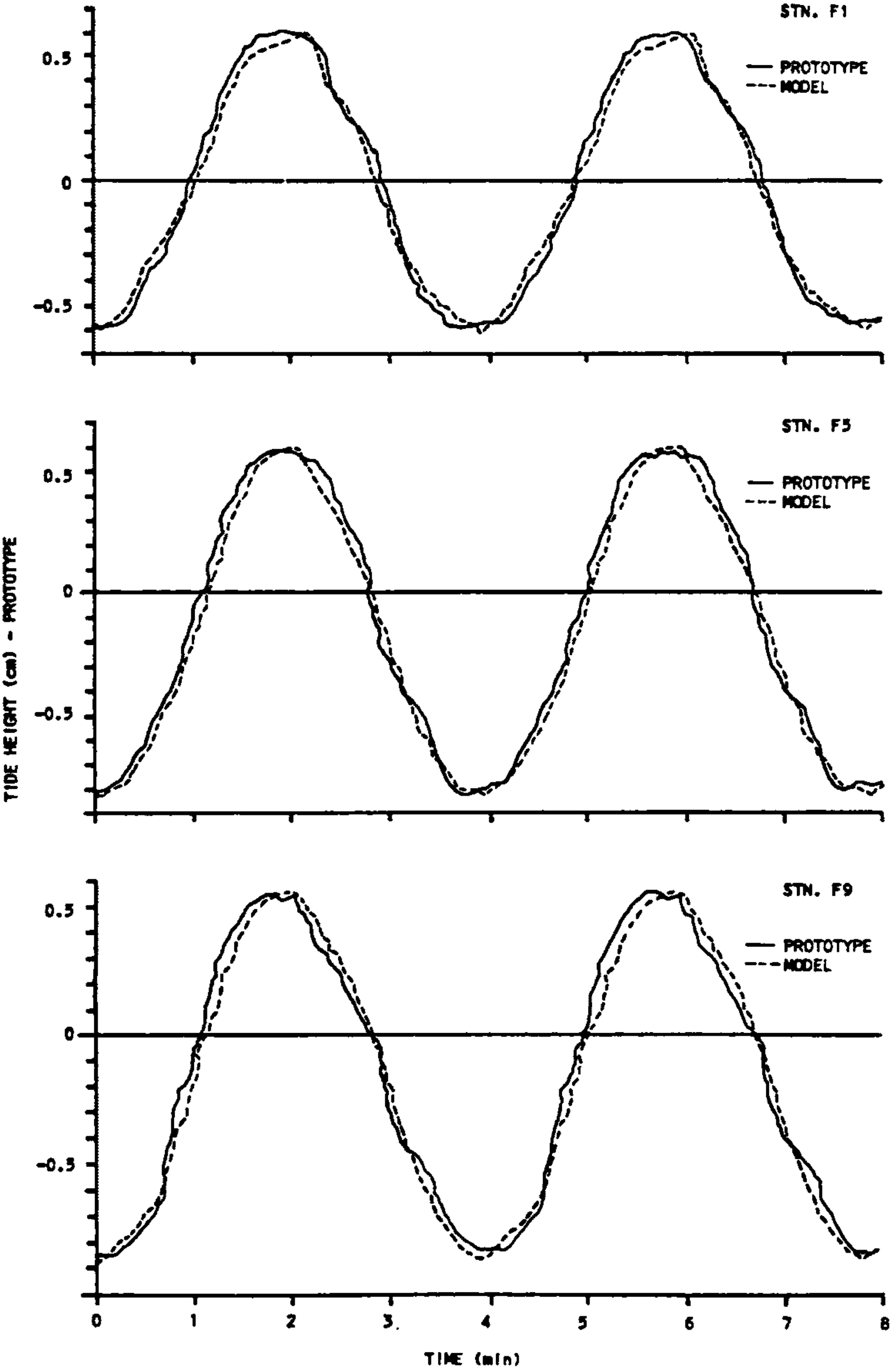
STN. F1
PROTOTYPE
MODEL
STN. F5
PROTOTYPE
MODEL
STN. F9
PROTOTYPE
MODEL
0.5
0
-0.5
TIDE HEIGHT (cm) - PROTOTYPE
0
1
2
3
4
5
6
7
8
TIME (min)

curred at the closed end of the flume (Ippen 1966).

Graphical comparisons of model and prototype current velocity profiles at stations F1, F5, and F9 are shown in Figure 19. (In Figure 19, model values have been converted to corresponding prototype values.) A reasonable match between model and prototype current velocities, durations of flood, and durations of ebb was possible. Current velocities in the model appear to be approximately in phase with those of the prototype. As expected for a cooscillating tide, the maximum current velocity occurred at the channel entrance (Ippen 1966).

Although the validation of tide heights and current velocities in estuary model studies is rather subjective, Harleman (1971) presents rough guidelines as to the degree to which typical model verifications of current velocities may range. Current velocity profiles validated for the Delaware Estuary model (horizontal scale 1:1000 and vertical scale 1:100) are used as examples of "better" and "poorer" verifications. Station 15-F is cited as representative of "better" verifications, where the percent difference in maximum current velocities is about 40% at worst and about 18% on the average. Station 4-B is cited as representative of "poorer" verifications, where the percent difference in maximum velocity is about 57% at worst and about 22% on the average. For the model in this investigation, the percent difference in maximum current velocities was about 14% at worst and about 8% on the average.

Fig. 19. Prototype and model current velocity comparisons at stations F1, F5 and F9.

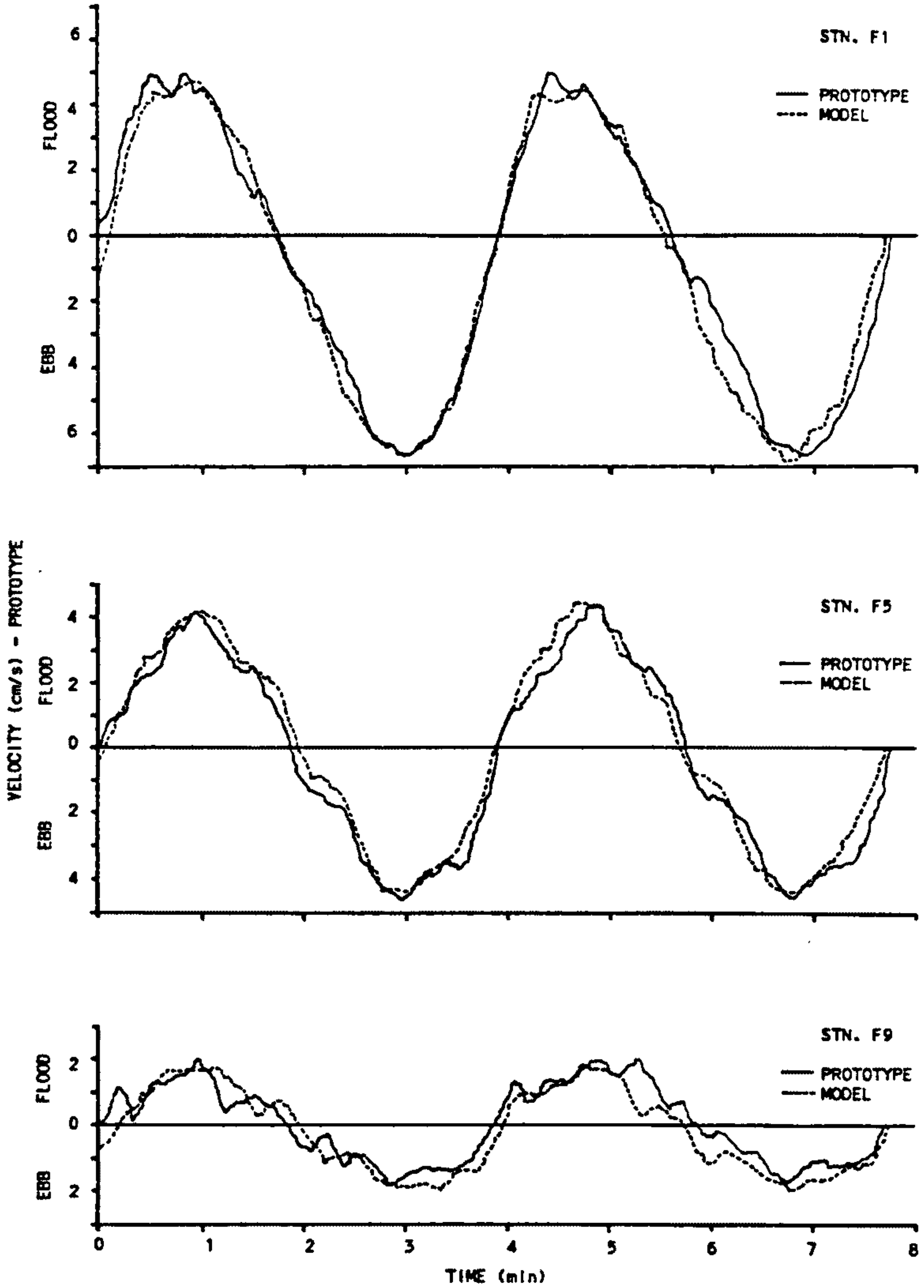
STN. F1
PROTOTYPE
MODEL
FLOOD
EBB
6
4
2
0
2
4
6
STN. F5
PROTOTYPE
MODEL
VELOCITY (cm/s) - PROTOTYPE
FLOOD
EBB
4
2
0
2
4
STN. F9
PROTOTYPE
MODEL
FLOOD
EBB
2
0
2
0
1
2
3
4
5
6
7
8
TIME (min)

Observation of the model flow regime indicated that turbulence persisted near the mouth (lower, two meters of the channel) throughout most of the tidal cycle. Turbulence was found to decay rapidly at times of slack current in the upper two-thirds of the channel, and turbulence did not resume until the flood or ebb current had been running for some time. Near the closed end of the channel, the flow was mostly laminar. In the lower two-thirds of the prototype channel, the flow was predominantly in the turbulent regime. Turbulence was found to decay near times of slack current near the closed end of the prototype channel. The wave filter at the channel entrance aided in inducing turbulence in the lower halves of the model and prototype channels. Wire mesh screens were placed vertically in the cross section of the prototype channel to promote turbulence in the upper portion of the channel. The absence of turbulent flow during portions of the tidal cycle in the model was anticipated, however, it was an undesirable feature in the prototype and was not anticipated when the dimensions of the flume were selected.

The results of the model and prototype dye dispersion tests are presented in plots (Figs. 20, 21 and 22) which compare spatial and temporal longitudinal dye distributions at all monitored high and low water slack currents. Fluorescence dial readings of the fluorometer were converted to dye concentrations by mass in accordance with laboratory calibrations of dye standards, given for the model and prototype

Fig. 20a. Prototype and model spatial dye distribution comparison at HW 5.

Fig. 20b. Prototype and model spatial dye distribution comparison at HW 10.

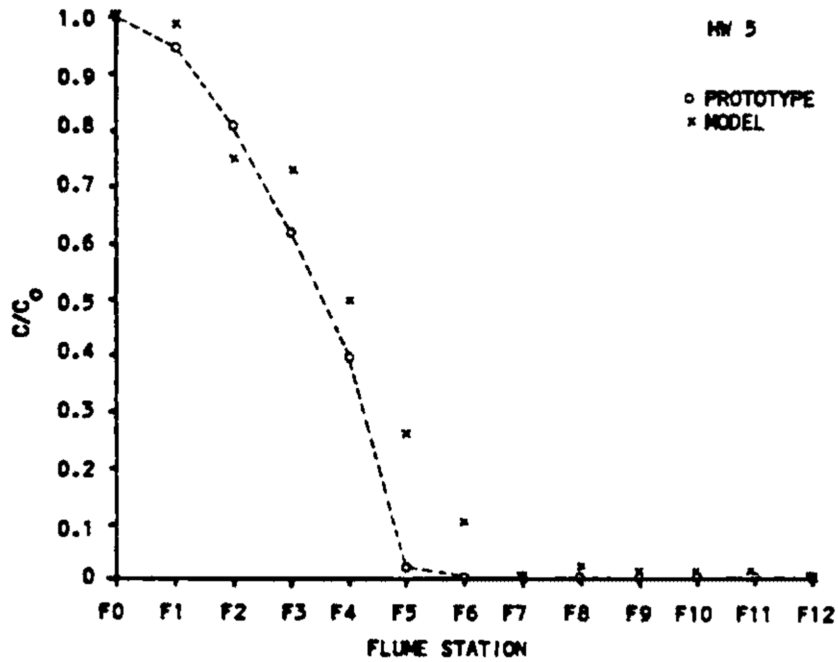
1.0
0.9
0.8
0.7
0.6
0.5
0.4
0.3
0.2
0.1
0
C/C_o
HW 5
○ PROTOTYPE
× MODEL
F0
F1
F2
F3
F4
F5
F6
F7
F8
F9
F10
F11
F12
FLUME STATION

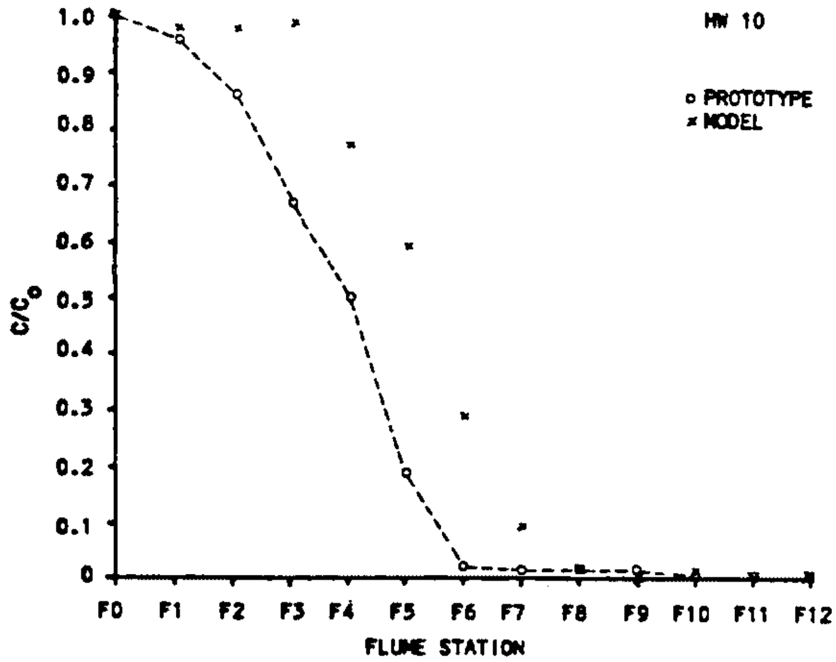
1.0
0.9
0.8
0.7
0.6
0.5
0.4
0.3
0.2
0.1
0
C/C_o
HW 10
○ PROTOTYPE
× MODEL
F0
F1
F2
F3
F4
F5
F6
F7
F8
F9
F10
F11
F12
FLUME STATION

Fig. 20c. Prototype and model spatial dye distribution comparison at HW 15.

Fig. 20d. Prototype and model spatial dye distribution comparison at HW 20.

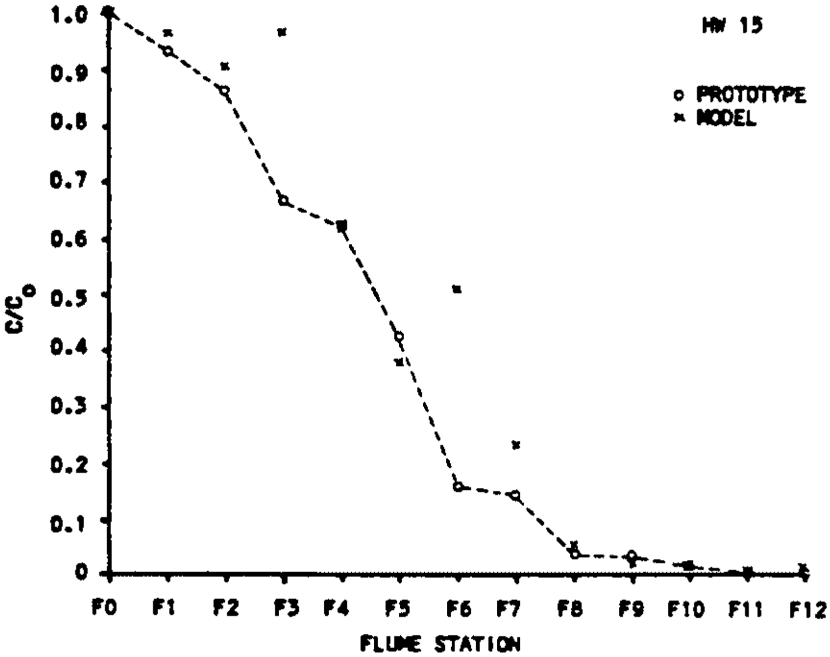
HW 15
PROTOTYPE
MODEL
C/C$_o$
1.0
0.9
0.8
0.7
0.6
0.5
0.4
0.3
0.2
0.1
0
F0
F1
F2
F3
F4
F5
F6
F7
F8
F9
F10
F11
F12
FLUME STATION

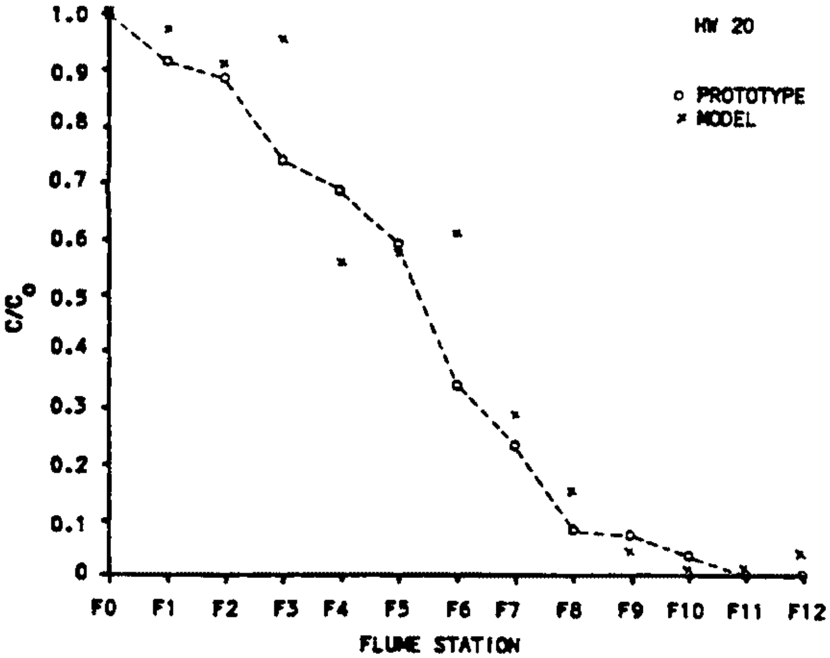
HW 20
PROTOTYPE
MODEL
C/C$_o$
1.0
0.9
0.8
0.7
0.6
0.5
0.4
0.3
0.2
0.1
0
F0
F1
F2
F3
F4
F5
F6
F7
F8
F9
F10
F11
F12
FLUME STATION

Fig. 20e. Prototype and model spatial dye distribution comparison at HW 25.

Fig. 20f. Prototype and model spatial dye distribution comparison at HW 30.

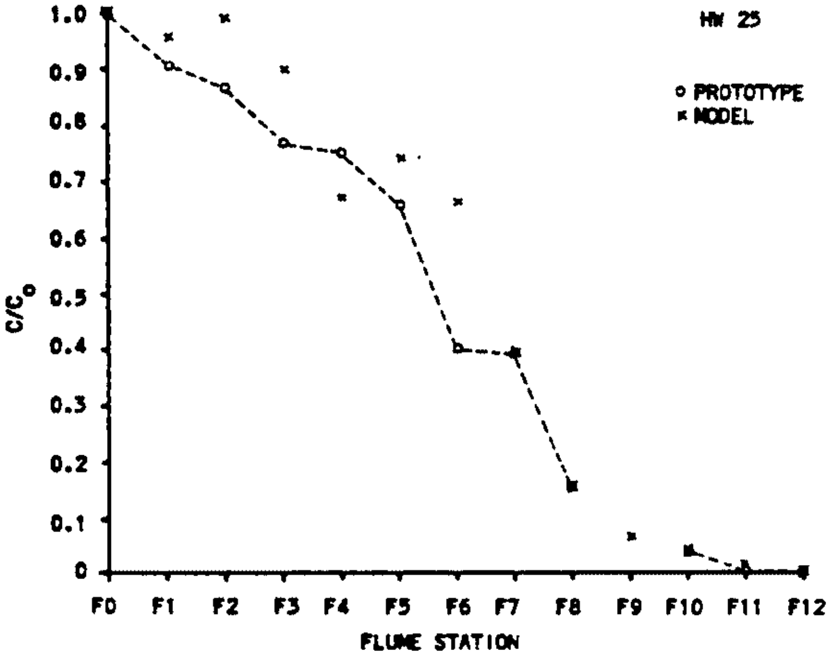
HW 25
○ PROTOTYPE
× MODEL
C/C$_o$
1.0
0.9
0.8
0.7
0.6
0.5
0.4
0.3
0.2
0.1
0
F0 F1 F2 F3 F4 F5 F6 F7 F8 F9 F10 F11 F12
FLUME STATION

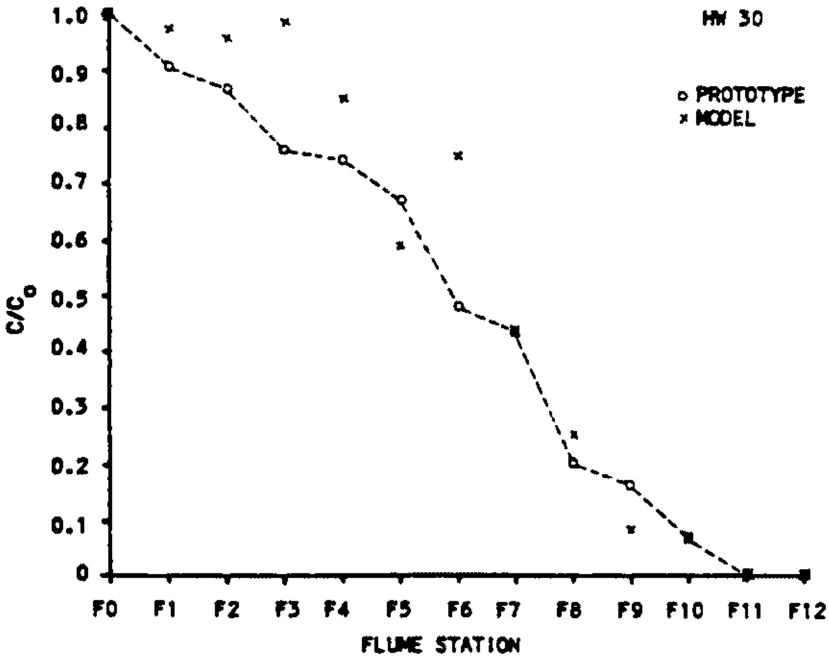
HW 30
○ PROTOTYPE
× MODEL
C/C$_o$
1.0
0.9
0.8
0.7
0.6
0.5
0.4
0.3
0.2
0.1
0
F0 F1 F2 F3 F4 F5 F6 F7 F8 F9 F10 F11 F12
FLUME STATION

Fig. 21a. Prototype and model spatial dye distribution comparison at LW 5.

Fig. 21b. Prototype and model spatial dye distribution comparison at LW 10.

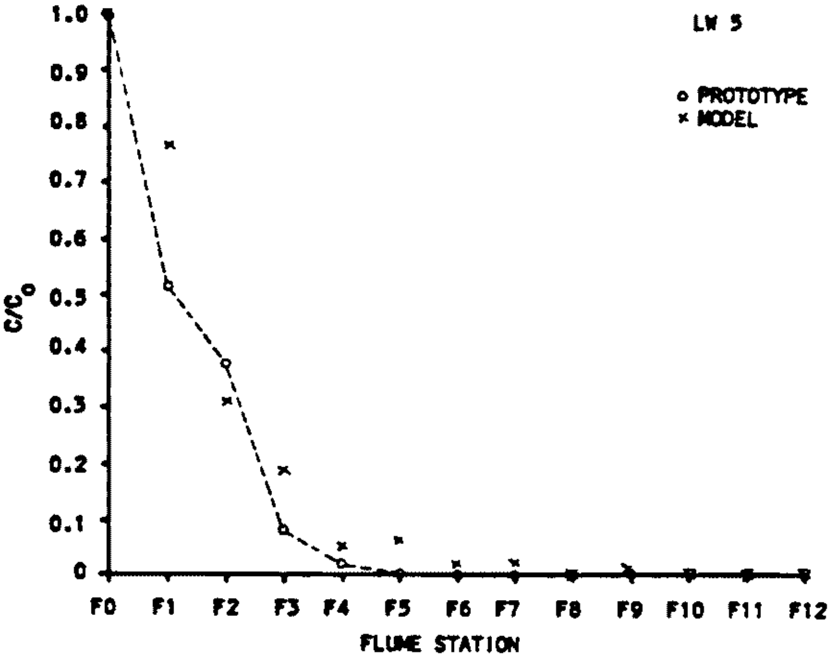
LW 5
o PROTOTYPE
× MODEL
C/C$_0$
1.0
0.9
0.8
0.7
0.6
0.5
0.4
0.3
0.2
0.1
0
F0
F1
F2
F3
F4
F5
F6
F7
F8
F9
F10
F11
F12
FLUME STATION

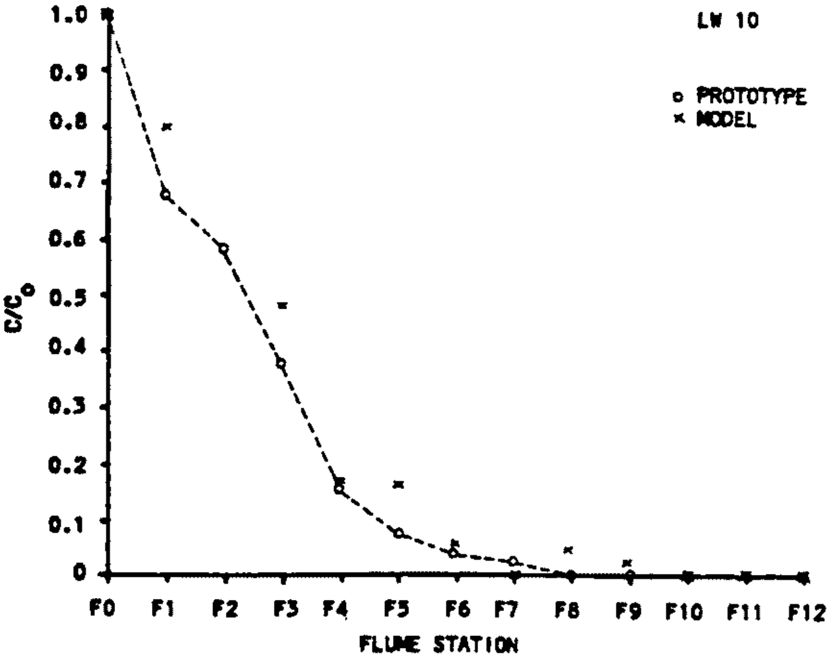
LW 10
o PROTOTYPE
× MODEL
C/C$_0$
1.0
0.9
0.8
0.7
0.6
0.5
0.4
0.3
0.2
0.1
0
F0
F1
F2
F3
F4
F5
F6
F7
F8
F9
F10
F11
F12
FLUME STATION

Fig. 21c. Prototype and model spatial dye distribution comparison at LW 15.

Fig. 21d. Prototype and model spatial dye distribution comparison at LW 20.

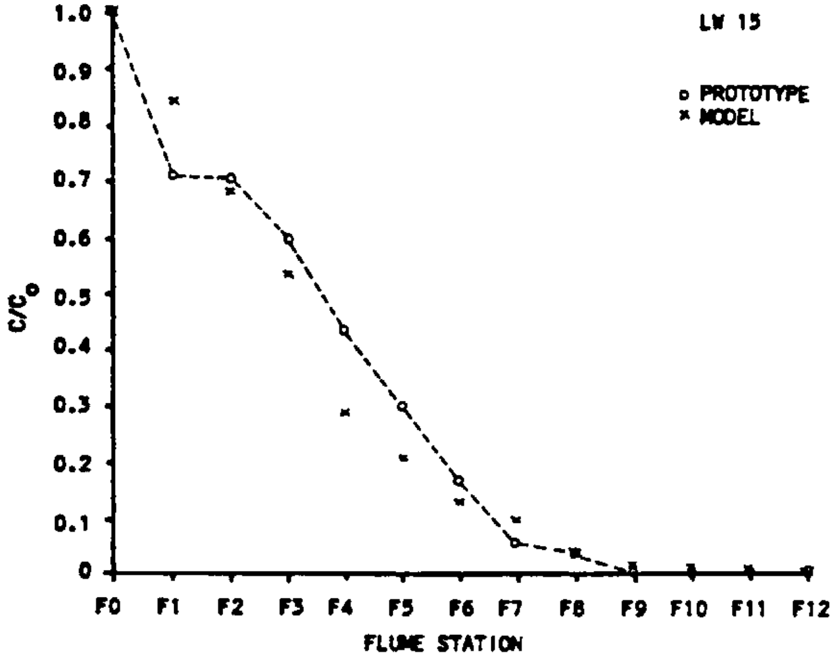
LW 15
o PROTOTYPE
× MODEL
C/C_o
1.0
0.9
0.8
0.7
0.6
0.5
0.4
0.3
0.2
0.1
0
F0
F1
F2
F3
F4
F5
F6
F7
F8
F9
F10
F11
F12
FLUME STATION

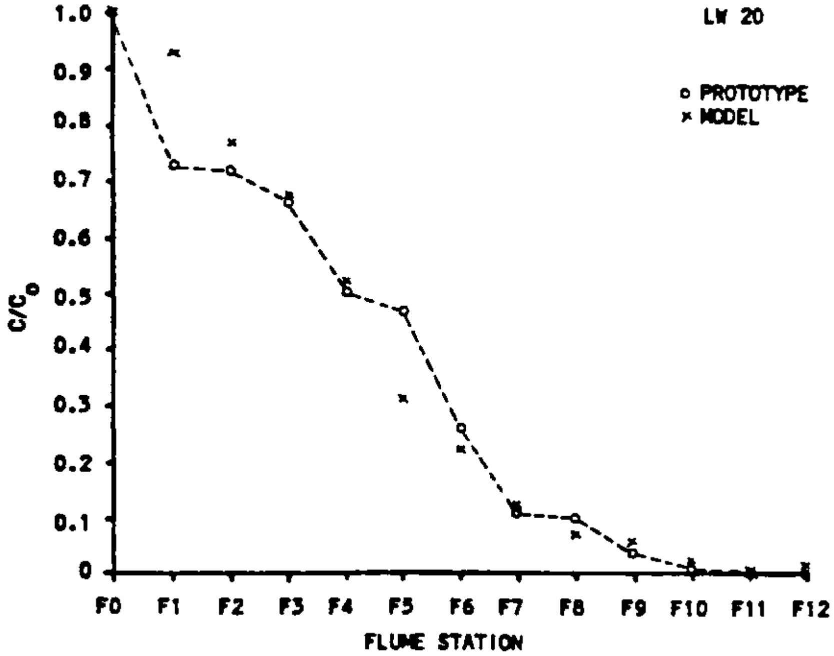
LW 20
o PROTOTYPE
× MODEL
C/C_o
1.0
0.9
0.8
0.7
0.6
0.5
0.4
0.3
0.2
0.1
0
F0
F1
F2
F3
F4
F5
F6
F7
F8
F9
F10
F11
F12
FLUME STATION

Fig. 21e. Prototype and model spatial dye distribution comparison at LW 25.

Fig. 21f. Prototype and model spatial dye distribution comparison at LW 30.

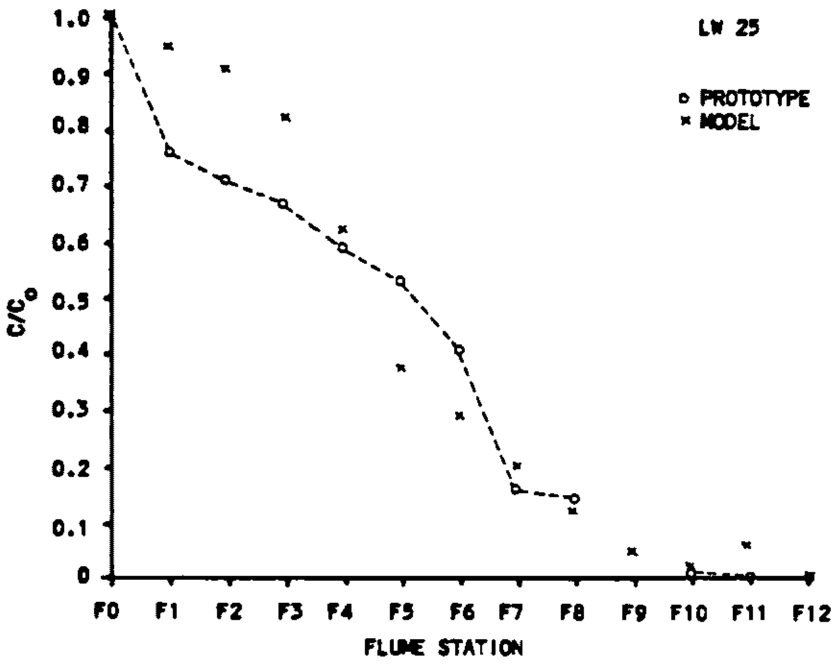
LW 25
PROTOTYPE
MODEL
C/C$_o$
1.0
0.9
0.8
0.7
0.6
0.5
0.4
0.3
0.2
0.1
0
F0
F1
F2
F3
F4
F5
F6
F7
F8
F9
F10
F11
F12
FLUME STATION

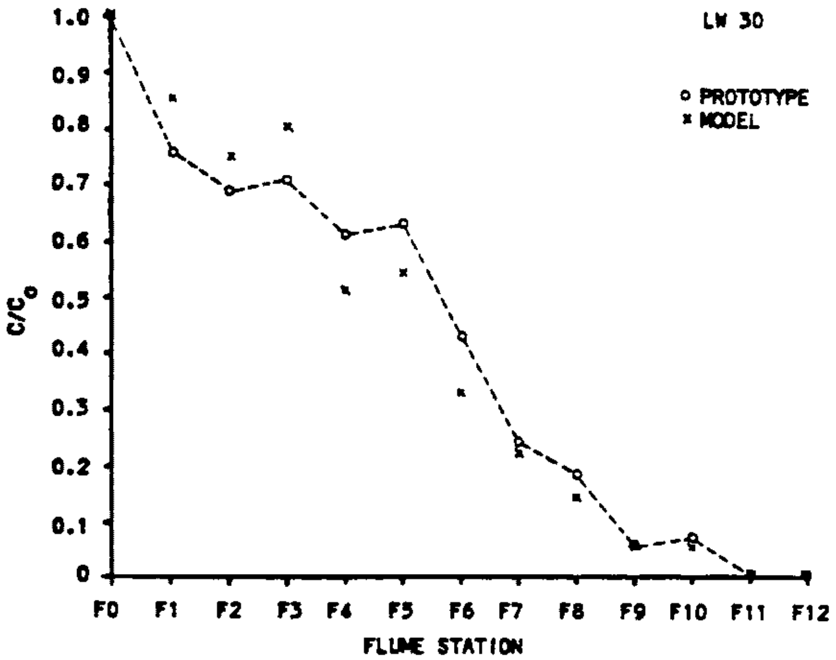
LW 30
PROTOTYPE
MODEL
C/C$_o$
1.0
0.9
0.8
0.7
0.6
0.5
0.4
0.3
0.2
0.1
0
F0
F1
F2
F3
F4
F5
F6
F7
F8
F9
F10
F11
F12
FLUME STATION

Fig. 22a. Prototype and model temporal dye distribution comparison at station F1.

Fig. 22b. Prototype and model temporal dye distribution comparison at station F2.

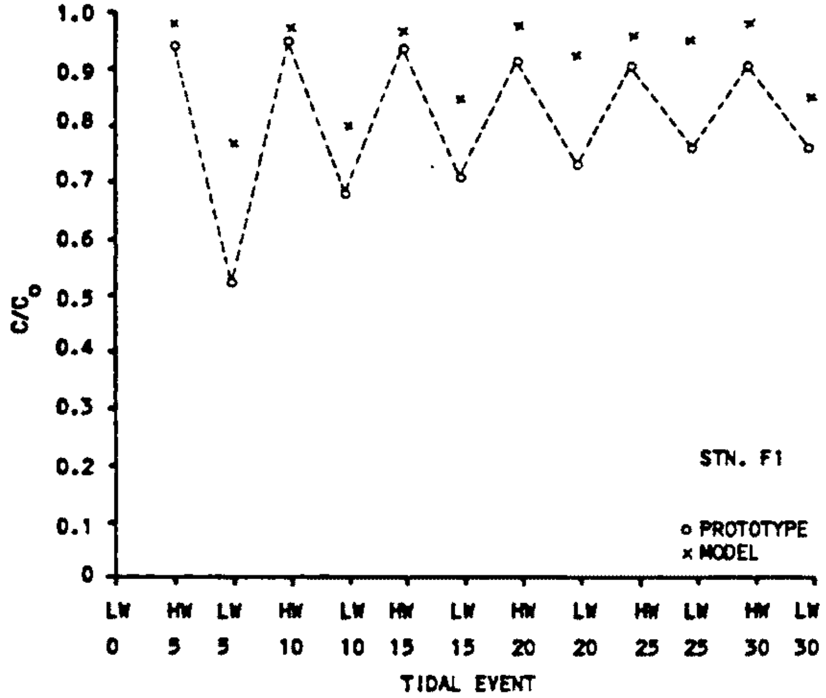
1.0
0.9
0.8
0.7
0.6
0.5
0.4
0.3
0.2
0.1
0
C/C$_o$
STN. F1
○ PROTOTYPE
× MODEL
LW 0
HW 5
LW 5
HW 10
LW 10
HW 15
LW 15
HW 20
LW 20
HW 25
LW 25
HW 30
LW 30
TIDAL EVENT

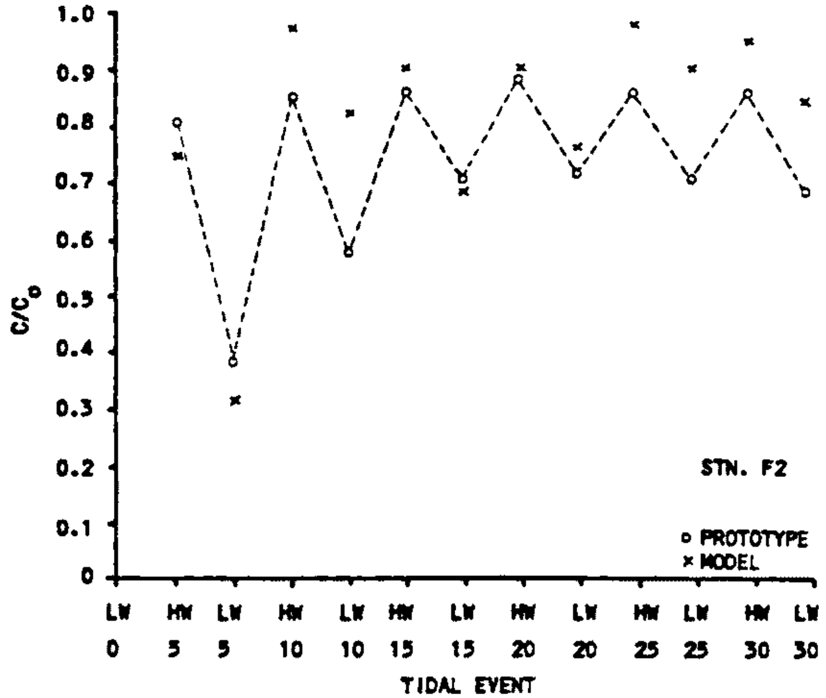
1.0
0.9
0.8
0.7
0.6
0.5
0.4
0.3
0.2
0.1
0
C/C$_o$
STN. F2
○ PROTOTYPE
× MODEL
LW 0
HW 5
LW 5
HW 10
LW 10
HW 15
LW 15
HW 20
LW 20
HW 25
LW 25
HW 30
LW 30
TIDAL EVENT

Fig. 22c. Prototype and model temporal dye distribution comparison at station F3.

Fig. 22d. Prototype and model temporal dye distribution comparison at station F4.

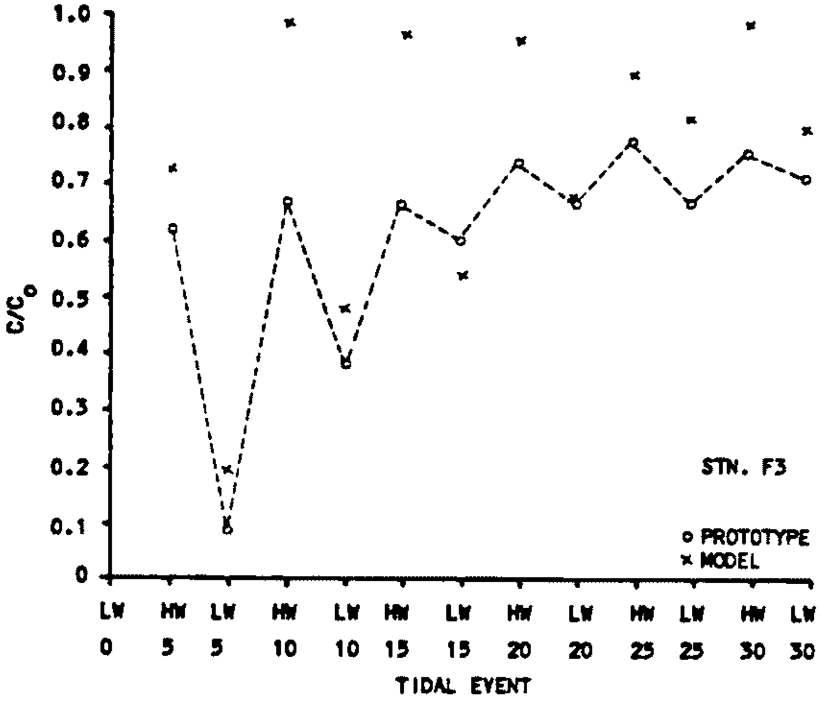
1.0
0.9
0.8
0.7
0.6
0.5
0.4
0.3
0.2
0.1
0
C/C$_o$
STN. F3
o PROTOTYPE
× MODEL
LW 0
HW 5
LW 5
HW 10
LW 10
HW 15
LW 15
HW 20
LW 20
HW 25
LW 25
HW 30
LW 30
TIDAL EVENT

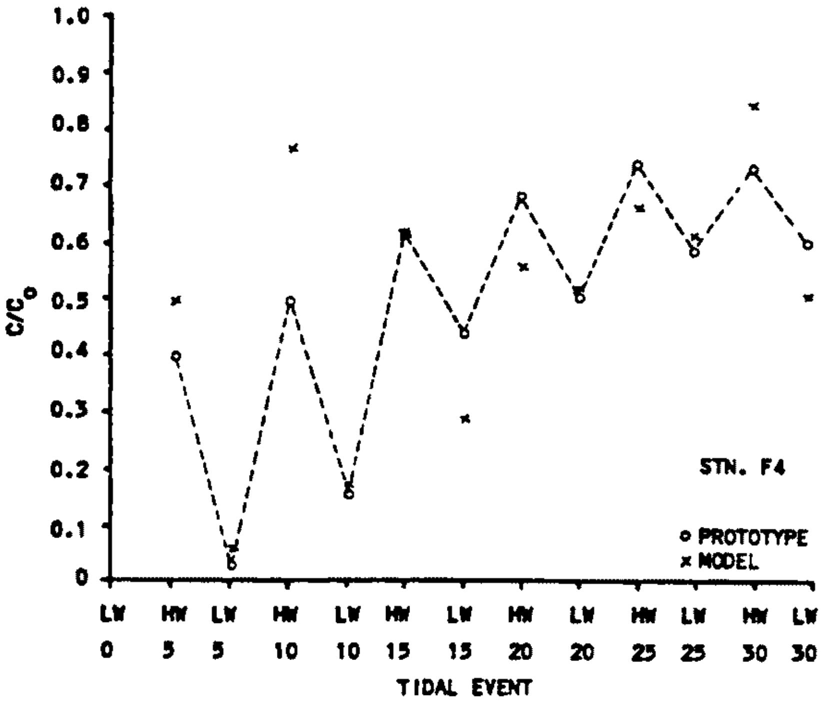
1.0
0.9
0.8
0.7
0.6
0.5
0.4
0.3
0.2
0.1
0
C/C$_o$
STN. F4
o PROTOTYPE
× MODEL
LW 0
HW 5
LW 5
HW 10
LW 10
HW 15
LW 15
HW 20
LW 20
HW 25
LW 25
HW 30
LW 30
TIDAL EVENT

Fig. 22e. Prototype and model temporal dye distribution comparison at station F5.

Fig. 22f. Prototype and model temporal dye distribution comparison at station F6.

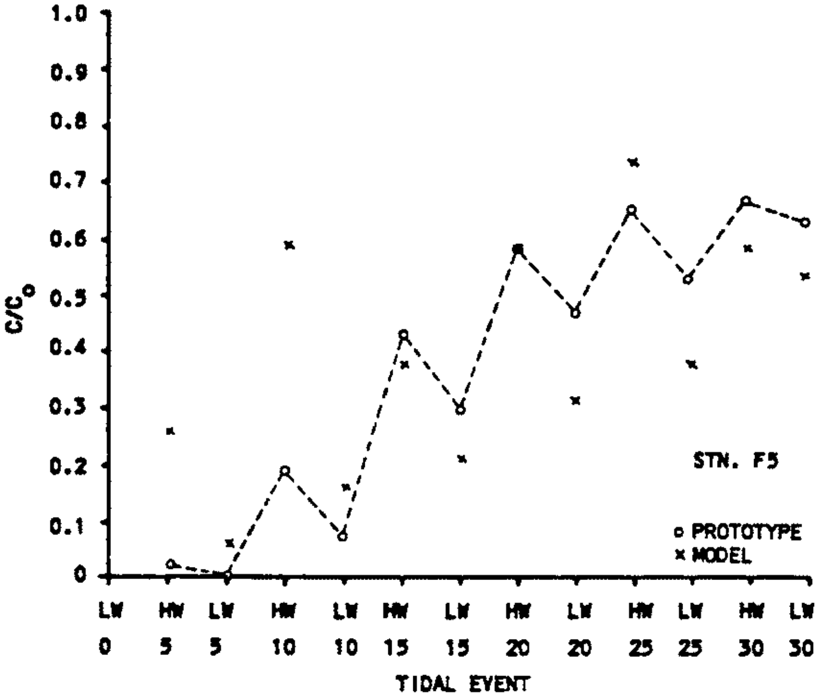
C/C$_o$
1.0
0.9
0.8
0.7
0.6
0.5
0.4
0.3
0.2
0.1
0
STN. F5
○ PROTOTYPE
× MODEL
LW 0
HW 5
LW 5
HW 10
LW 10
HW 15
LW 15
HW 20
LW 20
HW 25
LW 25
HW 30
LW 30
TIDAL EVENT

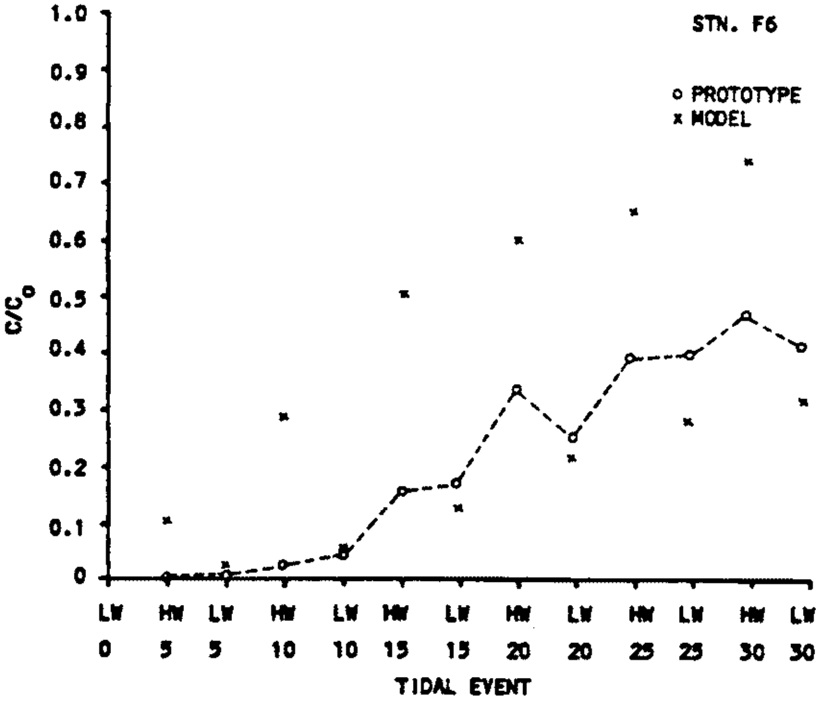
C/C$_o$
1.0
0.9
0.8
0.7
0.6
0.5
0.4
0.3
0.2
0.1
0
STN. F6
○ PROTOTYPE
× MODEL
LW 0
HW 5
LW 5
HW 10
LW 10
HW 15
LW 15
HW 20
LW 20
HW 25
LW 25
HW 30
LW 30
TIDAL EVENT

Fig. 22g. Prototype and model temporal dye distribution comparison at station F7.

Fig. 22h. Prototype and model temporal dye distribution comparison at station F8.

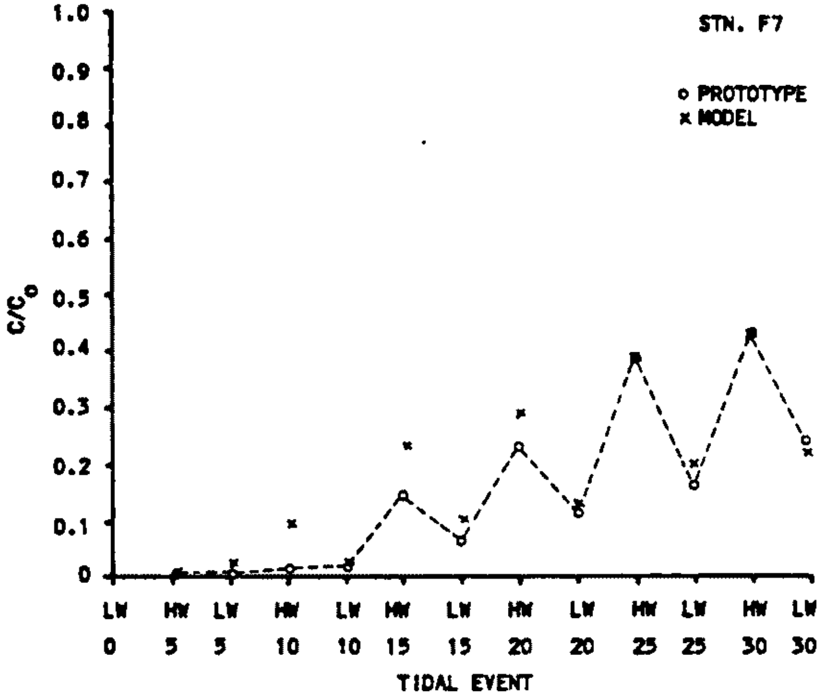
STN. F7
o PROTOTYPE
x MODEL
C/C$_o$
1.0
0.9
0.8
0.7
0.6
0.5
0.4
0.3
0.2
0.1
0
LW 0
HW 5
LW 5
HW 10
LW 10
HW 15
LW 15
HW 20
LW 20
HW 25
LW 25
HW 30
LW 30
TIDAL EVENT

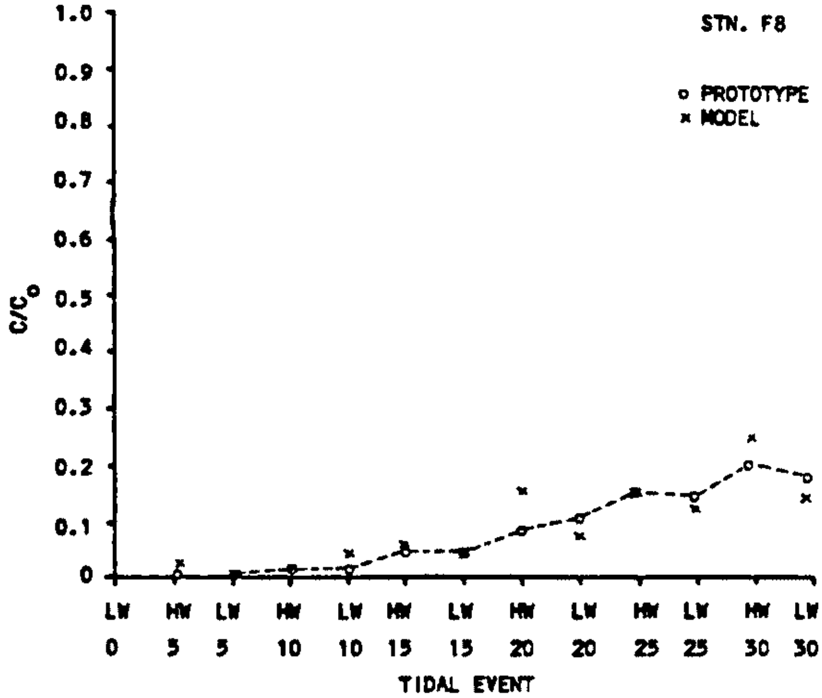
STN. F8
o PROTOTYPE
x MODEL
C/C$_o$
1.0
0.9
0.8
0.7
0.6
0.5
0.4
0.3
0.2
0.1
0
LW 0
HW 5
LW 5
HW 10
LW 10
HW 15
LW 15
HW 20
LW 20
HW 25
LW 25
HW 30
LW 30
TIDAL EVENT

in Tables 5 and 6. Background corrections were made by subtracting the average of the background concentrations (at LW 0) for all stations from the measured dye mass concentrations. All dye concentrations c were nondimensionalized c/c_0 against the average dye concentration in the headbay c_0. Since the volumes of water in the model and prototype headbays were much larger than their tidal prisms, the dye concentrations in the headbays and thus at the entrance of the flume remained fairly constant for the duration of the model and prototype dispersion tests. The average dye concentrations in the headbay during the tests was 264 ±10 ppb for the prototype and 276 ±23 ppb for the model. The amount of water removed from the flume during water sampling over 30 tidal cycles was equivalent to a change in the water levels of about 0.38 mm in the prototype and about 0.50 mm in the model.

Table 5. Actual dye mass concentration in the prototype.

	Sampling Stations															
	H3	H2	H1	F0	F1	F2	F3	F4	F5	F6	F7	F8	F9	F10	F11	F12
Event	c_{dye} (x 10^{-9} g/g) or ppb															
LW 00	282	280	279	282	0	0	0	0	0	0	0	0	0	0	0	0
HW 05	266	269	268	253	251	214	164	106	5	0	0	0	0	0	0	0
LW 05	276	272	248	271	137	100	21	5	1	0	0	0	0	0	0	0
HW 10	270	280	271	279	253	227	177	132	50	5	3	3	3	1	0	0
LW 10	277	279	263	268	180	153	100	42	18	11	3	3	1	0	0	0
HW 15	275	275	272	268	248	230	177	164	114	42	37	11	8	3	0	0
LW 15	268	264	259	262	187	187	158	116	79	45	16	11	3	0	0	0
HW 20	265	256	260	256	243	235	195	182	156	90	61	21	18	8	0	0
LW 20	260	260	251	255	193	190	177	135	124	69	29	26	13	2	0	0
HW 25	264	255	256	259	240	230	203	198	174	106	103	40	N.D.	13	0	0
LW 25	258	256	251	256	201	187	177	156	140	108	42	37	N.D.	3	0	0
HW 30	257	255	255	256	240	230	201	195	177	127	114	53	42	18	0	0
LW 30	253	262	248	252	201	182	187	161	166	114	63	48	13	16	0	0

N.D., Not determined.

Table 6. Actual dye mass concentration in the model.

	Sampling Stations															
	H3	H2	H1	F0	F1	F2	F3	F4	F5	F6	F7	F8	F9	F10	F11	F12
Event	c_{dye} (x 10^{-9} g/g) or ppb															
LW 00	300	294	305	297	1	0	0	0	1	0	1	1	1	0	0	1
HW 05	294	305	294	251	273	207	201	138	72	28	0	6	3	3	3	0
LW 05	297	285	303	294	213	86	52	14	17	6	6	0	3	0	3	0
HW 10	303	283	308	263	270	270	273	213	163	80	25	3	0	3	0	0
LW 10	285	288	297	260	221	224	132	47	44	14	6	11	6	0	0	0
HW 15	283	260	294	254	268	251	268	171	105	141	63	14	6	3	0	3
LW 15	294	283	197	225	235	190	149	80	58	36	28	11	6	3	3	0
HW 20	271	260	251	245	270	251	265	155	160	168	80	41	11	3	3	11
LW 20	260	280	283	277	257	213	188	144	86	61	33	19	11	6	0	3
HW 25	265	271	263	263	265	273	248	185	204	182	108	41	17	8	3	0
LW 25	277	285	297	225	262	251	226	171	105	80	55	33	14	6	17	0
HW 30	294	291	283	263	270	265	273	235	163	207	119	69	22	19	0	0
LW 30	280	257	248	271	235	207	221	141	149	91	61	39	14	14	0	0

Chapter 3

DISCUSSION

As discussed in chapter 1, the motivation for building many of our existing estuary models has been problems associated with navigation improvements. The achievement of Froude similitude of cross-sectional mean tidal motion in these models has been sufficient for solving navigation problems even though the flow regime on these models may be quite different from that in their prototypes. However, to avoid laminar viscous scale effects in the model and thus achieve exact Froude similitude, the same flow regime must be preserved on the model as in the prototype, i.e. turbulent and not laminar. Various modeling authorities have recommended Allen's (1947) minimum Reynolds number criterion of 1400 as being sufficient for the achievement of similitude of mean tidal motion in models used for solving navigation problems. Where the problem to be solved is extended to that of water quality and the modeling of longitudinal dispersion, the dispersive effects are primarily a function of flow regime and therefore may not be modeled properly in these models. In several, previous dispersion investigations in estuary models, similitude of dispersion has not been achieved throughout the reach under investigation. Whether the lack of similitude has been a result of the presence of laminar viscous scale effects has been unclear since other limitations to the achievement of similitude also exist, i.e. limitations imposed by depth distortion and exaggerated roughness elements. In this investigation all limitations to the achievement of dispersion similitude, other than possible laminar viscous scale effects, were eliminated by conducting dispersion tests in an undistorted, constant-density model.

The results of this investigation confirm previous findings that it is possible to achieve Froude similitude of cross-sectional mean tide heights and current velocities (see Figs. 18 and 19) even though the flow regime on the model may be quite different from that in the prototype. Allen's minimum Reynolds number criterion for tidal models did not guarantee turbulent flow throughout the tidal cycle, and thus, laminar viscous scale effects were present in the model. The flow in the model was laminar part of the time and turbulent part of the time with prolonged periods of laminar flow near times of slack current in contrast to the predominantly turbulent prototype. Consequently, comparisons between model and prototype spatial and temporal longitudinal dye distributions were generally poor (Figs. 20, 21, and 22).

In Figure 20, spatial dye distributions at high water slack HW show a better comparison in the early stages (HW 5) of the dispersion tests. A similar trend appears in Figure 21, showing spatial dye distributions at low water slack LW (LW 5, LW 10, and LW 15). During the early stages of the model dispersion test the dye cloud only sampled the flow regime in the lower portion of the channel, characterized by the highest velocities, highest Reynolds numbers, and therefore the most turbulence--similar to the predominantly turbulent flow regime in the prototype. Comparisons of model and prototype spatial dye distributions at HW 10 through HW 30 and LW 20 through LW 30 indicate that longitudinal dispersion, in general, was greatly distorted in the model. During the later stages of the model dispersion test the dye cloud sampled the flow regime in the upper portion of the channel, characterized by the lowest velocities, lowest Reynolds numbers, and prolonged periods of laminar flow--quite different from the flow regime in the prototype. The distortion of longitudinal dispersion at high water slack appears to have been more pronounced than at low water slack. This may have been a result of the occurrence of higher ebb velocities than flood velocities in the model, thereby producing higher Reynolds numbers and thus a flow regime similar to that of the prototype during the ebb. Figure 22 shows the distortion of longitudinal dispersion over time for stations F1 through F8.

Distortion of longitudinal dispersion is also apparent in the results of longitudinal dispersion experiments conducted in estuary models by Jugan (1982), Kuo et al. (1978), Blair (1980), and Blair (1976), however, the distortion of longitudinal dispersion in these experiments may also have been influenced by depth distortion and exaggerated roughness. Comparisons of model and prototype spatial dye distributions at low water slack for the ODU and WES Lafayette River models are shown in Figure 23 for an instantaneous dye release at a distance of 5 km (prototype) from the mouth and two tidal cycles after release. In the ODU model, longitudinal dispersion was particularly distorted in the two upper branches of the estuary (Fig. 23). (In Figure 23, the upper branches extend from 7 km from the mouth to 10 km from the mouth, and the top curve is the north branch and the bottom curve is the south branch.) This may have been caused by the presence of low advective velocities in the model reported by Blair (1976) and Kuo et al. (1978) and by the absence of roughness elements in these branches of the model which combine to inhibit turbulent flow. In the Lafayette River portion of the WES model, longitudinal dispersion was greatly distorted over most of the length of the estuary. A low Reynolds number of about 850 at the mouth appears to have been the likely cause of distortion, particularly in the main branch (Fig. 23). (In Figure 23, the main branch extends from the mouth to 7 km from the mouth.) Longitudinal dispersion in the two upper branches may also have been influenced by the effects of surface tension since the mean depth of these branches in the model was only about 1 cm. The distortion of longitudinal dispersion in the ODU and WES

Fig. 23. Lafayette River prototype, ODU model, and WES model spatial dye distribution comparisons at LW 3.

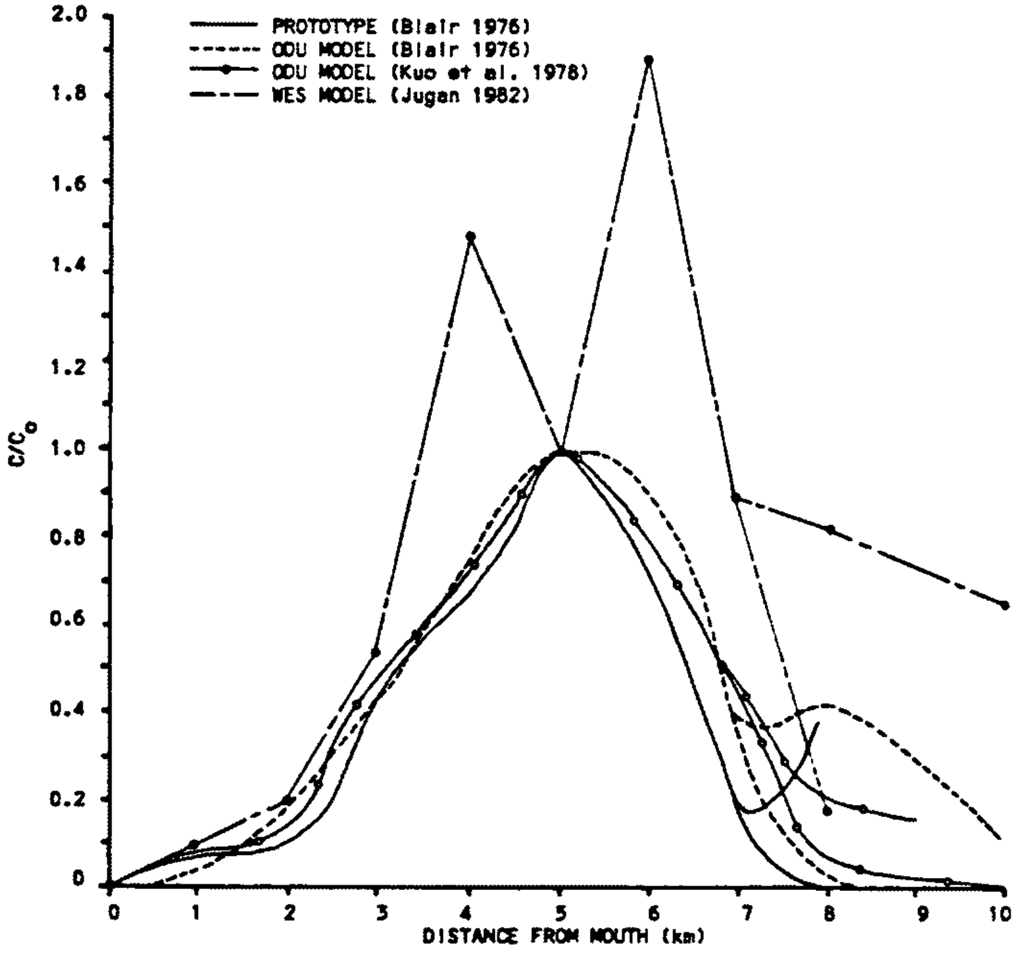
PROTOTYPE (Blair 1976)
ODU MODEL (Blair 1976)
ODU MODEL (Kuo et al. 1978)
WES MODEL (Jugan 1982)
2.0
1.8
1.6
1.4
1.2
1.0
0.8
0.6
0.4
0.2
0
C/C_o
0
1
2
3
4
5
6
7
8
9
10
DISTANCE FROM MOUTH (km)

models is also apparent in comparisons of model and prototype temporal dye distributions shown in Figure 24 for a station located at a distance of 5.5 km (prototype) from the mouth. It is suspected that the occurrence of greater distortion in the WES model than in the ODU model resulted because the Reynolds numbers in the ODU model were greater than those in the WES model. Table 7 gives the low water slack approximations of the longitudinal dispersion coefficient E_{LWS} reported by Blair (1976) and Kuo et al. (1978) for the ODU model and by Jugan (1982) for the WES model, showing that the longitudinal dispersion coefficients were magnified in the models.

Table 7. Low water slack dispersion coefficients for the ODU and WES Lafayette River models.

Model	Main Branch	North Branch	South Branch
	E_{LWS} (cm^2/s)		
ODU Model (required)	18.1	37.9	27.8
ODU (Blair 1976)	42.7	180.2	228.5
ODU (Kuo et al. 1978)	27.5	53.1	33.4
WES Model (required)	3.4	7.1	5.2
WES (Jugan 1982)	2.2-95.5	—	—

In general, prototype dye concentrations for the dispersion test conducted in the tidal flume for this investi-

Fig. 24. Lafayette River prototype, ODU model, and WES model temporal dye distribution comparisons at a distance of 5.5 km from the mouth.

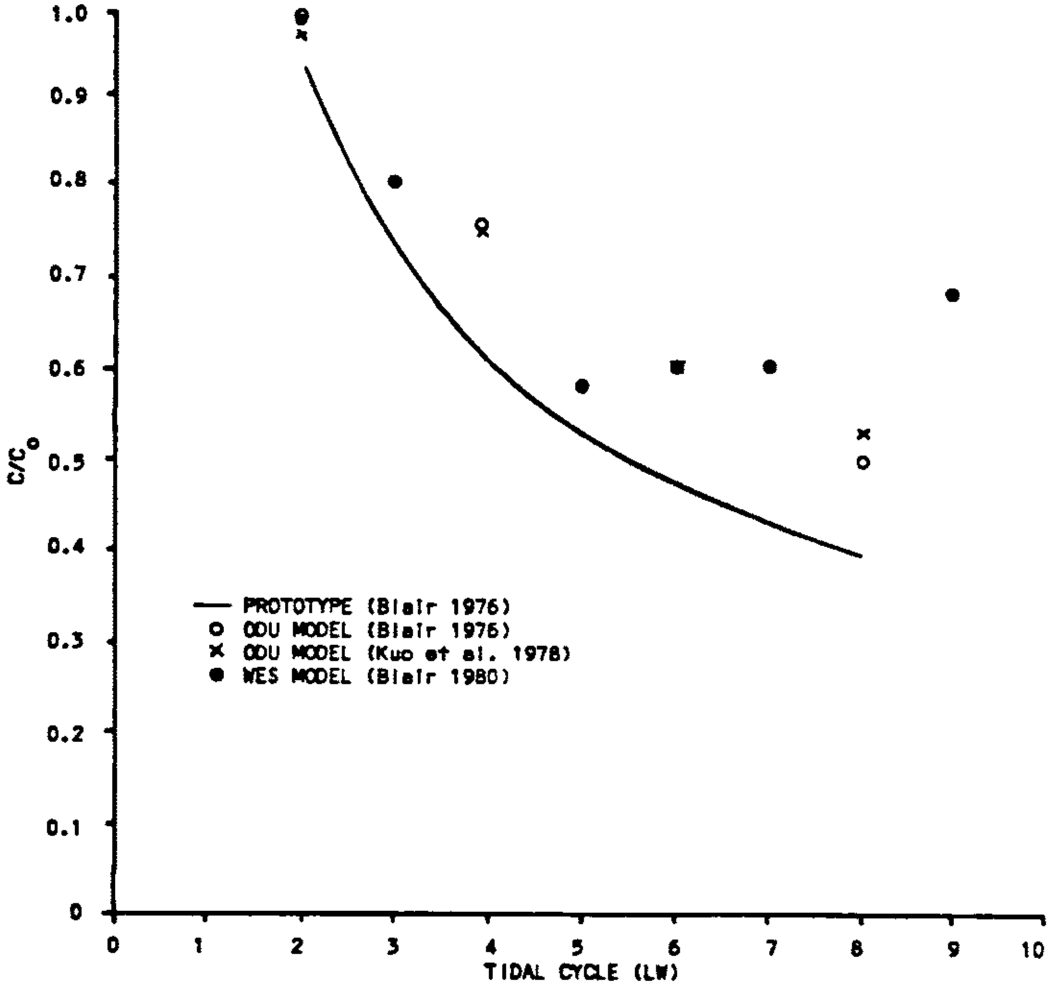
1.0
0.9
0.8
0.7
0.6
0.5
0.4
0.3
0.2
0.1
0
C/C_o
0
1
2
3
4
5
6
7
8
9
10
TIDAL CYCLE (LW)
PROTOTYPE (Blair 1976)
○ ODU MODEL (Blair 1976)
× ODU MODEL (Kuo et al. 1978)
● WES MODEL (Blair 1980)

gation and for dispersion tests conducted in the prototype Lafayette River by Blair (1976) were lower than those predicted by their respective models.

Further insight as to why longitudinal dispersion is magnified in tidal Froude models in which laminar flow exists during portions of the tidal cycle can be gained by exploring the mechanics of longitudinal dispersion.

A physical understanding of longitudinal dispersion can be gained by considering steady, uniform, two-dimensional open channel flow (Fischer 1973). Imagine that a line source of tracer-dye is injected instantaneously and uniformly across a flow moving in the x-direction (Fig. 25). The tracer will initially be advected downstream and take the shape of the velocity profile. Because of the shape of the profile, the tracer near the surface moves downstream much faster than the tracer near the bottom of the channel. The shearing action introduces vertical concentration gradients which are diminished by vertical mixing due to molecular diffusion in laminar flow and due primarily to turbulent diffusion in turbulent flow. In addition, there will be a large longitudinal spreading due to the velocity shear resulting from the differences in velocity with depth. During this initial (convective) period, the motion of the cloud of tracer is controlled primarily by the distribution of convective velocities over depth, and a skewed longitudinal concentration distribution is produced. The initial period is defined as the length of time which lapses before the

Fig. 25. The production of a Gaussian longitudinal concentration distribution by shear flow dispersion of a line source in an open channel. (a) The line source. (b) The velocity profile. (c) The initial convection of the line source. (d) The mean concentration distribution for the cloud shown in (c). (e) The cloud at the end of the initial period. (f) The mean concentration distribution for the cloud shown in (e). (g) The cloud sometime after the initial period. (h) Gaussian concentration distribution for the cloud shown in (g).

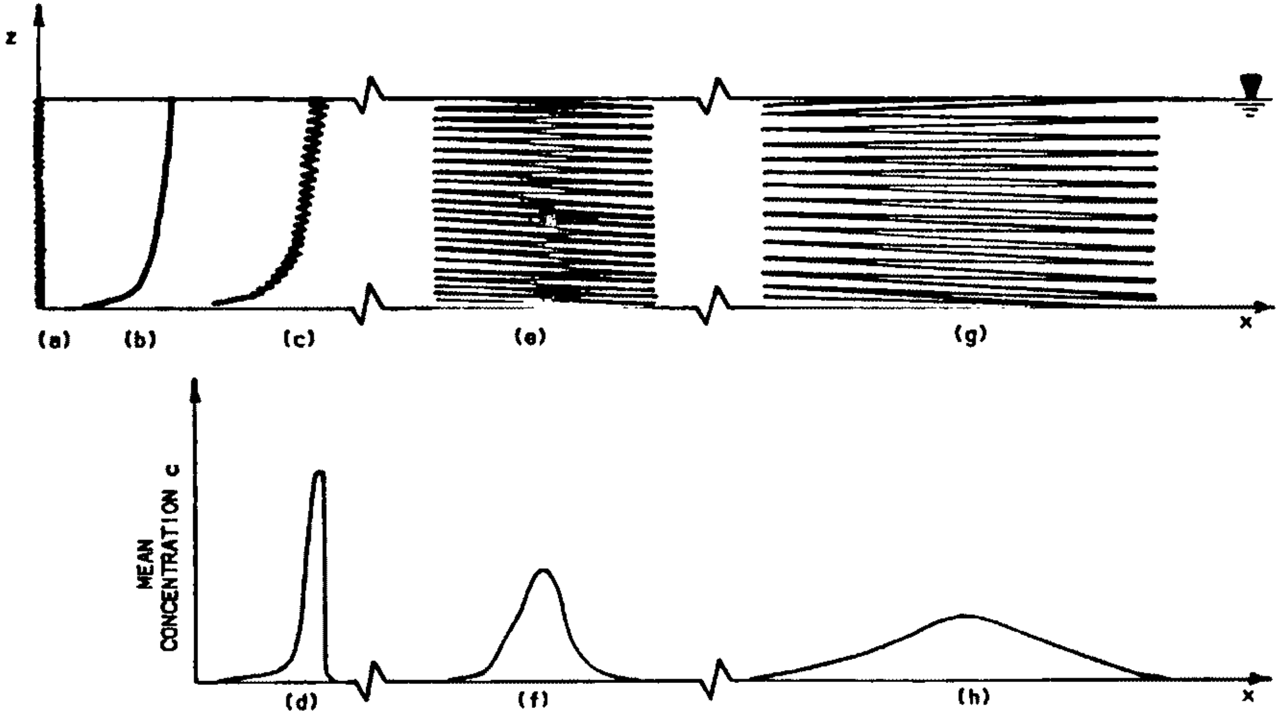
z
(a)
(b)
(c)
(e)
(g)
x
MEAN CONCENTRATION c
(d)
(f)
(h)
x

variance of the distribution becomes linear with time. After the initial period, the longitudinal spread of the tracer by the velocity profile will balance the vertical spread of the tracer by diffusion. At this time the concentration across every cross section will be nearly uniform and the longitudinal distribution of the cross-sectional mean concentration will become approximately Gaussian. As the cloud of tracer continues to be advected downstream, longitudinal dispersion will tend to erase longitudinal concentration gradients, as the concentration distribution curve gradually flattens over time.

The longitudinal dispersion of a tracer-dye due to shear flow as previously described, is subject to the findings of Taylor (1954 and 1953), describing first laminar and then turbulent shear flow dispersion (Fischer 1973). Taylor seems to have been the first to identify the essential role of the velocity distribution and the opposing action of cross-sectional diffusion to longitudinal dispersion. The differential equation describing the movement of a conservative tracer in laminar or turbulent shear flow of constant density in an open channel of constant area is the three-dimensional time-averaged mass transfer equation

$$\frac{\partial \bar{c}}{\partial t} + \bar{u}\frac{\partial \bar{c}}{\partial x} + \bar{v}\frac{\partial \bar{c}}{\partial y} + \bar{w}\frac{\partial \bar{c}}{\partial z} = \frac{\partial}{\partial x}(\bar{K}_x \frac{\partial \bar{c}}{\partial x}) + \frac{\partial}{\partial y}(\bar{K}_y \frac{\partial \bar{c}}{\partial y}) + \frac{\partial}{\partial z}(\bar{K}_z \frac{\partial \bar{c}}{\partial z}) \qquad (7)$$

where x,y,z = the longitudinal, lateral, and vertical cartesian coordinates in an open channel

u, v, w = the velocity components in the x, y, z directions, respectively
c = concentration of the tracer
K = mixing coefficient
t = time

The equation is a mass balance equation and is derived by considering the loss and gain of mass through a small volume of fluid. In laminar flow, K represents the molecular diffusion coefficient D which is constant with time in all directions. In turbulent flow, molecular diffusion is considered insignificant compared to turbulent diffusion, therefore, K represents the turbulent diffusion coefficient ε which has components x, y, and z. For turbulent flow, the overbar indicates that the quantity has been averaged over a long enough time to smooth-out fluctuations due to turbulence yet short enough to preserve the oscillations in the velocity due to tidal motion. Equation (7) shows that the total mass transport is a function of both advective and diffusive mass transport.

Since interest often focuses on dispersion in the longitudinal or x-direction it is common to consider only the variations of c with x and t (Chatwin and Allen 1985). Therefore, a one-dimensional mass transfer equation is obtained by considering the concentration as a function of x and t, thus

$$\frac{\partial \bar{c}}{\partial t} + \bar{u}\frac{\partial \bar{c}}{\partial x} = \frac{\partial}{\partial x}\left(\bar{K}_x \frac{\partial \bar{c}}{\partial x}\right) \qquad (8)$$

If all quantities are considered to be constant across the width of the channel then equation (8) may be integrated over the channel depth h, normal to the longitudinal direction of flow, to give

$$\frac{\partial c}{\partial t} + u \frac{\partial c}{\partial x} = \frac{1}{h} \frac{\partial}{\partial x} \left(Kh \frac{\partial c}{\partial x} - \int_h u'c' \, dz\right) \qquad (9)$$

where u = depth-averaged velocity

c = depth-averaged tracer concentration

u' = deviation from u

c' = deviation from c

The results of space averaging have revealed a dispersive transport term $u'c'$, representing the longitudinal spreading of a tracer distribution governed primarily by the shape of the velocity profile (Holley et al. 1970). The longitudinal transport represented by the $u'c'$ term is much greater than the longitudinal transport by either molecular or turbulent diffusion. The term "dispersion" by the velocity profile due to spatial deviations u' and c' is used to distinguish this process from the molecular diffusion process in laminar flow, or the turbulent diffusion process in turbulent flow which is associated with temporal deviations u'' and c''. Equation (9) indicates that downstream advection by the mean velocity and the combined effects of a velocity shear and diffusion are the transport mechanisms.

The quantities u' and c' are defined by the following equations

$$U(z) = u + u'(z) \tag{10a}$$

$$C(z) = c + c'(z) \tag{10b}$$

in which U is the local fluid velocity in the x-direction and C is the local concentration of tracer. The two-dimensional velocity profiles for both laminar and turbulent flow are shown in Figure 26 for $u = 4$ cm/s and $h = 4$ cm. The laminar velocity profile is parabolic and given by (Fischer et al. 1979)

$$U_L = u_{max} \left[2\left(\frac{z}{h}\right) - \left(\frac{z^2}{h^2}\right) \right] \tag{11}$$

and, with subscript L referring to laminar flow. The turbulent velocity profile is represented by the logarithmic law equation (Fischer et al. 1979)

$$U_T = u + \left(\frac{u^*}{k}\right)\left[1 + \ln\left(\frac{z}{h}\right) \right] \tag{12}$$

where $k = 0.41$ the von Karman constant, and with subscript T referring to turbulent flow.

It can be seen in Figure 26 that u' in laminar flow is greater than u' in turbulent flow, i.e. the shear effect is greater in laminar than in turbulent flow, which in effect causes a tracer to initially be spread out in the longitudinal direction more so in laminar flow than in turbulent flow. Also, because vertical mixing by molecular diffusion

Fig. 26. Graphs of velocity profiles in laminar and turbulent flows of equal mean velocities in the same channel.

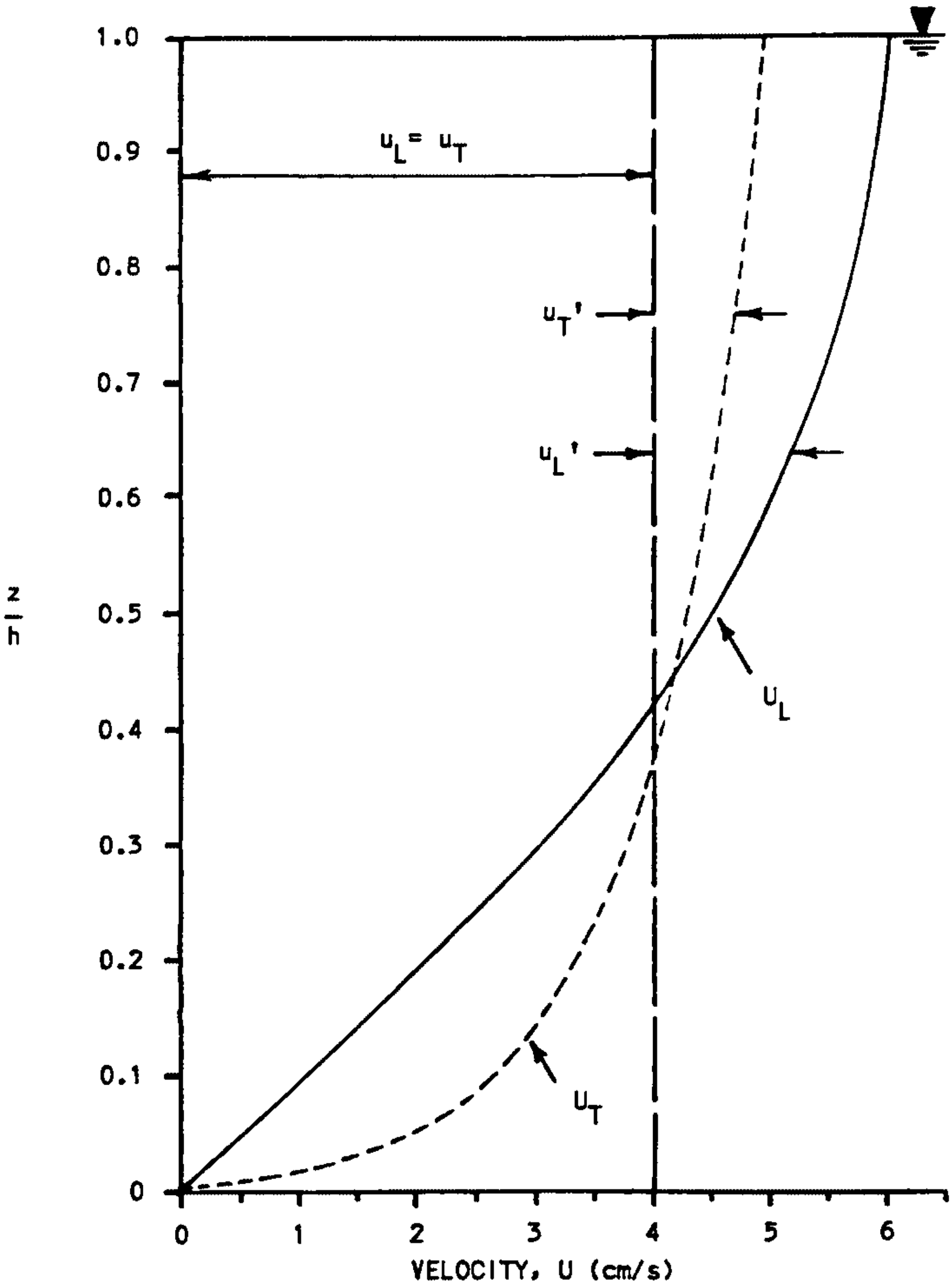
1.0
0.9
0.8
0.7
0.6
0.5
0.4
0.3
0.2
0.1
0
$\frac{z}{h}$
$u_L = u_T$
u_T'
u_L'
U_L
U_T
0
1
2
3
4
5
6
VELOCITY, U (cm/s)

in laminar flow is less than that by turbulent diffusion in turbulent flow, c' will be greater in laminar flow than in turbulent flow. Therefore, the $u'c'$ transport in equation (9) will initially be greater in laminar flow than in turbulent flow. For example, when the line source of tracer, referred to in Figure 25, initially takes the shape of the velocity distribution, the longitudinal spread of tracer would be greater if the profile was laminar than if the profile was turbulent.

If vertical mixing has caused the concentration distribution to be one-dimensional in the x-direction, i.e. if c' is much less than c then equation (9) has been shown (Taylor 1954) to be analogous to Fick's law of diffusion, i.e. the $u'c'$ transport is proportional to the longitudinal gradient of the mean concentration (Holley et al. 1970). Fick's law for a one-dimensional diffusion process $q = -D\ \partial c/\partial x$, says that the flux of solute mass q, i.e., the mass of a solute crossing a unit area per unit time in a given direction, is proportional to the gradient of solute concentration in that direction, and the minus sign indicates transport is from high to low concentrations (Fischer et al. 1979). Therefore, it is possible to write

$$Kh \frac{\partial c}{\partial x} - \int_h u'c'\, dz = Eh \frac{\partial c}{\partial x} \qquad (13)$$

The essential result is that the total mass transport in the streamwise direction is proportional to the concentration gradient in the streamwise direction (Fischer et al. 1979). For laminar flow, the effects of velocity and concentration variations with depth and molecular diffusion are lumped into a bulk transport coefficient called the longitudinal dispersion coefficient E_L (Fischer et al. 1979). For turbulent flow, the effects of velocity and concentration variations with depth and both molecular and turbulent diffusion are lumped into E_T. The longitudinal dispersion coefficient in analogy to the molecular or turbulent diffusion coefficient primarily expresses the diffusive property of the velocity distribution and is a measure of the rate of spreading of a tracer distribution. The mass transport represented by equation (13) is called longitudinal dispersion. Since, in equation (13) the $u'c'$ transport is much greater than the diffusion term $Kh\ \partial c/\partial x$, the diffusion term may be neglected and equation (13) rewritten as

$$- \int_h u'c'\, dz = Eh \frac{\partial c}{\partial x} \tag{14}$$

Combining equation (13) with equation (9) gives the one-dimensional mass transfer equation for a conservative tracer in shear flow

$$\frac{\partial c}{\partial t} + u \frac{\partial c}{\partial x} = \frac{1}{h} \frac{\partial}{\partial x} \left(hE \frac{\partial c}{\partial x}\right) \tag{15}$$

In general, u, h, and E may be functions of both x and t. The one-dimensional mass transfer equation is not applicable to a dispersing cloud immediately after introduction of the tracer, rather, it is applicable only after the initial period (Holley et al 1970).

A quantitative evaluation of longitudinal dispersion is possible by determining the numerical values of E for laminar flow and for turbulent flow in the same channel and at equal mean velocities from which the magnitudes of E_L and E_T can be compared.

The real time longitudinal dispersion coefficient for laminar shear flow E_L is found as follows (Fischer et al. 1979). The deviation of the concentration from the mean concentration over depth is

$$c' = \frac{1}{D}\frac{\partial c}{\partial x}\int_z \int_z u'\, dz\, dz + c'(0) \tag{16}$$

Substitution of equation (16) into equation (14) and solving for E_L gives

$$E_L = -\frac{1}{hD}\int_h u' \int_z \int_z u'\, dz\, dz\, dz \tag{17}$$

The extra term $\int_h u'[c'(0)]dz = c'(0)\int_h u'dz = 0$, because $\int_h u'dz = 0$. Since the mean velocity for any velocity distribution can be found by integration, i.e.

$$u = \frac{1}{h} \int_h U \, dz \tag{18}$$

then application of this operator to equation (11) gives the depth-averaged velocity

$$u = (2/3)u_{max} \tag{19}$$

Substitution of equation (19) into equation (11) and solving for u' gives the deviation of the velocity from the mean velocity over depth

$$u' = u_{max} \left(2 \frac{z}{h} - \frac{z^2}{h^2} - \frac{2}{3}\right) \tag{20}$$

Substitution of equation (20) into equation (17) and solving for E_L gives

$$E_L = \frac{1}{118} \frac{h^2 (u_{max})^2}{D} \tag{21}$$

The real time longitudinal dispersion coefficient for turbulent shear flow is found as follows (Fischer et al. 1979). The deviation of the concentration from the mean concentration over depth is

$$c' = \frac{\partial c}{\partial x} \int_z \frac{1}{\varepsilon_z} \int_z u' \, dz \, dz + c'(0) \tag{22}$$

Substitution of equation (22) into equation (14) and solving for E_T gives

$$E_T = -\frac{1}{h}\int_h u' \int_z \frac{1}{\varepsilon_z}\int_z u' \, dz \, dz \, dz \qquad (23)$$

As before, the extra term $\int_z u'[c'(0)]dz = 0$. The deviation of the velocity from the mean velocity over depth is found from the logarithmic law for turbulent flow, equation (12)

$$u' = \frac{u^*}{k}\left[\,1 + \ln\left(\frac{z}{h}\right)\,\right] \qquad (24)$$

Substitution of equation (24) into equation (23) with $\varepsilon_z = (kz/h)[1-(z/h)]hu^*$ (Fischer et al. 1979), and solving for E_T gives

$$E_T = \frac{0.404}{k^3}\,hu^* = 5.9\,hu^* \qquad (25)$$

For the laminar velocity profile given by equation (11) and shown in Figure 26, $u_{max} = 6$ cm/s and $h = 4$ cm. For salt or $KMnO_4$ in water, $D \simeq 10^{-5}$ cm^2/s. Substitution of these values into equation (21) gives $E_L = 5 \times 10^5$ cm^2/s. For the turbulent velocity profile given by equation (12) and shown in Figure 26, $u^* = 0.4$ cm/s and $h = 4$ cm. Substitution of these values into equation (25) gives $E_T = 9$ cm^2/s. The result is that $E_L \gg E_T$ for laminar and turbulent flows in the same channel with equal mean velocities.

In light of the preceding analysis, a physical explanation of why longitudinal dispersion is magnified in tidal models in which the flow is laminar part of the time and turbulent part of the time can now be drawn (Ward 1972). In oscillating flow, the flow reverses direction at each slack current. Since the flow near times of slack current is laminar, then each time the flow reverses direction the tracer distribution must initially take the shape of the laminar velocity profile. The result is that the tracer is initially spread out farther longitudinally in laminar flow than if the flow were turbulent all of the time. The greater shearing effect in laminar flow, in combination with very small vertical mixing, causes a large amount of differential convection during the period when the flow is laminar. When turbulence commences during the half cycle, the tracer is rapidly mixed over the channel depth. The net result is that the rate of longitudinal spread of tracer or the longitudinal dispersion coefficient E, averaged over half a tidal cycle, is greater than if the flow were continuously turbulent.

Chapter 4

SUMMARY AND CONCLUSIONS

A plunger-type tide generator proved to be adequate for the production of oscillating flow in the laboratory flume of this investigation. The tide generator was easy to operate and produced repeatable, sinusoidal, oscillating waves in the flume.

A low cost capacitance wave height measuring system proved to be of sufficient accuracy and stability for the measurement of small amplitude water waves in the tidal flume of this investigation. Further experimentation with different sensing elements is required if the system is to be used in salt water.

Despite the lack of equal flow regime on the model as in the prototype, it was possible to calibrate the tidal model to obtain Froude similitude of mean tidal propagation. In this investigation, model and prototype mean tide heights and current velocities showed good agreement.

The minimum Reynolds number criterion of 1400 for tidal models, recommended by various modeling authorities, was sufficient for the attainment of Froude similitude of mean tidal motion, however, it did not guarantee fully turbulent flow nor did it guarantee turbulence throughout all tidal stages in the model. In this investigation, prolonged periods of laminar flow were observed near times of slack current in the model. It is probable that this criterion is adequate in models which are used to solve navigation problems in which only mean tidal motion is of interest.

It is not probable that the dispersive mechanisms in estuary flows in which turbulent shear flow plays a significant role will be modeled correctly in distorted, tidal Froude models which are operated with laminar flow part of the time and turbulent flow part of the time. Unequal flow regime on the model in comparison to that of the prototype, due to viscous effects in the model, can be added to the reasons why estuary models may distort longitudinal dispersion, i.e. in addition to those limitations imposed by depth distortion and exaggerated roughness. In this investigation, similitude of longitudinal dispersion was not achieved in an undistorted, constant-density, tidal Froude model operated according to the minimum Reynolds number criterion for tidal models. Similitude of longitudinal dispersion was also not achieved in previous investigations conducted in the upper reaches of the ODU Lafayette River and WES Chesapeake Bay hydraulic models in which the flows were characterized by low Reynolds numbers.

Longitudinal dispersion can be expected to be magnified in tidal Froude models which are operated with laminar flow during portions of the tidal cycle as a result of laminar viscous scale effects. In this investigation and in previous investigations conducted in the ODU and WES hydraulic models, the models predicted greater longitudinal dispersion than that of their respective prototypes. Evaluation of the mass transfer equations governing the process of longitudinal dispersion and subsequent quantitative evaluation of longitudinal dispersion in both laminar and turbulent flow showed that the longitudinal dispersion coefficient is greater in laminar than in turbulent flow. Therefore, in tidal flow the rate of spread of tracer, averaged over half a tidal cycle, will be greater in flows which are laminar part of the time and turbulent part of the time than if the flow were continuously turbulent. This conclusion confirms the results of this investigation and those of several, previous investigations in estuary models.

Further research is required to determine a criterion for turbulent flow throughout the tidal cycle for estuary models which are used to solve problems associated with water quality.

REFERENCES CITED

Allen, J. 1934. Streamline and turbulent flow in open channels. Phil. Mag., Ser. 7, Vol. 17, No. 116, 1081-1112.

Allen, J. 1947. Scale Models in Hydraulic Engineering. Longmans, Green and Co., London.

Anderson, A.L., Shirley, D.J. and Wilkins, L.H. 1972. An improved capacitance wavestaff for water surface wave measurements. Proc. IEEE, Oceans 1972, 483-486.

Blair, C.H. 1976. Similitude of mass transfer processes in distorted Froude model of an estuary. Dissertation presented in partial fulfillment of the requirements for the degree of Doctor of Philosophy. Old Dominion University Department of Civil Engineering, Norfolk, Virginia.

Blair, C.H. 1979. Hydraulic model verification of marina pollutant fields. Proposal to VIMS Sea Grant Program, Proj. No. R/CM-3, ODURF No.: VIMS-79-1183-686, College of William and Mary, Gloucester Point, Virginia.

Blair, C.H. 1980. Hydraulic model verification of marina pollutant fields. Proposal to VIMS Sea Grant Program, Proj. No. R/CM-3, ODURF No.: VIMS-80-1183-686, College of William and Mary, Gloucester Point, Virginia.

Blair, C.H. 1981. Hydraulic model verification of marina pollutant fields. Proposal to VIMS Sea Grant Program, Proj. No. R/CM-3, ODURF No.: VIMS-81-1183-686, College of William and Mary, Gloucester Point, Virginia.

Blair, C.H., and Kuo, C.Y. 1979. Mass transfer verifications of tidal Froude models. J. Hydraul. Div. Proc. A.S.C.E. 105, Tech. Note Proc. Paper, 1561-1564.

Chatwin, P.C. and Allen, C.M. 1985. Mathematical models of dispersion in rivers and estuaries. Ann. Rev. Fluid Mech. 17, 119-149.

Chatwin, P.C. and Sullivan, P.J. 1982. The effect of aspect ratio on longitudinal diffusivity in rectangular channels. J. Fluid Mech. 120, 347-358.

Coates, J. 1982. Research could redefine shellfish harvesting zones. ODU Courier, Nov. 5, Old Dominion University, Norfolk, Virginia, p. 5.

Cook, D. 1982. Modeling for marinas. Marine Resources Bulletin 14, No. 4, Virginia Sea Grant Advisory Service, VIMS, pp. 4-5.

Crickmore, M.J. 1972. Tracer tests of eddy diffusion in field and model. J. Hydraul. Div. Proc. ASCE 98, 1737-1751.

Cushing, V.J. 1974. Electromagnetic Flowmeters, in Flow: its Measurement and Control in Science and Industry, R.B. Dowdell, ed., Instrument Soc. Am., Pittsburg, Pennsylvania, vol. 1, part 2.

Daily Press. 1983. Oceanographer studies oyster bed zone laws. Newport News, Virginia, July 24.

Deaner, D.G. 1973. Effect of Chlorine on Fluorescent Dyes. J. Water Poll. Control Fd. 45, 507-514.

Dyer, K.R. 1977. Estuaries: A Physical Introduction. John Wiley & Sons Ltd., London.

Fischer, H.B. 1969. The effect of bends on dispersion in streams. Water Resour. Res. 5, 496-506.

Fischer, H.B. 1973. Longitudinal dispersion and turbulent mixing in open-channel flow. Ann. Rev. Fluid Mech. 5, 59-78.

Fischer, H.B. 1976. Mixing and dispersion in estuaries. Ann. Rev. Fluid Mech. 8, 107-133.

Fischer, H.B. and Hanamura, T. 1975. The effect of roughness strips on transverse mixing in hydraulic models. Water Resour. Res. 2, 362-364.

Fischer, H.B. and Holley, E.R. 1971. Analysis of the use of distorted hydraulic models for dispersion studies. Water Resour. Res. 7, 46-51.

Fischer, H.B., List, E.J., Koh, R.C.Y., Imberger, J., and Brooks, N.H. 1979. Mixing in Inland and Coastal Waterways. Academic Press, New York.

Grace, R.A. 1970. How to measure waves. Ocean Industry, February, 65-69.

Harleman, D.R.F. 1966. Pollution in Estuaries, in Estuary

<u>and Coastline Hydrodynamics</u>, A. Ippen, ed., McGraw-Hill Co., New York, pp. 630-649.

Harleman, D.R.F. 1971. Physical Hydraulic Models, in <u>Estuarine Modeling: An Assessment</u>, G. Ward and W. Espey Jr., eds., TRACOR Inc., Austin, Texas, pp. 215-263.

Henderson, F.M. 1966. <u>Open Channel Flow</u>. The Macmillan Co., New York.

Herrman, F.A. 1979. Estuaries, in Coastal Hydraulic Models, Special Report No. 5, U.S. Army Corps of Engineers Coastal Engineering Research Center, Fort Belvoir, Virginia, pp. 48-201.

Hickox, G.H. 1952. Hydraulic Models, in <u>Handbook of Applied Hydraulics</u>, C.V. Davis and K.E. Sorensen, eds., McGraw-Hill Co., New York, 1121-1158.

Holley, E.R., Harleman, D.R.F. and Fischer H.B. 1970. Dispersion in homogeneous estuary flow. J. Hydraul. Div. Proc. ASCE 8, 1691-1709.

Ippen, A.T. 1966. Salinity Intrusion in Estuaries, in <u>Estuary and Coastline Hydrodynamics</u>, A. Ippen, ed., McGraw-Hill Co., New York, pp. 598-629.

Ippen, A.T. and Harleman, D.R.F. 1966. Tidal Dynamics in Estuaries, in <u>Estuary and Coastline Hydrodynamics</u>, A. Ippen, ed., McGraw-Hill Co., New York, pp. 493-521.

Jugan, M.J. 1982. The Effects of Varying Freshwater Discharge on Dispersion in an Estuarine Hydraulic Model of the Lafayette River, Norfolk, Virginia. Thesis presented in partial fulfillment of the requirements for the degree of masters of Science. Old Dominion University Department of Oceanography, Norfolk, Virginia.

Keulegan, G.H. 1966. Model Laws for Coastal and Estuarine Models, in <u>Estuary and Coastline Hydrodynamics</u>, A. Ippen, ed., McGraw-Hill Co., New York, pp. 691-710.

Killen, J.M. 1955. Capacitive wave profile recorder. Proc. First Conf. on Coast. Eng. Instruments, Berkeley, California, pp. 32-38

Knight, D.W. and Macdonald, A.J. 1979. Open channel flow with varying bed roughness. J. Hydraul. Div. Proc. ASCE 105, 1167-1183.

Kuo, C.Y., Blair, C.H., Mayhew, J.D., Wong, H.F.N., Wang, W. C. 1978. Mass transport study in a hydraulic model. Old Dominion Univ. Research Foundation, Norfolk, Virginia.

LeMehaute, B. 1976. An Introduction to Hydrodynamics and Waterwaves. Springer-Verlag, New York.

Maxwell, H.C. and Weggel, J.R. 1969. Surface tension in Froude models. J. Hydraul. Div. ASCE 95, 677-701.

McGoldrick, L.F. 1969. A system for the generation and measurement of capillary-gravity waves. Dept. of Geophys. Sci., Univ. of Chicago, Tech. Rep. No. 3, Chicago, Illinois.

Moore, J.B. 1964. A water wave recording instrument for use in hydraulic models. 41, 321-323.

Nece, R.E., Richey, E.P., Rhee, J. and Smith, H.N. 1979. Effects of planform geometry on tidal flushing and mixing in marinas. Dept. Civil Eng., Univ. of Washington, Tech. Rep. No. 62, Seattle, Washington.

Novak, P. and Cabelka J. 1981. Models in Hydraulic Engineering. Pitman Advanced Publishing Program, Boston.

Plapp, J.E. 1968. Engineering Fluid Mechanics. Prentice-Hall, Inc., Englewood Cliffs, New Jersey.

Pond, S. and Pickard G.L. 1978. Introductory Dynamic Oceanography. Pergamon Press, Oxford.

Pritchard, D.W. 1965. Kinsman's Notes on Lectures on Estuarine Oceanography. The John Hopkins University, Baltimore, Maryland.

Rouse, H. 1961. Fluid Mechanics for Hydraulics Engineers. McGraw-Hill Book Co., New York.

Sager, R.A. and Hales, L.Z. 1979. Inlets, in Coastal Hydraulic Models, Special Report No. 5, U.S. Army Corps of Engineers Coastal Engineering Research Center, Fort Belvoir, Virginia, pp. 453-519.

Scheffner, N.W., Crosby, L.G., Bastian, D.F., Chambers, A.M., Granat, M.A. 1981. Verification of the Chesapeake Bay Model. Hydraulics Laboratory, U.S. Army Engineer Waterways Experiment Station, Tech. Rep. HL-81-14, Vicksburg, Mississippi.

Stevens, J.C. 1942. Hydraulic Models. ASCE Manual of Engineering Practice No. 25., New York.

Taylor, G.I. 1953. Dispersion of soluble matter in solvent flowing slowly through a tube. Proc. R. Soc. London Ser. A 219, 186-203.

Taylor, G.I. 1954. The dispersion of matter in turbulent flow through a pipe. Proc. R. Soc. London Ser. A 223, 446-468.

Timpy, D.L. 1982. A Capacitance Wavestaff and Measurements of Wave Height Decay in the Surf Zone. Thesis presented in partial fulfillment of the requirements for the degree of Master of Science. Old Dominion University Department of Oceanography, Norfolk, Virginia.

Tucker, M.J. and Charnock H. 1954. A Capacitance-Wire Recorder for Small Waves, in Conf. on Coastal Engineering, Univ. of California, Berkeley, California, pp. 177-187.

Turner Designs. 1975. Circulation, dispersion and plume studies: a monograph. Mountain View, California.

Turner Designs. 1982. Flow measurements: a monograph. Mountain View, California.

Von Arx, W.S. 1967. An Introduction to Physical Oceanography. Addison-Wesley Publishing Co.

Ward, P.R.B. 1972. Transverse dispersion of pollutants in oscillatory open-channel flow. Hydraulic Eng. Lab., Dept. of Civil Eng., Univ. of California, Report No. WHM2, Berkeley, California.

Webel, G. and Schatzmann, M. 1984. Transverse mixing in open channel flow. J. Hydraul. Eng. ASCE 110, 423-435.

Whittenbury, C.G., Huber, E.A. and Newell, G.S. 1959. Instrument for measuring water waves. The Rev. of Sci. Instr. 30, 674-676.

Wilner, L.B. 1960. Variable capacitance liquid level sensors. The Rev. of Sci. Instr. 31, 501-507.